Charles University in Prague
Faculty of Mathematics and Physics

BACHELOR THESIS

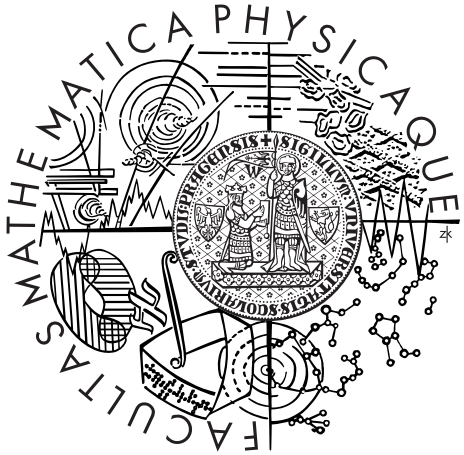

Michael Hakl

Studium vlastností heterostrukturních tenkých vrstev křemíku s nanometrovým rozlišením

Department of Material Research

Supervisor of the bachelor thesis: RNDr. Antonín Fejfar, CSc.

Study programme: Physics

Specialization: General Physics

Prague 2012

Acknowledgements

I would like to express deep gratitude to the thesis supervisor, Dr. Antonín Fejfar, for his guidance, patience, critical comments and corrections of my writing. I am also very grateful to the advisors, Dr. Martin Ledinský and Dr. Aliaksei Vetushka, for their invaluable assistance and support. The research would not have been possible without their abundant helps and best suggestions.

I acknowledge the advice and recommendations of Ing. Jakub Zlámal who enabled me to use high-performance computers at the Faculty of Mechanical Engineering, University of Technology, Brno.

Thanks also go to the group of colleagues: Robin Schilhart, Peter Pikna, Matěj Hývl, Martin Müller, Tina Ganzerová and Ing. Vlastimil Píč for encouragement and providing an excellent atmosphere.

Finally, the author would also like to convey thanks to the Institute of Physics for providing the financial means through the project PolySiMode funded by European Union, FP7-Energy-2009-1 Grant Agreement No. 240826 and for providing laboratory facilities.

Honorable Declaration

I declare that I carried out this bachelor thesis independently, and only with the cited sources, literature and other professional sources.

I understand that my work relates to the rights and obligations under the Act No. 121/2000 Coll., the Copyright Act, as amended, in particular the fact that the Charles University in Prague has the right to conclude a license agreement on the use of this work as a school work pursuant to Section 60 paragraph 1 of the Copyright Act.

In Prague 2012 signature of the author

Title: Study of properties of heterostructured thin silicon films in nanometer resolution

Author: Michael Hakl

Department: Material Research

Supervisor: RNDr. Antonín Fejfar, CSc., Department of Thin films and Nanostructures, Institute of Physics, Academy of Sciences of the Czech Republic

Abstract: Thin films based on heterostructured mixture of amorphous and microcrystalline hydrogenated silicon have a perspective application in production of low-cost photovoltaic cells. Local electrical properties of silicon microcrystalline grains embedded in amorphous silicon phase were studied in nano- and microscale resolution. Measurements of film's surface topography and local electrical conductivity were performed with atomic force microscope (AFM) under standard ambient conditions. Scanning electron microscope and AFM observations identified a constant shape of microcrystalline grains. In the first approximation, the grain can be characterized as a cone with a spherical cap. A simplified finite element model of the crystalline grain was created in the Comsol Multiphysics simulation software and used for calculations of various grain's arrangements. The text includes experimental and theoretical points of view on thin-film's fine structure and its local electrical properties.

Keywords: Local electrical properties, microcrystalline silicon, thin films, atomic force microscopy, finite element method

Název práce: Studium vlastností heterostrukturních tenkých vrstev křemíku s nanometrovým rozlišením

Autor: Michael Hakl

Katedra: Fyzika kondenzovaných látek

Vedoucí bakalářské práce: RNDr. Antonín Fejfar, CSc., oddělení tenkých vrstev a nanostruktur, Fyzikální ústav, Akademie věd České republiky, v. v. i.

Abstrakt: Tenké filmy na bázi heterostrukturní směsi amorfního a mikrokrystalického křemíku mají perspektivní využití při výrobě levných fotovoltaických článku. Lokální elektrické vlastnosti mikrokrystalických křemíkových zrn zapuštěných v amorfní křemíkové fázi byly detailně studovány s mikrometrovým a nanometrovým rozlišením. Byly provedeny měření topografie a lokální elektrické vodivosti pomocí mikroskopu atomárních sil (AFM) za standartních atmosférických podmínek. Elektronový mikroskop spolu s AFM zjistily, že mikrokrystalická zrna zaujímají konstantní tvar, který lze v prvním přiblížení charakterizovat jako kužel s vrchní kulovitou čepicí. V simulačním programu Comsol Multiphysics byl vytvořen jednoduchý model krystalického zrna, který byl dále podrobován různým fyzikálním podmínkám. Tento text tudíž podává jak experimentální, tak teoretický pohled na jemnou strukturu a lokální elektrické vlastnosti tenkých filmů.

Klíčová slova: Lokální elektrické vlastnosti, tenké vrstvy, mikrokrystalický křemík, mikroskop atomárních sil, metoda konečných prvků

Contents

1. Introduction

1.1 Photovoltaic solar cell energy conversion

The main argument for intensive scientific research of electrical, optical and structural properties of silicon is its importance for electrical industry. Silicon is a convenient material due to semiconductive behaviour. Moreover, silicon has almost an ideal bandgap for absorption of the sunlight and it is even the second most abundant element in the Earth's crust with 26% (after oxygen).

In last decades there are tendency and technical means to study thin silicon films for application in photovoltaic cells, thin film transistors and various detectors. Thin Si films bring several advantages for production of photovoltaic cells such as decrease of material and energy inputs. But thin Si solar cells still retain sufficient energy conversion efficiency around 5-10% [csgsolar]. For instance, during fabrication of a monocrystalline or polycrystalline solar cells, 50% of primary ingot is wasted because of etching and slicing processes. Price of $1\,kg$ solar-grade quality poly-silicon is around 100 \$. There are strong principal reasons for investing funds and supporting progress in this field such as reduction of manufacturing costs of PV cell, satisfaction of rapidly increasing energy consumption and possible way out from fossil fuel depletion.

Let us shortly summarize basic physical facts and limitations concerning solar cell energy production. Solar radiative power density at the Earth distance is about $1350\,W/m^2$. Power, that penetrates to the Earth surface at 50° latitude, is approximately $900\,W/m^2$, which corresponds to $14\,GJ/m^2$ per annum. Manufacturing of $1\,m^2$ of photovoltaic(PV) panel requires about $1\,GJ$ in dependence on type of PV panel [Alsema]. With 5% efficiency of cell we get 1.4 year of energy payback time. In early years of PV cell lifetime, efficiency of energy conversion is decreased by $\approx 1\%$ per year as PV modules degraded. With effective lifetime of 15 years, the remaining final energy profit is less than $9.5\,GJ$. There is still a large scope for further improvements.

In the figure Fig. 1.1 distribution of spectral solar radiation power is depicted in dependence upon wavelength of electromagnetic waves. The main area under the curve lies in optical and infrared range and a minor part in ultraviolet range.

Energy gap of amorphous silicon is $E_g(\text{a-Si}) \approx 1.7\,eV$ and for crystalline silicon $E_g(\text{c-Si}) \approx 1.1\,eV$ which correspond to photoelectric-effect absorption edge at wavelengths $\lambda(\text{a-Si}) = 730\,nm$ and $\lambda(\text{c-Si}) = 1130\,nm$. Thus the main part of the solar radiation is able to excite electrons from the valence band to the conductive band.

Light absorption coefficient of silicon is $\alpha(\lambda = 400) = 1.22 \times 10^5\,cm^{-1}$, $\alpha(\lambda =$

Figure 1.1: *Solar spectrum with maximum radiation intensity at* 480 *nm.*

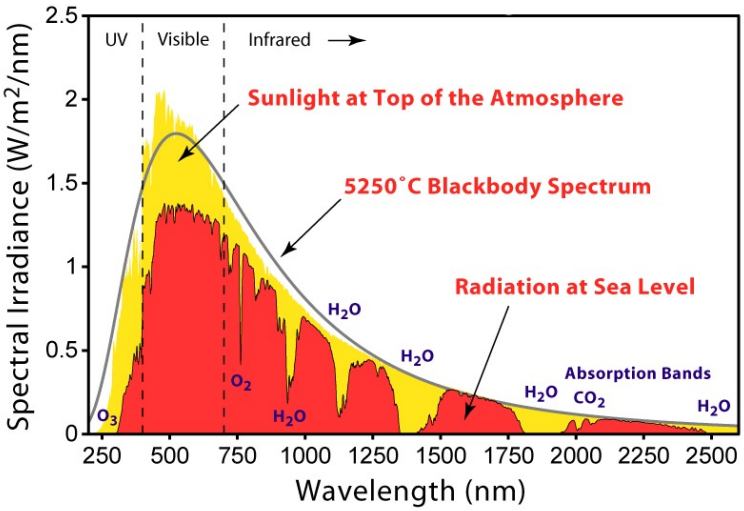

600) $= 5.2 \times 10^3\, cm^{-1}$. According to the Beer–Lambert law, absorption depth in c-Si is $d(600\,nm) = 4.4\,\mu m$, $d(400\,nm) = 0.19\,\mu m$ for 10% of initial light intensity and $d(600\,nm) = 8.9\,\mu m$, $d(400\,nm) = 0.38\,\mu m$ for 1% of initial intensity. Only a few micrometers thin layer of silicon is needed to absorb the main part of incident radiation flux. This is considered as one of the most important advantages of thin films PV cells.

In this paper we will focus on thin films based on heterogeneous mixture of amorphous and microcrystalline silicon in order to characterize, describe and discuss its fundamental electric and morphological properties.

However, at this place a very short introduction into silicon films and elementary physics of semiconductors will follow.

1.2 Microcrystalline and amorphous hydrogenated silicon for thin-film PV cells

Crystalline silicon possesses diamond structure at normal conditions. Unit diamond cell (Fig. ??) consists of four tetrahedrons. Bond angle is 109°28′ and bond length is approximately 2.35 Å. In amorphous silicon, there is a distribution of bond angles with standard deviation of 6° to 9° around c-Si value and bond lengths are randomly distributed around average crystalline value (with standard deviation about 1%).

In hydrogenated amorphous silicon (a-Si:H) layers prepared from silane[1], point defects occur in formation caused by missing of certain bonds. Such a missing bond is called a dangling bond. A silicon atom shares bond to three or less

[1]Silane is gas composed of molecules SiH_4.

Figure 1.2: *Diamond structure of crystalline silicon. Examples of Si dangling bonds.*

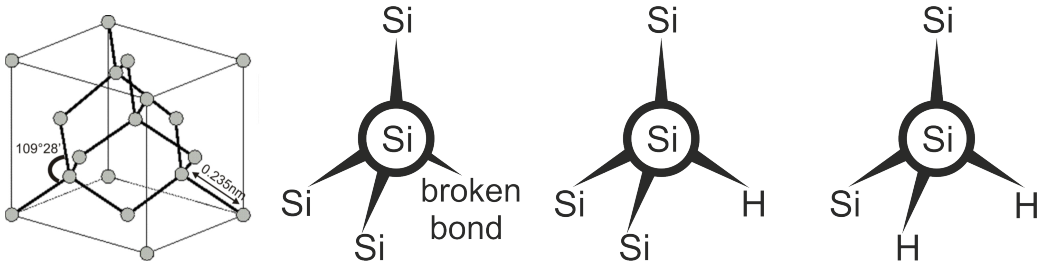

silicon atoms and the remaining bond (unpassivated dangling bond) may be either unoccupied or filled with a hydrogen atom (Fig. ??).

Unsaturated bonds act as recombination centers in electric conduction. Their corresponding electronic states lie near the energy midgap.

Defect density of the layer is the highest at bottom or top boundary of the layer. Under exposure of light, some weaker bonds are broken and new dangling bonds are created. This effect is called light-induced degradation (Staebler-Wronski effect) [Shah]. After 1000 hours of the a-Si layer light-soaking degradation saturates at range of $10^{16} - 10^{17}$ dangling bonds per $1\,cm^3$ which is about 10 to 100 higher than the initial value. Structural disorder of a-Si causes bandtails at the edge of valence and conduction band. The density of states in these bandtails decreases exponentially, as one moves towards the middle of the bandgap. Dependence of the bandgap of a-Si:H on hydrogen incorporation varies linearly from about $1.5\,eV$ for 0% hydrogen concentration to about $2\,eV$ for 50%.

Dispersion of amorphous and crystalline silicon is shown in Fig. 1.3. Optical absorption coefficient (which appears in Beer-Lambert law) as a function of wavelength is in Fig. 1.4.

μc-Si:H is a mixture of crystalline grains with predominance of micrometer-sized features. Let us assume a typical columnar microcrystalline grain of size $50 \times 50 \times 200\,nm$. Mass density of pure crystalline silicon is $\varrho(\text{c-Si}) = 2.33\,g/cm^3$. Density of ideal amorphous silicon differs very slightly (about 97% of the crystalline density). So, the atomic density of silicon is $5 \times 10^{22}\,cm^{-3}$. Volume of such grain is $5 \times 10^5\,nm^3$ and consists of 2.5×10^7 atoms. Area of the grain surface is $45 \times 10^3\,nm^2$ and grain surface contains 6×10^5 atoms. It means that 2.5% of all atoms in the grain are located at the grain's boundary.

Selected properties of silicon are presented in table Tab. 1.

1.3 Deposition of Si thin films

Standard process for thin film fabrication is plasma enhanced chemical vapour deposition (PECVD) [Vetushka-phd], [Shah]. Scheme of the method may

Figure 1.3: *Dispersion of silicon. Re, Im denote real part, resp. imaginary parts of refractive index. Abbreviations c-Si, a-Si, poly-Si stand for crystalline [ncSi], amorphous [naSi], polycrystalline silicon [npSi].*

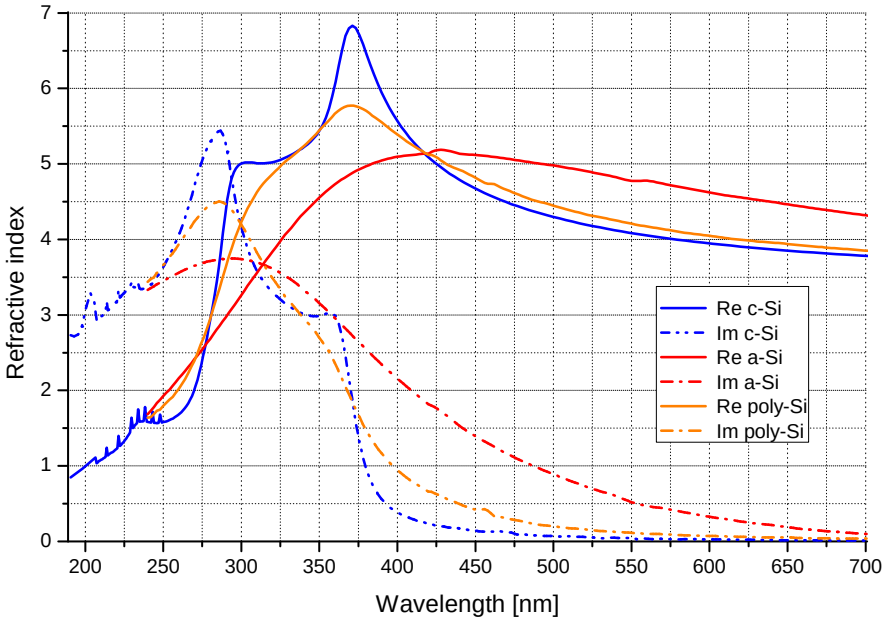

Figure 1.4: *Absorption coefficient and standard absorption depth (37% of initial intensity) of crystalline silicon in dependence on wavelength [AbsorpSi]. Note that functions are plotted in a logarithmic scale and vary over 10 orders of magnitude.*

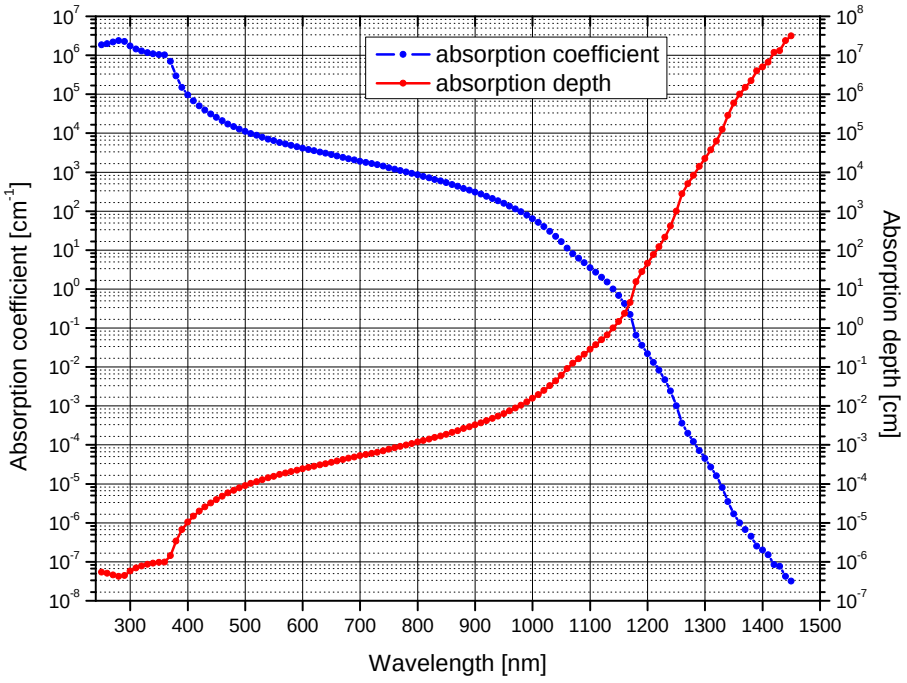

be simply introduced in Fig. 1.5. Gas containing desired material is brought to vacuum chamber with a substrate to deposit inside. Substrate's electrode is grounded. The second electrode is floating and connected to radiofrequency voltage generator. Electrons are emitted from electrodes and collide with gas molecules. Electron impacts ionize molecule and plasma is created. Oscillating electromagnetic field gives molecules activation energy and accelerates them to the electrode with substrate wafer. Ions act as radicals and take part in other chemical reactions. Products of reaction adsorb (condense) at the substrate surface, which starts the layer growth.

For deposition of silicon films, silane SiH_4 is used as a suitable gas, diluted with hydrogen H_2. Usual substrate material is optical glass. Typical generator frequency is $13.56\,MHz$. Substrate temperature is circa $200-300\,°C$ and chamber pressure is roughly $100\,Pa$. Deposition rate is about $10\,nm/min$.

During deposition, silicon atoms get through three type of chemical reactions [Shah]. Electrons dissociate silane molecules:

$$\begin{aligned} SiH_4 + e &\longrightarrow SiH_2 + 2H \\ SiH_4 + e &\longrightarrow SiH_3 + H \\ H_2 + e &\longrightarrow 2H\,. \end{aligned}$$

Then the several reactions of silane with radicals follow

$$\begin{aligned} SiH_4 + H &\longrightarrow SiH_3 + H_2 \\ SiH_4 + H &\longrightarrow SiH_2 + H_2 \\ SiH_4 + SiH_2 &\longrightarrow Si_2H_6 + H_2 \\ 2H &\longrightarrow H_2\,. \end{aligned}$$

Entire process is finished with surface reactions

$$\begin{aligned} SiH_2 &\longrightarrow Si_{surface} + H_2 \\ SiH_3 &\longrightarrow 2Si_{surface} + 3H_2 \\ 4H + Si_{surface} &\longrightarrow SiH_4\,. \end{aligned}$$

There are several technical parameters controlling deposition process such as dilution ratio, gas flow, substrate size, electrode spacing, substrate temperature, gas pressure, excitation frequency, voltage applied to plasma and deposition time.

The crucial parameter for morphology of silicon layer is dilution ratio defined as

$$R = [H_2]/[SiH_4]\,,$$

where $[H_2]$, $[SiH_4]$ denote relative gas flows. Dilution ratio influences primarily layer crystallinity. Effect of hydrogen concentration to grain formation is described in Fig 1.6. Increase of hydrogen dilution raises the crystalline volume fraction.

Hydrogen additive also affects the amorphous tissue formation, in paper [Bronsveld] (p. 1012 , Fig. 2) one may observe long vertical columnar structure in amorphous phase. The specimen crystallinity can be measured through Raman spectra (Fig. 1.7).

Figure 1.5: *Scheme of a PECVD reactor chamber.*

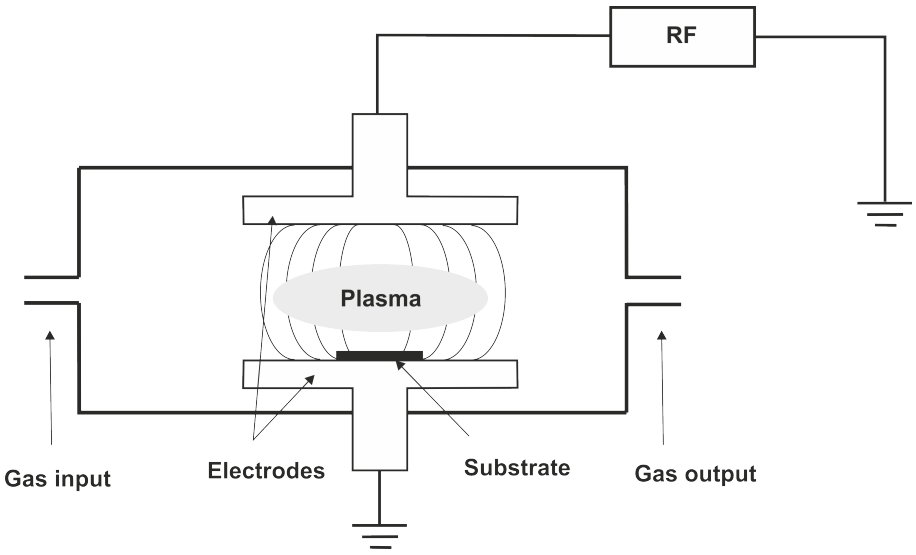

Figure 1.6: *Effect of hydrogen concentration on crystalline volume fraction (adopted from [Shah]. Horizontal scale defines hydrogen dilution R. Dark dashed line indicates the start of microcrystalline growth process, light dashed line shows fusion of grains into compact agglomerates.*

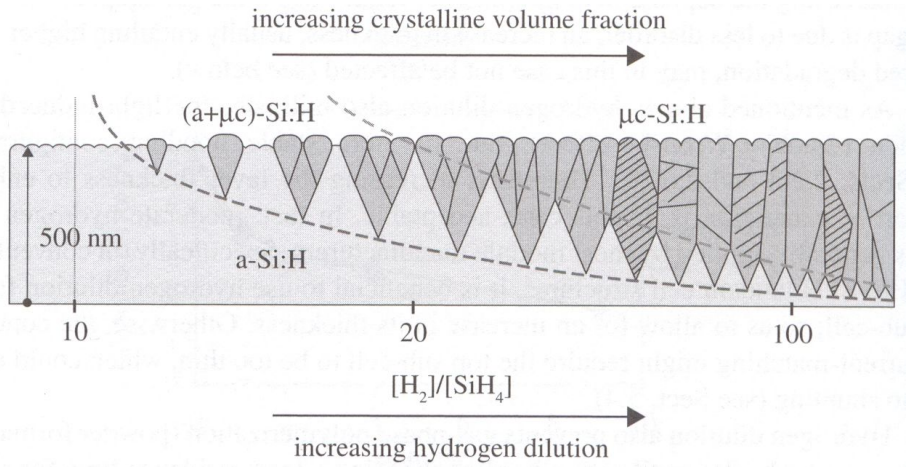

1.4 Photogenerated charge collection in disordered structure

At zero absolute temperature, all valence electrons of intrinsic semiconductor rest in valence band below Fermi energy level. At room temperature, minor part of electrons are thermally excited above bandgap to the conductive valence

Figure 1.7: *Exemplary Raman spectra of μc-Si:H and a-Si:H [Shah]. Notice different positions of microcrystalline and amorphous peaks. Increase of hydrogen portion enlarges width of the μc-Si:H peak.*

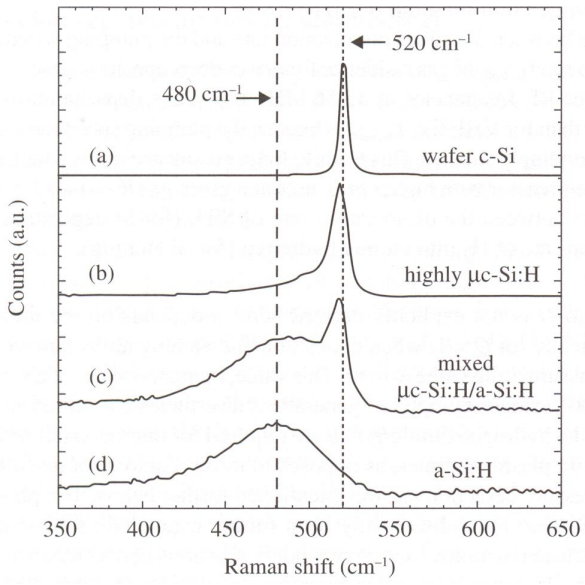

band. Transfer of electrons into the conductive band creates charge vacancies in the valence band, which can be considered as positive charge carriers – holes.

1.4.1 Carrier recombination

Electrons in the conductive band are in meta-stable state and make efforts to return to the lower located valence band. If the demoted electron encounters a hole, both carrier annihilate. This process is called recombination. There are three main types of recombination.

In radiative (band-to-band) recombination, an electron directly recombines with a hole in valence band, then a photon with energy equivalent to the energy bandgap is emitted.

Auger recombination involves three carriers: two electrons and one hole. If the first electron recombines with the hole, the released energy is turned over to the second electron, which afterwards thermalizes back to the conductive band edge. Both previous types of recombination are rare effects.

The third case, so called Shockley-Read-Hall recombination, is caused by dangling bond defects and impurities. Dangling bonds bring extra energy level to classical energy band structure located approximately in the middle of the energy gap. Free electrons from the conductive band are attracted to the positively charged dangling bond. If free hole meets a neutral dangling bond at the same site, then both carriers will exist at similar energy level and may recombine. There is also an opposite situation to the previous one. When free electron collides with a neutral dangling bond or when free hole merges with negatively dangling bond

Figure 1.8: *Schema of electron hole attraction and recombination at dangling bond locus. On the left side capture process is described at positively charged dangling bond, on the right side the recombination is depicted at negatively charged dangling bond.* S_{e+}, S_{h-} *mean effective cross section area for electron capture at positive dangling bond, resp. for hole capture at negative dangling bond;* S_{e0}, S_{h0} *denote effective cross section areas of electron resp. hole capture at neutral dangling bond.*

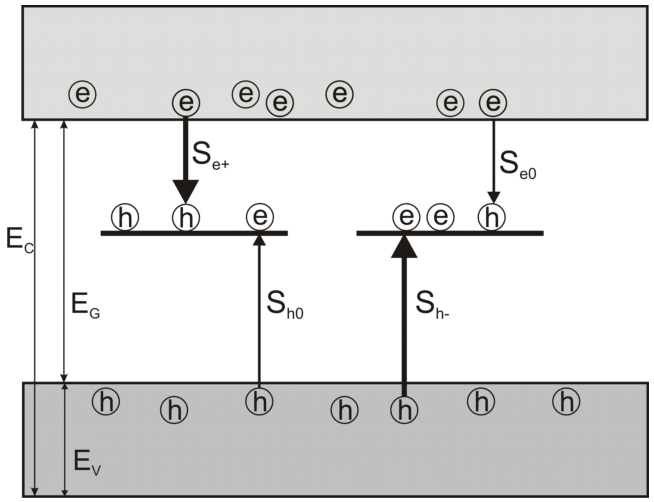

at the same local state, then they recombine. Both processes are added together.

Let N_{db} be volume density of dangling bonds and ν_e, ν_h are thermal velocities of electrons resp. holes. Denote S_{e0}, S_{h0}, S_{e+}, S_{h-} effective capture cross section of electron and neutral dangling bond, hole and dangling bond, electron and positively charged dangling bond respectively hole and negatively charged dangling bond. Probability of carrier capture by the bond recombination center is given by standard expression from scattering theory

$$\text{Probability of capture} = 1 - \exp\left(\frac{t}{\tau}\right) = 1 - \exp(-N_{db}Sx) \approx N_{db}Sx\,, \qquad (1.1)$$

where x is a distance between the place of carrier inception and the place of carrier recombination, t is time to recombination and τ denotes mean carrier lifetime. Further we know $x = \nu t$. Thus

$$\frac{1}{\tau} = N_{db}S\nu\,. \qquad (1.2)$$

Occurrence of recombinations are independent phenomena, so effective mean carrier lifetime is according to Matthiessen rule

$$\frac{1}{\tau_{tot}} = \frac{1}{\tau_{e0}} + \frac{1}{\tau_{h-}} = \frac{1}{\tau_{e+}} + \frac{1}{\tau_{h0}}\,. \qquad (1.3)$$

Last equality holds true because $e0$, $h-$ and $e+$, $h0$ are complementary events.

1.4.2 Dark conductivity

Conductivity of material with volume density of carriers N is commonly defined as

$$\sigma = e\mu N\,, \tag{1.4}$$

where μ denotes carrier mobility and e is an elementary charge. Then conductivity of a material, compounded from electron and hole charge carriers, is

$$\sigma = \sigma_e + \sigma_h = e(\mu_e N_e + \mu_h N_h)\,. \tag{1.5}$$

With elementary consideration (e.g. from Drude theory of conductivity), it is possible to get general expression for electron mobility

$$\mu_e = \frac{e\tau}{m_e^*}\,, \tag{1.6}$$

where m_e^* denotes effective electron mass.

Without any illumination, carrier density in the valence and conductive band is given only by thermal equilibrium. Hole density of states in the valence band is according to Sommerfeld model

$$g_h(\mathcal{E}) = 2\frac{1}{4\pi^2}\left(\frac{2m_h^*}{\hbar^2}\right)^{3/2}\sqrt{\mathcal{E}_V - \mathcal{E}}\,, \tag{1.7}$$

where $\hbar$ is reduced Planck constant, m_h^* is effective hole mass, $\mathcal{E}_V$ is energy of valence band. Similar expression can be written for electron density of states in conductive band

$$g_e(\mathcal{E}) = 2\frac{1}{4\pi^2}\left(\frac{2m_e^*}{\hbar^2}\right)^{3/2}\sqrt{\mathcal{E} - \mathcal{E}_C}\,, \tag{1.8}$$

where m_e^* is effective electron mass for density of states calculations, $\mathcal{E}_C$ is energy of conductive band edge.

Assume nondegenerated intrinsic semiconductor, i.e. $\mathcal{E}_C - \mathfrak{u} \gg k_B T$ and $\mathfrak{u} - \mathcal{E}_V \gg k_B T$, where $\mathfrak{u}$ is chemical potential of electrons, T is absolute temperature, k_B is Boltzmann constant.

Electrons and holes satisfy Fermi-Dirac statistics that can be approximated for room temperature with the Boltzmann distribution: $\exp\{-(\mathcal{E} - \mathfrak{u})/k_B T\}$.

Thus, total concentration of electrons in conductive band is

$$N_e(T) = \int_{\mathcal{E}_C}^{+\infty} g_e(\mathcal{E})\exp\{-\frac{(\mathcal{E} - \mathfrak{u})}{k_B T}\}\,\mathrm{d}\mathcal{E} \approx \mathcal{N}_e(T)\exp\{-\frac{(\mathcal{E}_C - \mathfrak{u})}{k_B T}\}\,, \tag{1.9}$$

where

$$\mathcal{N}_e(T) = \int_{\mathcal{E}_C}^{+\infty} g_e(\mathcal{E}) \exp\{-\frac{(\mathcal{E}-\mathcal{E}_C)}{k_B T}\} \mathrm{d}\mathcal{E} = \frac{1}{4}\left(\frac{2m_e^* k_B T}{\pi\hbar^2}\right)^{3/2} . \tag{1.10}$$

Similarly, for total concentration of holes in valence band

$$N_h(T) = \int_0^{\mathcal{E}_V} g_h(\mathcal{E}) \exp\{-\frac{(\mathfrak{u}-\mathcal{E})}{k_B T}\} \, \mathrm{d}\mathcal{E} \approx \mathcal{N}_h(T) \exp\{-\frac{(\mathfrak{u}-\mathcal{E}_V)}{k_B T}\} , \tag{1.11}$$

where

$$\mathcal{N}_h(T) = \int_0^{\mathcal{E}_V} g_h(\mathcal{E}) \exp\{-\frac{(\mathcal{E}_V-\mathcal{E})}{k_B T}\} \mathrm{d}\mathcal{E} = \frac{1}{4}\left(\frac{2m_h^* k_B T}{\pi\hbar^2}\right)^{3/2} . \tag{1.12}$$

For intrinsic silicon, concentration of holes and electrons must be equaled, because total electric charge conserves. Fermi-Dirac distribution at the Fermi level vicinity behaves as odd function. Expression $-(\mathcal{E}_C - \mathcal{E}_F)$, so called activation energy $\mathcal{E}_a$, might be substituted with $\mathcal{E}_G/2$ (a half of energy band gap).

In the case of undoped semiconductor, it is also useful to define intrinsic carrier concentration N_i as electron concentration in the conductive band, or as hole concentration in valence band, i.e. $N_i(T) = N_e(T) = N_e(T)$. After mutual multiplication of equations (1.9), (1.11) and after elementary algebraic operations, we received

$$N_i^2 = \mathcal{N}_e \mathcal{N}_h \exp\{-\frac{\mathcal{E}_G}{k_B T}\} = N_e . N_h , \tag{1.13}$$

or more explicitly

$$N_i = \frac{1}{4}\left(\frac{2k_B T}{\pi\hbar^2}\right)^{3/2} (m_e^* m_h^*)^{3/4} \exp\{-\frac{\mathcal{E}_G/2}{k_B T}\} , \tag{1.14}$$

and numerically casted

$$N_i = 2.5 \left(\frac{m_e^*}{m_0}\right)^{3/4} \left(\frac{m_h^*}{m_0}\right)^{3/4} \left(\frac{T}{300\,K}\right) \exp\{-\frac{\mathcal{E}_G/2}{k_B T}\} . \times 10^{19}\, cm^{-3} . \tag{1.15}$$

At temperature $25\,^\circ C$, it yields $N_i = 7.67 \times 10^9\, cm^{-3}$ for effective masses from Table 1.

Sufficient accuracy for c-Si is reached with empirical formula [conSi] for temperature interval from 275 to 375 K

$$N_i = 9.38 \times 10^{19} \left(\frac{T}{300}\right)^2 \exp\left(-\frac{6884}{T}\right) cm^{-3} . \tag{1.16}$$

At temperature $25\,^\circ C$, relation (1.16) gives $N_i = 8.6 \times 10^9\, cm^{-3}$.

From equation (1.14) is possible to calculate electron chemical potential

$$\mathfrak{u}(T) = \mathcal{E}_V + \frac{1}{2}\mathcal{E}_G + \frac{1}{2}k_B T \ln\frac{\mathcal{N}_h}{\mathcal{N}_e} = \mathcal{E}_V + \frac{1}{2}\mathcal{E}_G + \frac{1}{2}k_B T \ln\frac{m_h^*}{m_e^*}\,. \tag{1.17}$$

The last term is in order of magnitude of $k_B T$, so $\mathfrak{u} \approx \mathcal{E}_V + \frac{1}{2}\mathcal{E}_G$, i.e. Fermi level is positioned near the energy midgap.

Due to thermal expansivity of the crystal lattice energy gap is not constant value, if temperature is altered. Value of energy gap is possible to correct with experimental formula [EnGap]

$$\mathcal{E}_G(T) = \mathcal{E}_G(T = 0\,K) - \frac{\alpha T^2}{T + \beta}\,, \tag{1.18}$$

with fitting parameters $\mathcal{E}_G(T = 0\,K) = 1.166\,eV$, $\alpha = 0.473\,meV/K$, $\beta = 636\,K$. For room temperature $300\,K$, we have $\mathcal{E}_G = 1.12\,eV$.

In the previous text, effective electron and hole masses were introduced. Replacement of free electron mass m_0 in vacuum by effective electron mass m_e^* is a consequence of periodic lattice potential generated by ionic residues. In anisotropic crystals, effective mass is a second rank tensor represented by diagonal square 3×3 matrix. Pure silicon is an indirect-gap semiconductor (see Fig. 1.9). Silicon direct gap (wavenumber is zero) has value $3.2\,eV$, another minima, in directions [100] and in distance $5\,nm$, have well-known energy gap $1.12\,eV$. There are six equivalent band minima, because Si diamond structure is actually face-centered cubic lattice with two-point basis at $(0, 0, 0)$, $(a/4, a/4, a/4)$, where a is a lattice parameter (Fig. **??**). As longitudinal direction is usually considered [100]. Longitudinal electron mass is $m_l = 0.98 m_0$. Both remaining transversal electron masses are the same and they are equal $m_t = 0.19 m_0$. For density-of-state calculations, the final effective mass is given as geometrical mean

$$m_e^* = M_c^{2/3}(m_l m_t m_t)^{1/3}\,, \tag{1.19}$$

where M_c stands for number of equivalent band minima.

Hole mobility is typically much smaller then the electron mobility, therefore the hole term in total conductivity is neglected.

This leads to the final formula of dark conductivity

$$\sigma_{dark} = e\mathcal{N}_e\mu_e \exp\{-\frac{\mathcal{E}_G/2}{k_B T}\} = \sigma_0 \exp\{-\frac{\mathcal{E}_G/2}{k_B T}\}\,, \tag{1.20}$$

where new prefactor σ_0 was introduced.

To simply estimate pure Si dark conductivity, one must know at least crude values of electron and hole mobility. High variability of c-Si, μc-Si microstructural

defects depending on additive concentration results in a wide span of electron mobilities from 800 to 1400 $cm^2/(Vs)$ and hole mobilities from 200 to 500 $cm^2/(Vs)$. As was already mentioned, intrinsic carrier concentration is $8.6 \times 10^9\, cm^{-3}$ at room temperature. This leads to electron dark conductivity $1.4 \times 10^{-6}\, S/cm$ and hole conductivity $4.1 \times 10^{-7}\, S/cm$. The sum of both gives total dark intrinsic conductivity $1.8 \times 10^{-6}\, S/cm$.

Energy gap of amorphous tissue is wider than the gap of crystalline silicon. Moreover, c-Si has in general less defects and dangling bonds and therefore less recombination centers. This implies that intrinsic carrier concentration of c-Si must be greater than concentration of a-Si at the same temperature.

Figure 1.9: *Simplified Si band structure. The lowest band gap is not positioned directly at* Γ *point but in* X *point.*

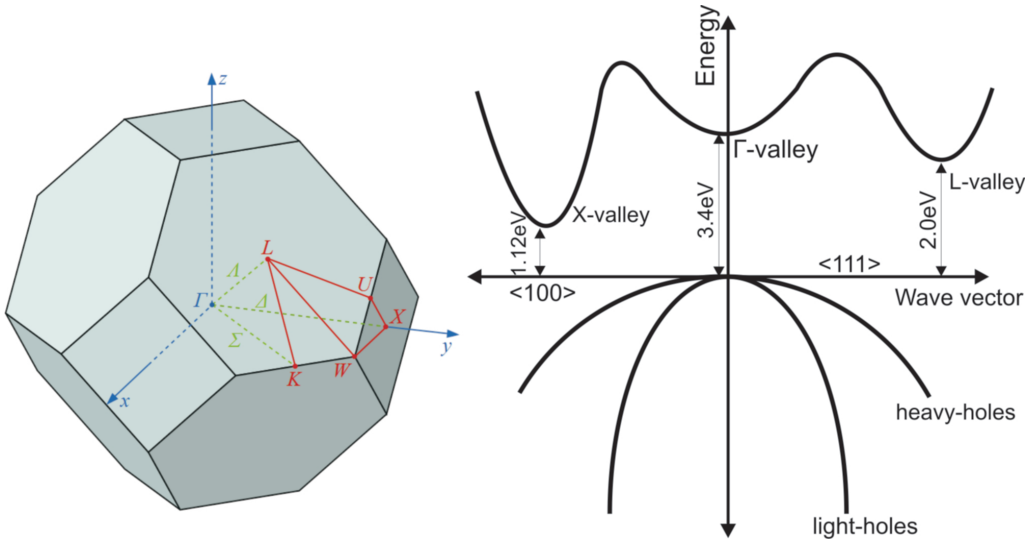

1.4.3 Beer-Lambert law

Light absorption of silicon leads to increase of carrier concentration due to photoelectric effect. When a silicon atom absorbs a light photon and releases electron with kinetic energy equal to the difference of photon energy and bandgap energy. The left-over energy of electron is passed on to the crystal lattice or to other electrons in the form of thermal motion. Electron relaxes to the lower boundary of the conductive band edge.

Neglecting surface reflection, the amount of transmitted light depends upon thickness through the relation

$$I = I_0 e^{-\alpha(\lambda) z}\,, \tag{1.21}$$

where I is light intensity at depth z, I_0 is initial light intensity, α is a coefficient of absorption dependent on light wavelength. The number of excited electrons G per second in a slice of thickness dz and of a unit area, so called carrier generation

G, is

$$G = \alpha \Phi_0 e^{-\alpha z}\,, \tag{1.22}$$

where Φ_0 is photon flux at the surface (number of photons incident on unit area per second).

Assuming monochromatic light with wavelength λ_0, photon flux is

$$\Phi_0 = \frac{I_0}{hc/\lambda_0}\,, \tag{1.23}$$

where h is Planck constant.

Under illumination, amount of charge carriers is raised, which results in increase of total material conductance. Denote ΔN_e contribution to electron volume density caused by light induced carrier generation G. If the mean lifetime of generated carrier is τ, then $\Delta N_e = G\tau$.

Numerically, for illumination $10\,mW/cm^2$ of monochromatic red light ($\lambda_f = 690\ nm$) with photon energy $E_f = 1.8\,eV$ and absorption coefficient $\alpha(\lambda_f) = 10^{-3}\,cm^{-1}$, generation is about $3.5 \times 10^{13}\,cm^{-3}s^{-1}$. Assuming carrier lifetime $\tau = 10\,\mu s$, then contribution to the volume electron density is $3.5 \times 10^{8}\,cm^{-3}$.

Finally, photoconductivity is given as $\sigma_{photo} = e\mu_e G\tau$. Total conductivity is a sum of photo and dark conductivity $\sigma_{tot} = \sigma_{dark} + \sigma_{photo}$.

1.4.4 Thin-film transport equations

Now, we will heuristically attempt to derive basic concept of carrier transport equation. Imagine a model situation depicted at Fig. 1.10. Plane silicon layer of thickness d is exposed to homogeneous electric field E_z in $z-$axis. Layer is illuminated with monochromatic light that incident perpendicularly to the layer's surface. Backward light reflection is neglected. In volume of the differential slice at position z, local Ohm law is well obeyed

$$j_z(\text{drift}) = \sigma_{tot} E_z = e\mu_e N_e(z) E_z\,, \tag{1.24}$$

j_z(drift) is $z-$component of volume density of the drift current.

Carrier drift velocity in vertical direction is

$$\nu = \frac{eE_z\tau}{m_e^*} = \mu_e E_z\,, \tag{1.25}$$

τ labels mean carrier lifetime.

In addition, Poisson electrostatic equation is fulfilled in the slice region

$$\frac{\partial E_z}{\partial z} = \frac{eN_e(z)}{\varepsilon}\,, \tag{1.26}$$

where $eN_e(z)$ is charge density at z coordinate and ε is material permitivity.

We also need to take into account the diffusion of electrons in the direction of concentration decrease. Diffusion current density is given by the Fick's first law

$$j_z(\text{diffusion}) = -eD_e \frac{\partial N_e(z)}{\partial z}\,, \tag{1.27}$$

where D_e represents diffusion coefficient (diffusivity). The definitive current density is the sum of both currents $j_z = j_z(\text{drift}) + j_z(\text{diffusion})$, so

$$j_z = e\mu_e N_e(z) E_z - eD_e \frac{\partial N_e(z)}{\partial z}\,. \tag{1.28}$$

Current density obeys also equation of continuity

$$e\frac{\partial N_e(z)}{\partial t} + \frac{\partial j_z(z)}{\partial z} = 0\,, \tag{1.29}$$

where time derivative of electron concentration can be replaced in stationary state with the sum of the generation and recombination term that varies number of carriers in the slice. We remind that the generation term is equal to $G_e(z) = \alpha\Phi_0 e^{-\alpha z}$. Whereas, the recombination term represents amount of electrons that are depleted due to recombination centers. Electron decrement in the slice is proportional to the probability of dangling bond capture per second and also proportional to the electron concentration $R_e = -eN_e\frac{1}{\tau} = -eN_e S\nu N_{db}$, where the same nomenclature as in (1.1) was used. Thus charge continuity equation has the concrete form

$$-\frac{\partial j_z}{\partial z} = G_e(z) + R_e(z)\,. \tag{1.30}$$

Namely, with the use of Leibniz rule to the drift current term, one obtains

$$D_e\frac{\partial^2 N_e}{\partial z^2} - \mu_e\left(\frac{\partial N_e}{\partial z}\right)E_z - \mu_e N_e\left(\frac{\partial E_z}{\partial z}\right) = \alpha\Phi e^{-\alpha z} - \frac{N_e}{\tau}\,. \tag{1.31}$$

Electric intensity in z-axis direction is defined as minus first derivate of electric potential with respect to z, symbolically $E_z = -\frac{\partial V}{\partial z}$.

Thus electric intensity can be directly substituted with electric potential

$$D_e\frac{\partial^2 N_e}{\partial z^2} + \mu_e\left(\frac{\partial N_e}{\partial z}\right)\left(\frac{\partial V}{\partial z}\right) + \mu_e N_e\left(\frac{\partial^2 V}{\partial z^2}\right) = \alpha\Phi e^{-\alpha z} - \frac{N_e}{\tau}\,. \tag{1.32}$$

In accordance with Einstein relation from kinetic theory, diffusivity is

$$D_e = \frac{k_B T}{e}\mu_e \tag{1.33}$$

Figure 1.10: *Diagram for derivation of electric carrier transport equation.*

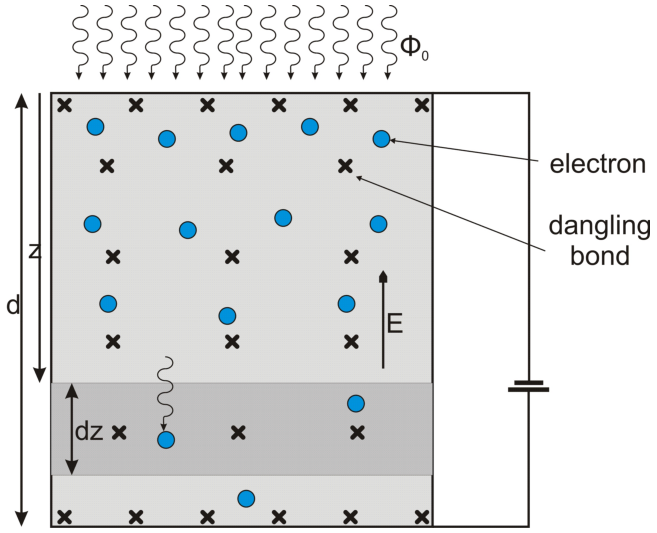

and diffusion length is

$$L = \sqrt{D_e \tau} = \sqrt{\mu_e \tau (k_B T)}\,. \tag{1.34}$$

Differential equations (1.32) and (1.26) determine electric potential V and electron concentration N_e. The solution must obey translation symmetry in directions perpendicular to z-axis (independent on xy position), thus entire problem is one-dimensional. Boundary conditions for electric potential are simple, one of possible options can be $V(z = 0) = V_0$ and $V(z = d) = 0$.

1.5 Tunneling effect in metal-semiconductor interface

The way, how to apply external electric field to the film, is mainly a technical complication. Electric contact is mostly carried out by metal electrodes or by conductive probe (scanning probe microscopy). The behaviour of metal-semiconductor (MS) interface has complex description. We distinguish two type of MS contact: Schottky and ohmic, i.e. whether the volt-ampere characteristic is linear and asymmetric or not.

Assume a metal-semiconductor plane junction in accordance to Fig. 1.11. Vacuum energy is taken as reference zero energy level. Fermi energies of metal and semiconductor are denoted $\mathcal{E}_F$. Let us define work function ϕ of a material as a distance between Fermi level and vacuum level. Physical meaning of the work function is an external energy that electron requires to be released from the material. In addition, suppose a standard semiconductor energy band structure with the valence and conductive band, energy gap $\mathcal{E}_G$ and affinity χ_s. When both

materials are connected, electrons from material with lower work function (in our case metal) flow to the material with higher work function (semiconductor). This continues until the equilibrium of Fermi energy levels are reached. Deformed semiconductor band structure forms a potential barrier V_{bias} that electrons must overcome in order to flow from the metal to the semiconductor. The area of curved energy band is also called depletion region or rectifying region likewise in situation of diode PN junction, because electrons in the conduction band tend to return to the bulk of the semiconductor, where potential energy is lower.

In crude approximation, electric charge density $\varrho(x)$ is constant value $-eN_e < 0$ through the depletion region of width W, for $0 \leq x \leq W$. N_e labels concentration of electrons in the conduction band. In stable state, Poisson equation for electrical potential V in x-axis direction is obeyed in region of the MS interface

$$-\frac{\partial^2 V}{\partial x^2} = \frac{\varrho}{\varepsilon}\,, \tag{1.35}$$

where ε is permitivity of the semiconductor. Trivial integration yields

$$\frac{\partial V}{\partial x} = -\frac{\varrho x}{\varepsilon} + C\,, \tag{1.36}$$

where C is appropriate integration constant equaled to $+\frac{\varrho W}{\varepsilon}$. In a similar way, further integration gives electric potential

$$V(x) = -\frac{1}{2}\frac{\varrho}{\varepsilon}x^2 + \frac{\varrho W}{\varepsilon}x + V_{bias} = -\frac{1}{2}\frac{\varrho}{\varepsilon}(x-W)^2 + \frac{1}{2}\frac{\varrho}{\varepsilon}W^2 + V_{bias} \tag{1.37}$$

that fulfills boundary condition of potential barrier $V(0) = V_{bias} > 0$. At position with coordinate W, we might set $V(W) = 0$ without loss of generality. This results in expression for depletion width

$$W = \sqrt{\frac{2\varepsilon V_{bias}}{\varrho}}\,. \tag{1.38}$$

The needed barrier-surmounting energy ϕ_B is the sum of the built-in potential barrier V_{bias} and the offset between the Fermi level and the conduction band $\phi_B = \phi_m - \phi_s = \phi_m - \chi_s$ [2]. For titanium-silicon contact, semiconductor affinity is $\chi_s = 4.05\,eV$ and work functions are $\phi_{Ti} = 4.33\,eV$, $\phi_{Si} = 4.60 - 4.85\,eV$, thus we obtain for n-type Si $\phi_B = 0.28\,eV$ and for p-type Si $\phi_B = 0.82\,eV$. Positive barrier height for n-type semiconductor means that current flow more easily into the semiconductor. A positive barrier height for a p-type semiconductor means that current flow more easily into the metal. If barrier heights approaches zero, then MS contact is rather Ohmic than Schottky.

[2] Analogically for p-type semiconductor: $\phi_B = \mathcal{E}_G - (\phi_m - \chi_s)$.

Figure 1.11: *Schottky contact between metal and n-type semiconductor. Two separated materials: metal and semiconductor have their own inherent band structure with work functions ϕ_m, ϕ_s. Their junction deforms bands in semiconductor and creates depletion region as in PN diode. Fermi levels of both materials are balanced. Curvature of electric potential depends on type of doping.*

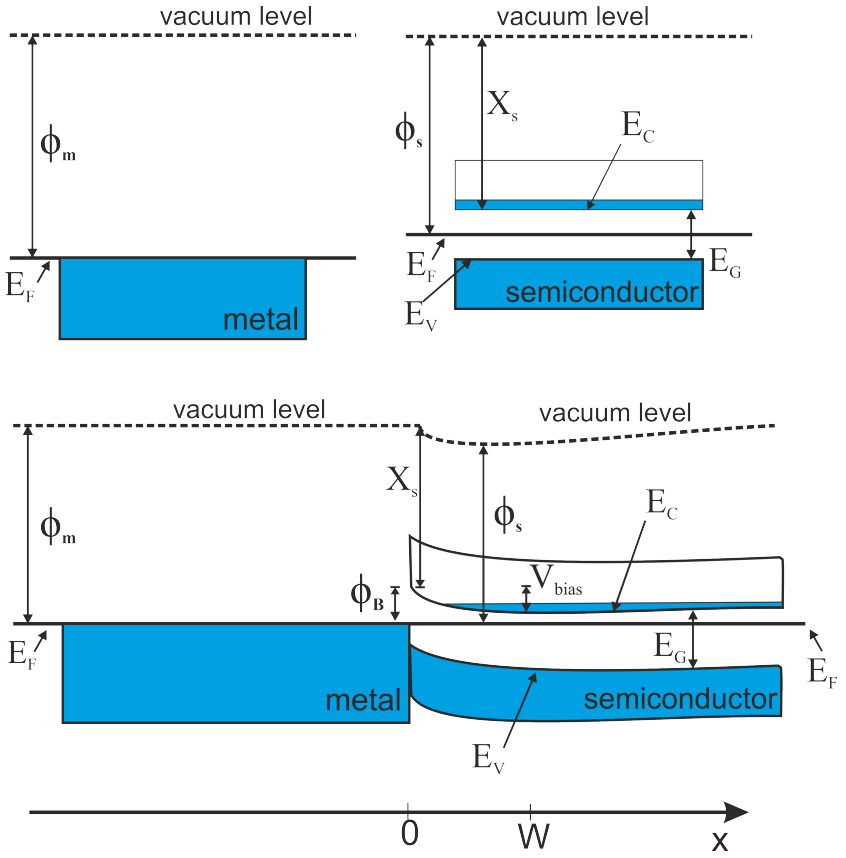

Penetration of electron through the potential barrier is a quantum tunneling effect, when the kinetic energy of electron is lower than the height of potential barrier. Probability of the rectangular-barrier penetration T (transmittance) can be sufficiently approximated for wide barrier $\kappa W \gg 1$ as

$$T \approx 16 \left(\frac{\mathcal{E}}{V_0}\right)\left(1-\frac{\mathcal{E}}{V_0}\right) \exp\{-\frac{2W}{\hbar}\sqrt{2m_e^*(V_0-\mathcal{E})}\}\,, \tag{1.39}$$

where $\mathcal{E}$ is energy of electron, V_0 is height of potential barrier of width W and $\kappa = \sqrt{\frac{2m_e^*(V_0-\mathcal{E})}{\hbar^2}}$. Oppositely, if barrier is narrow $\kappa W \ll 1$, then transmittance is simply

$$T \approx \exp\{-\frac{2W}{\hbar}\sqrt{2m_e^*(V_0-\mathcal{E})}\}\,. \tag{1.40}$$

For semiconductor-metal interface, barrier height V_0 equals to Schottky barrier ϕ_B. As W or ϕ_B tend to zero, afterward transmittance converges to 1.

2. Characterization of the μc-Si structure

2.1 Diagnostic methods and facilities

In order to understand the morphology of the microcrystalline silicon structure in a-Si:H tissue, we need to carry out specimen characterization.

The most widely used technique for surface analysis of submicron structures is scanning electron microscopy (SEM) for its universality and easy use. For our purpose, `Tescan Mira3` microscope with Schottky field emission gun was used.

Another approach to learn further about topography is provided by AFM operating in contact or in tapping mode. AFM belongs to the family of scanning probe microscopes and allows to scan topographical map of the terrain. Its resolution is 1000 better than optical diffraction limit. It gathers information through deviation of laser beam, that points to the deflected probe (Fig. 2.3). AFM probe consists of a cantilever with sharp tip at the end (Fig. 2.11).

Accessible facilities for our experiments were three ambient AFMs: Bruker Dimension Icon [Icon], Bruker Veeco Dimension 3100 and NT-MDT NTegra [Ntegra].

Scan images are usually processed with image processing software such as Gwyddion [Gwyd], NanoScope Analysis, WSxM [WSxM]. Programs are equipped with appropriate tools, e.g. roughness analyzer, cross section profiler, distance and angle measuring tool, grain identifier, 3D visualization, etc.

2.2 Specimen preparation

Specimen were prepared by plasma enhanced chemical vapour deposition[1]. Conditions of fabrication might be summed up in few steps:

1. Inserting a titanium contacted substrate wafer into the vacuum chamber.
2. Evacuation to pressure less than $10^{-6}\,Pa$ under temperature of $T = 300\,°C$.
3. Deposition of incubation amorphous layer: Temperature $T = 250°C$. Hydrogen gas flow $38.4\,cm^3/s$, silane gas flow $3.0\,cm^3/s$. Dilution ratio $R = 12.8$. Time of deposition 11 minutes. Amplitude of RF voltage $325\,V$. Electrical power input $90\,W$. Chamber pressure was $75\,Pa$. Gas residence time $1.8 \times 10^{-3}\,s$ (time that silane molecule spent between electrodes.)

[1] Method was detailedly discussed in 1.

4. Deposition of mixed phase layer: Temperature $T = 250°C$. Hydrogen gas flow $50.0\,cm^3/s$, silane gas flow $1.6\,cm^3/s$. Dilution ratio $R = 31.2$. Deposition time 170 minutes. Amplitude of RF voltage $325\,V$. Electrical power input $20\,W$. Chamber pressure $75\,Pa$. Gas residence time $1.4 \times 10^{-3}\,s$.

Chamber volume was $2 - 2.5\,dm^3$. Circular electrodes had diameter $8\,cm$ and mutual separation distance $2\,cm$. So, the effective chamber volume within electrodes was $0.4\,dm^3$. Specimen cartridge was placed in the center of the electrode. Discharge frequency was $13.56\,MHz$. Substrate was made of Corning glass C7059. Internal identification number of specimen is `KSTM21`. Sample scheme is drawn in the figure Fig. 2.1. For pictures of typical sample, see Fig. 2.2.

Figure 2.1: *Sample design. Some proportions do not correspond to realistic size.*

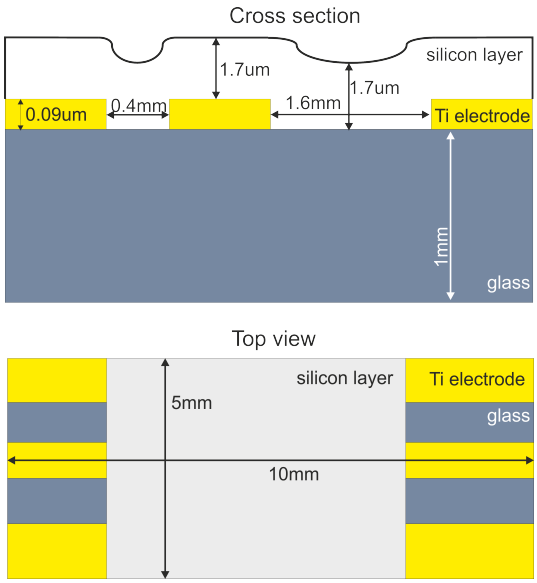

Figure 2.2: *Photos of deposited samples.*

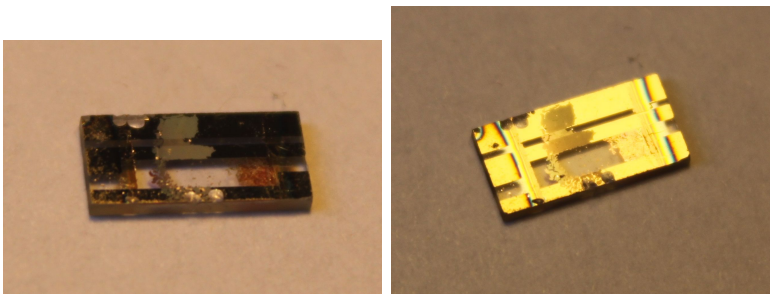

2.3 SEM observations

Wide field images of sample (Fig. 2.13) show that the thin silicon film uniformly covers top side of the glass substrate. Higher magnification discovers that film's structure is composed of grain particles embedded in homogeneous amorphous phase – tissue. Grain particles are silicon crystals. Distribution (disorder-

ing) is more or less random across the upper side of the film. Grain's arrangement depends upon growth conditions and creates small clusters – agglomerates.

Images in Fig. 2.15 show usual circular outline of a grain from top view.

Let us denote the surface area occupied by grains S_{grains}, surface area occupied by amorphous tissue S_{tissue}. The ratio

$$\kappa_S = \frac{S_{grain}}{S_{tissue} + S_{grain}}$$

depends on manufacturing conditions, especially on dilution ratio and on time of deposition. Ratio κ_S is not directly equaled to specimen crystallinity, because it is defined as the volume fraction

$$\kappa_V = \frac{V_{grain}}{V_{tissue} + V_{grain}},$$

where V means volume. However, κ_S is not usually far from κ_V. For the sample studied by SEM, we found out $\kappa_S = 45\%$.

Fig. 2.14 demonstrates layer structure from cross section. Side view of grains discloses its true shape, undetectable from the top view. Probably the best way, how to describe the grain, is a naive idea of an ice-cream [Fejfar2004], that is comprised of a cone and spherically cap. Orientation of capped cone is always with apex towards the glass substrate [Fejfar2004], as a consequence of deposition process.

Typical geometrical parameters, that define size and shape of capped cone, are listed in figure 2.16.

2.4 AFM topography measurements

AFM topographical maps contain a lot of information that can be exploited with image processing software. For instance, spatial visualization of terrain is depicted in Fig. 2.4, 4.2. Amorphous tissue evinces fine granularity in regions within grain particles. Root mean square analysis yields roughness of tissue in interval from 2 to 5 nm in dependence upon type of specimen.

It is also possible to find out the film thickness, by scanning the sharp edge of layer. When AFM tip moves from the film to the surface of electrode, sharp edge of layer need to be crossed. Then photodetector registers high vertical deflection error and significant vertical drop is recorded to the topographical map. After processing several cross section profiles, one receives thickness around 1.4 μm. This value can be compared with result of surface profiler `Tencor Alpha Step`, that has discovered thickness around 1.8 μm.

To verify, whether grains cap is truly spherical, we had decided to extract

Figure 2.3: *Scheme of atomic force microscope operating in the conductive mode.*

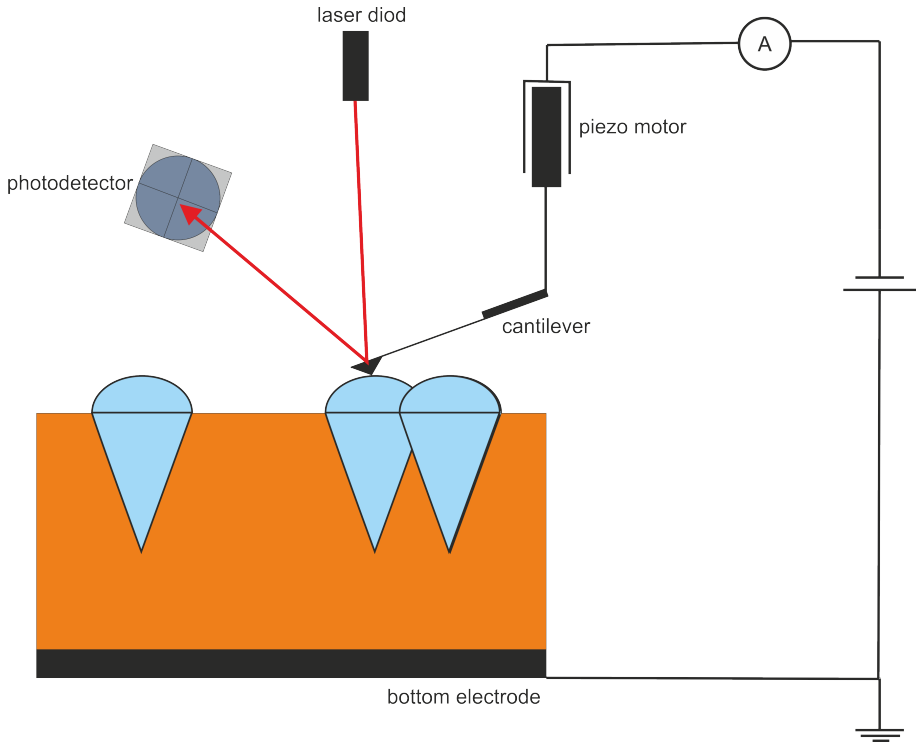

Figure 2.4: *3D topography of film's surface (true proportions).*

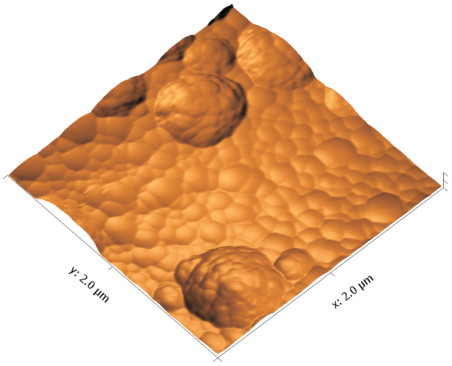

six different cross-section profiles. Profiles were placed equidistantly around the the center of the cap (Fig. 2.5). An osculating circle well approximates the cap. Axial symmetry of the cap, about vertical axis intersecting the cone apex, is also sufficiently fulfilled.

Another issue that we might be interested in is the average cap radius. This parameter is dependent on conditions of layer's growth. In general, it is given by incubation height and film thickness. Radii of 70 caps were measured. Their histogram is showed in Fig. 2.6. Distribution might be compared to Gaussian distribution with mean value around 225 nm

Figure 2.5: *Comparison of six grain profiles with the osculating circle(bold turquoise line). Arc angle of the osculating circle is* 90°.

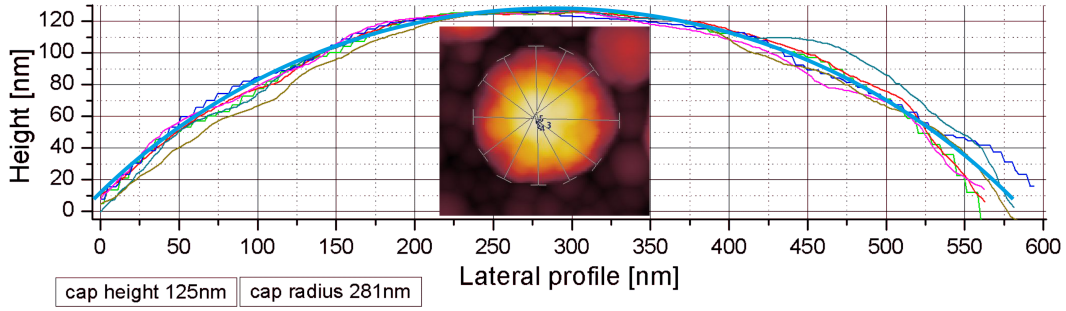

Figure 2.6: *Histogram of cap's radii for sample from Fig. 2.9, Processed date includes grains presented in µc-Si agglomerates. Nanogranular mounds of tissue were strictly excluded. Bin size is* 50 *nm.*

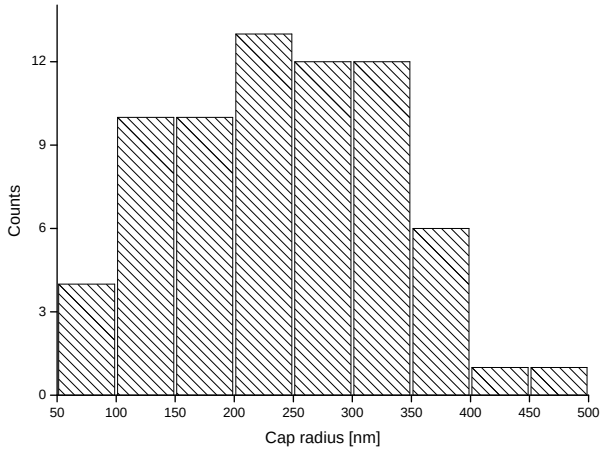

2.5 Estimation of apex semi-angle

Besides the radius, grain's cone is determined by apex semi-angle, henceforth denoted as α. In addition, we need to assume in general that the spherical cap does not have its center of origin positioned exactly at the cone's apex. If we accept this idea, a new enhanced model of grain must be taken in account. Scheme in Fig. 2.7 introduces new angle β, that is defined as the semi-angle of the special spherical sector that generates the cap. This develops preceding model (Fig. 2.16), where the cap was given by the apex semi-angle α. The cone's edge served as a radius of the spherical sector. Consequently, preceding model was a special case of the new one, where $\beta := \alpha$. However, it is no longer truth and we heuristically anticipate, that angle β should be roughly 1.5–3 times greater, than the angle α, as shows image Fig. 2.17.

After basic geometrical consideration, we may write following expressions for the height of cone v_{cap} and for the radius of spherical sector R_{cap}

$$R_{cap} = \frac{r_{cap}}{\sin\beta}, \quad v_{cap} = R_{cap}(1-\cos\beta) = r_{cap}(\frac{1}{\sin\beta} - \frac{1}{\tan\beta}), \tag{2.1}$$

Figure 2.7: *Enhanced geometrical model of the microcrystalline grain. Spherical cap is set by sphere sector with semi-angle β. Underneath cone has different apex semi-angle α Dashed curve is hypothetical (incorrect) cap given by sphere sector with semi-angle α.*

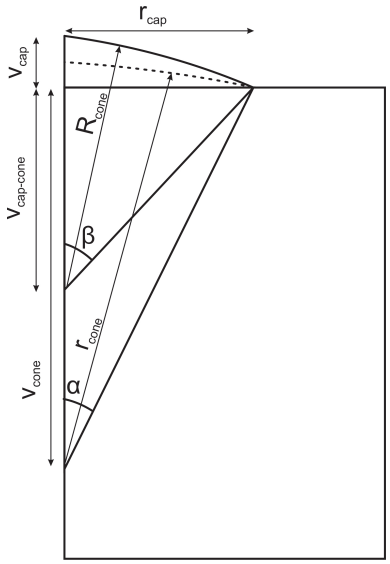

where the notation defined in Fig. 2.7 is respected. So, the cap radius is directly proportional to height of the cap, $v_{cap} = k.r_{cap}$. Comparison of expressions (2.1) yields the formula for slope k

$$k = \frac{1}{\sin\beta} - \frac{1}{\tan\beta}\,, \tag{2.2}$$

After elementary operations, implicit equation for semi-angle β is received

$$k\sin\beta + \cos\beta = 1\,. \tag{2.3}$$

In graph Fig. 2.8, cap height is plotted versus cap radius for several grains. Data were fitted with a linear function ($y = k.x + q$). We have obtained the slope $k_1 = (0.398 \pm 0.03)$ and interception $q_1 = (-24 \pm 6)\,nm$, and coefficient of determination $R^2 = 0.94$. Value of shift in $y-$axes (i.e. interception q) is not significant because the surface plane was not flattened to zero.

The same experiment was carried out with a different sample and different AFM (see Fig. 2.9). Resultant fit constants are: $k_2 = (0.53 \pm 0.02)$, $q_2 = (-63 \pm 4)\,nm$ and $R^2 = 0.95$.

With knowledge of slopes k_1, resp. k_2, numerical solution of equation (2.3) was found $\beta_1 = 43.4°$ for sample in Fig. 2.8 and $\beta_2 = 56.7°$ for sample in Fig. 2.9.

Another feasible method, how to obtain angle β, is demonstrated in Fig. 2.10. Method is based on manual fitting of cap profile with an osculating circle. Then, we may easy determine the arc angle. But, resultant apex angle is heavily depen-

Figure 2.8: *Dependence of cap height on cap radius. Only radii of selected solitary grains were measured. Data in graph were obtained as the mean of radii in x and y directions. Result of NT-MDT AFM. A standard silicon cantilever was used with tip's curvature radius* $\approx 35\,nm$

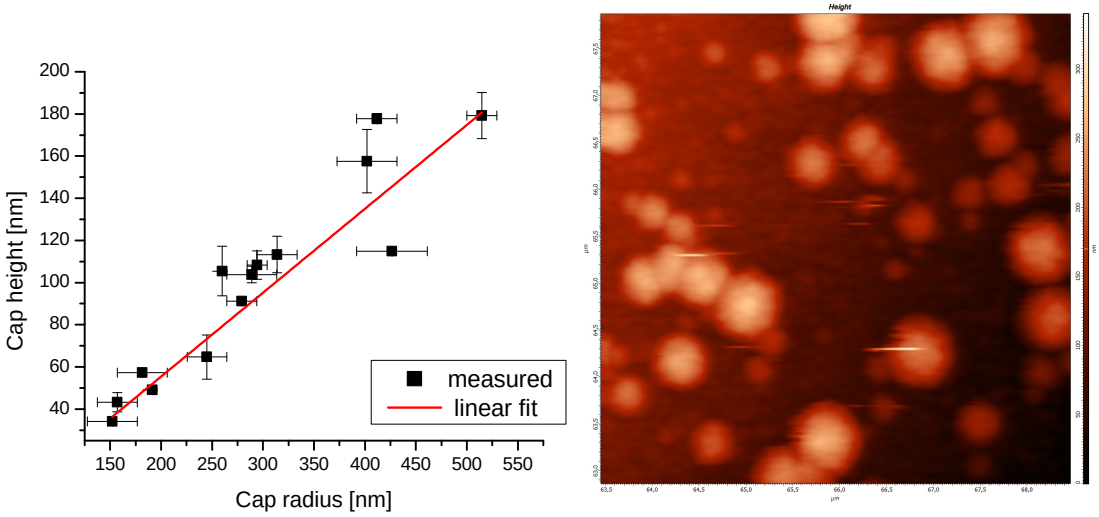

dent on the choice of radius, which defines deviation margins at grain boundaries. Such method gives semi-angle β in range from 30 to 46 degrees.

Apex angle of the cone could be determined from picture Fig. 2.17, that was taken by cross-sectional transmission electron microscope (XTEM). One acquires value $\alpha \approx 18.5°$.

Figure 2.10: *Osculating circle fitting the grain cap hump.*

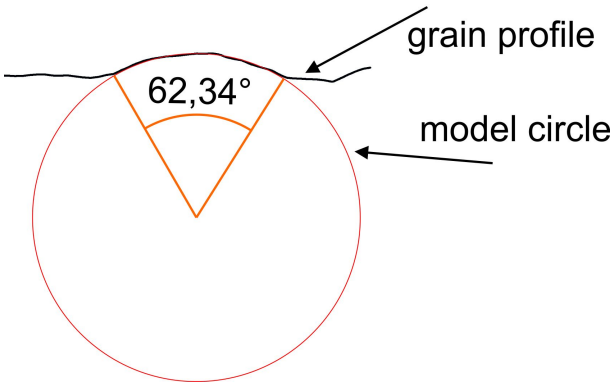

Figure 2.9: *Dependence of cap height on cap radius. Different sample than in Fig. 2.8. Inset shows the region that was used for data processing. Diameters were taken in convenient directions to avoid distortion, caused by grain's agglomeration. Result was obtained with Bruker Veeco Dimension 3100 AFM. A cantilever with diamond coating was used. Radius of tip's curvature was* $\approx 100\,nm$.

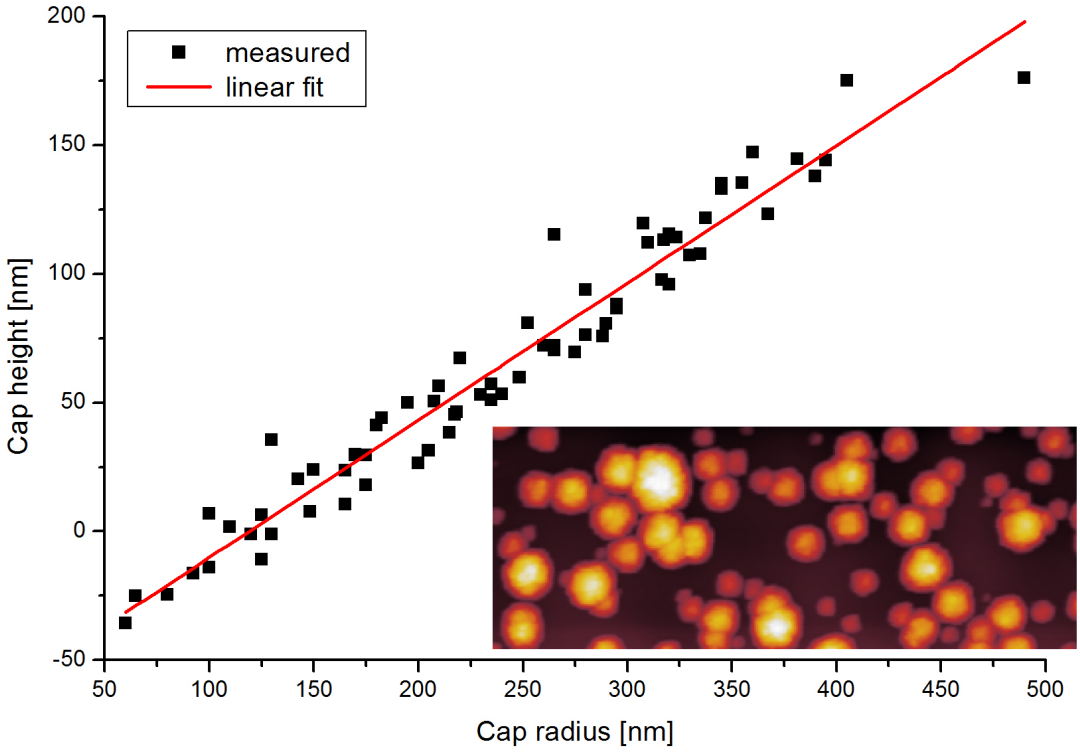

Figure 2.17: *Cross section image of μc-Si film obtained by XTEM. Adopted from [Bronsveld].*

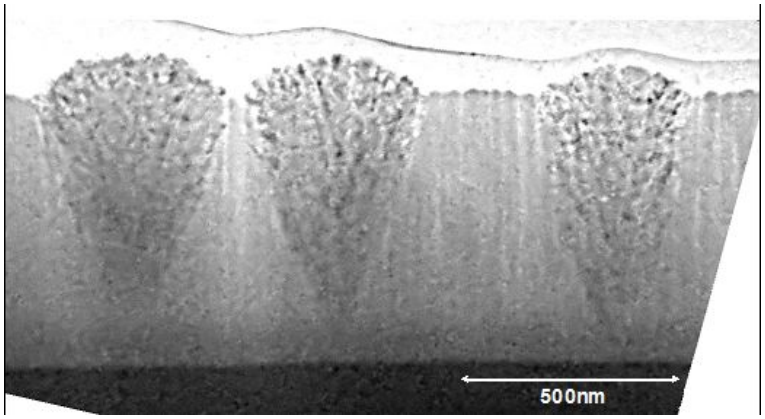

Figure 2.11: *AFM probe with three main parts: Holder, cantilever and tip. Cantilever's tip blunting after several scans.*

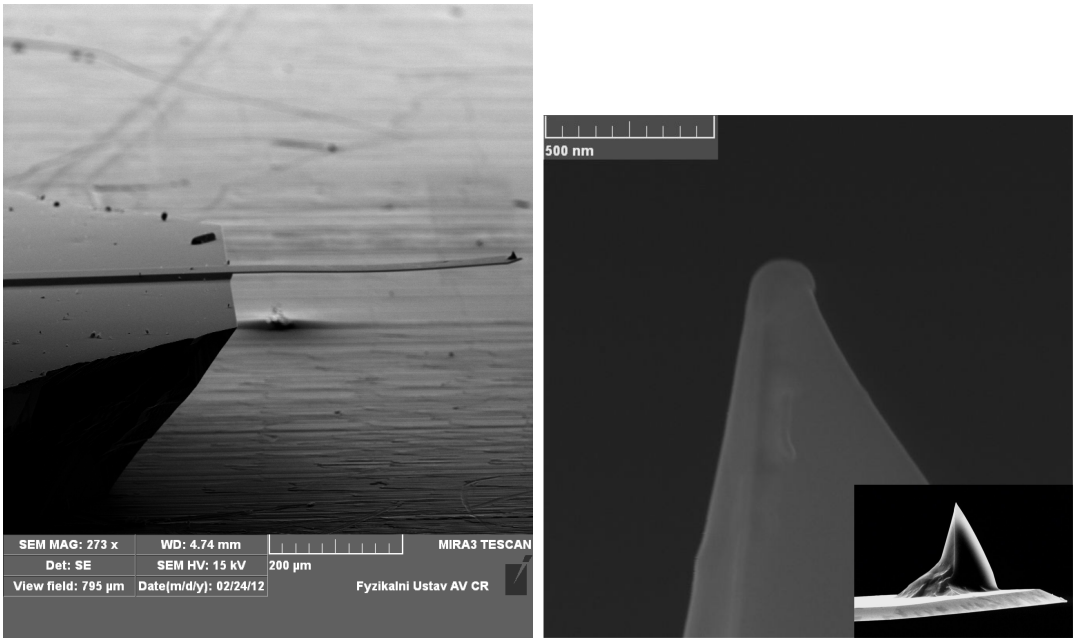

Figure 2.12: *Top view of film and cantilever. The photograph was taken by optical microscope attached to head of Bruker Dimension Icon AFM. Black stripe on the right is cantilever's holder. White background on the left is backward reflections from Ti electrode. In the middle is the cantilever with laser spot. Dotted stain is heterogeneous structured film of µc-Si and a-Si.*

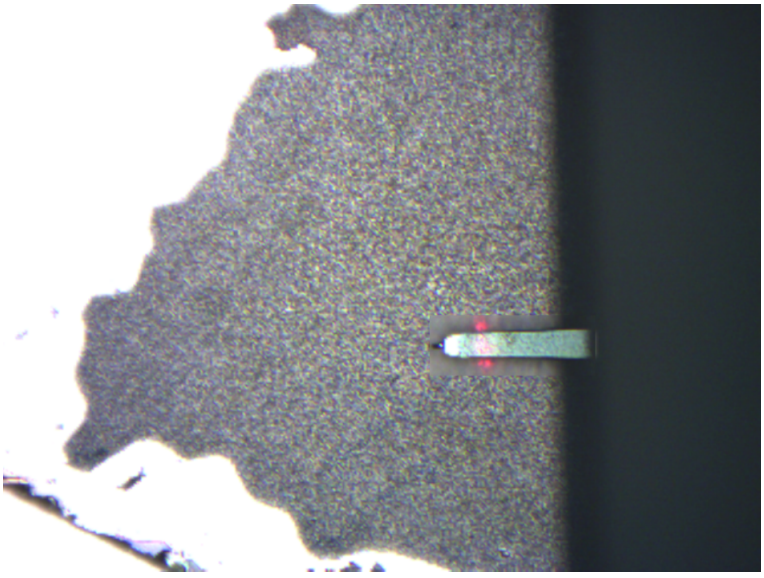

Figure 2.13: *Wide field SEM image of the Si layer.*

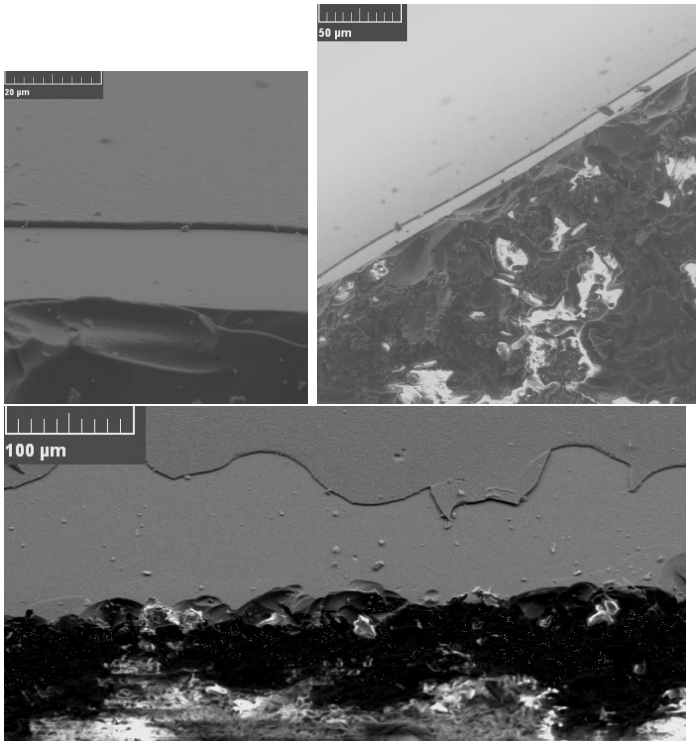

Figure 2.14: *Cross section SEM image of the Si layer. Magnification* 65×10^3 *and* 18×10^3*, working distance* $3.05\,mm$*, voltage* $9\,kV$*. The height of the layer could be estimated as 1-2* μm*.*

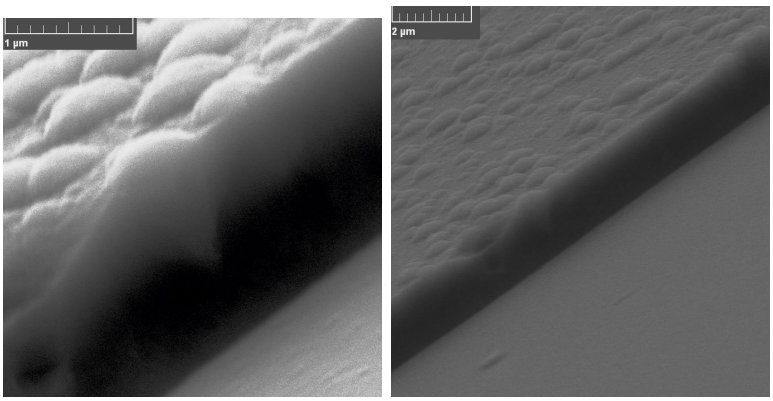

Figure 2.15: *SEM image of Si layer from the top view.*

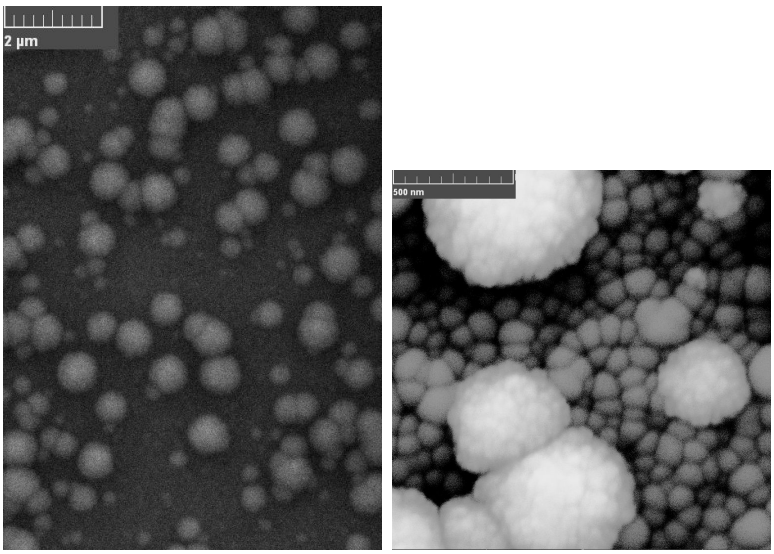

Figure 2.16: *Simple model of Si microcrystalline grain. Values of geometrical parameters are related to chapter 3.*

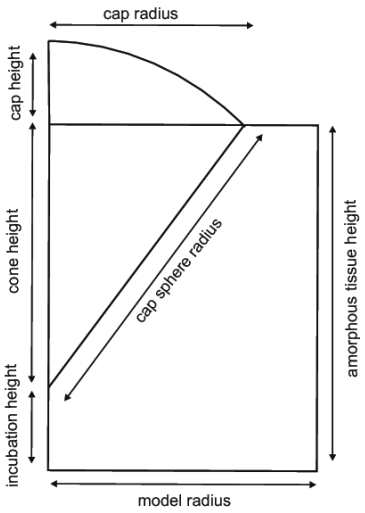

3. Finite element modeling

In our study we investigate local electric properties of grain structured thin film. Fundamental problem is to find essential electric quantities such as electric potential, spatial current density and density of power dissipation as functions of radius-vector. Complex two-dimensional geometry of the grain radically complicates detailed theoretical predictions and analytical calculations, even if the geometrical situation evinces axial symmetry. Perhaps, in some trivial cases accurate solution can be found as variation on Bessel functions or with the use of suitable conformal mapping. For instance, if upper electrode fully covers grain's cap or if the upper electrode touches the cap on the top at the only one point.

Finite element analysis provided by `Comsol Multiphysics` simulation software [Comsol] allows simpler and more practical approach. Comsol is equipped with wide repertoire of specific physical tasks covering large application field. Modeling of electric currents are performed in AC-DC simulation module (section Electric currents), while charge carrier transport is carried out in Chemical Species Transport module (section Transport of Diluted Species) and electromagnetic waves propagation in Radio Frequency module (section Electromagnetic waves). Detailed description of finite element method is beyond the scope of this text. We refer interested readers to [Polycarpou], [Jianming] and to other books concerning the topic.

It is to be noted that very similar simulations were done in the work [Kalusova].

3.1 Equations for a simple electric model of grain

First step, on the way to comprehend the local electric charge transport through the microcrystalline silicon grain, is to solve basic stationary current task for given electric potential at boundaries. In figure Fig. 3.1, simple grain geometry consisting of capped cone, is shown. Cone apex semi-angle α and spherical cap sector semi-angle β are angles describing the grain's shape. Angle γ defines an effective contact area that the upper electrode (probe's tip) touches the grain cap. Boundary lines in cross section view are labeled by letter Γ with appropriate indices. Revolution of cross section about axis of symmetry creates from lines Γ_1, Γ_2, Γ_3, Γ_4, Γ_5 surfaces, but boundaries Γ_6, Γ_7 remain line segments.

Bottom macroscopic electrode is adjacent to grain incubation layer. We assume constant electric potential on the top and on the bottom electrode as boundary conditions. Electric potential on bottom electrode is set up to zero (ground) and on top electrode to value $V_0 \geq 0$, typically from 1 to $10\,V$. Conventional

current then flows from the cap contact to the ground electrode[1].

Electric conductivity of the capped cone is denoted as σ_c (approximative value of crystalline silicon) and is constant in domain $\mathcal{G}$. Similarly, the rest of layer (domain $\mathcal{A}$) has constant conductivity σ_a (approximative value for amorphous silicon). For dielectric constants ε_{r-C}, ε_{r-A} of the grain and tissue, the same restrictions hold as for conductivity.

Laplace equation for electric potential V governs interior of both domains. In cylindrical coordinates, it has form

$$\frac{1}{R}\frac{\partial}{\partial R}\left(R\frac{\partial V}{\partial R}\right)+\frac{\partial^2 V}{\partial z^2}=0\,, \tag{3.1}$$

where R stands for radius, z labels height. Null right hand side stands for no bound space charge in volume of domains.

Electric intensity is generated as

$$\mathbf{E}=-\frac{\partial V}{\partial R}\mathbf{e}_R-\frac{\partial V}{\partial z}\mathbf{e}_z\,, \tag{3.2}$$

where $\mathbf{e}_R, \mathbf{e}_z$ denote unit vectors in direction of radial distance, resp. in direction of z-axis.

On the top of that, equation of charge continuity in stationary state for volume current density $\mathbf{j}$ must be also fulfilled

$$\frac{1}{R}\frac{\partial}{\partial R}(R\,j_R)+\frac{\partial j_z}{\partial z}=0\,. \tag{3.3}$$

j_R, j_z are coordinates of current density in cylindrical coordinate system. A material relation that links up current density and electric field intensity (local Ohm's law) through material properties is

$$\mathbf{j}=\sigma\mathbf{E}\,. \tag{3.4}$$

Equation (3.3) is redundant because insertion of material relation into continuity equation lead quickly to Laplace equation.

Generally, Maxwell partial differential equations for electro-magnetic field hold in domains. At boundaries, equations must be completed with additional relations treating continuity resp. discontinuity of field quantities.

Divide of permittivity, on conical skirt surface $\Gamma_{\mathcal{AG}}$ between amorphous and crystalline silicon, creates thin layer of surface bound charge. Surface density of bond charge η is described by equation

$$\mathbf{n}\cdot(\mathbf{D}_{\mathcal{A}}-\mathbf{D}_{\mathcal{G}})=\eta\,, \tag{3.5}$$

[1]Model does not involve local anodic oxidation.

where $\mathbf{D}_{\mathcal{A}}$, $\mathbf{D}_{\mathcal{G}}$ are electric field displacement in amorphous tissue, resp. in the grain.

$$\mathbf{n} = \cos\alpha\,\mathbf{e}_R - \sin\alpha\,\mathbf{e}_z = \cos\alpha\frac{x}{\sqrt{x^2+y^2}}\mathbf{e}_x + \cos\alpha\frac{y}{\sqrt{x^2+y^2}}\mathbf{e}_y - \sin\alpha\,\mathbf{e}_z\,, \quad (3.6)$$

is a normal vector perpendicular to the cone's skirt. Vector $\mathbf{n}$ points into amorphous tissue. α is the apex semi-angle. Electric intensity is related to electric field displacement through isotropic linear material relations $\mathbf{D}_{\mathcal{A}} = \varepsilon_{\mathcal{A}}\mathbf{E}_{\mathcal{A}}$, $\mathbf{D}_{\mathcal{G}} = \varepsilon_{\mathcal{G}}\mathbf{E}_{\mathcal{G}}$, where $\varepsilon_{\mathcal{A}}$, $\varepsilon_{\mathcal{G}}$ are permitivities of tissue, resp. grain[2].

Tangential component of electric field intensity at permittivity drop is preserved

$$\mathbf{n} \times (\mathbf{E}_{\mathcal{A}} - \mathbf{E}_{\mathcal{G}}) = 0,. \quad (3.7)$$

Furthermore, analogical equation for surface current density $\mathbf{j}_{surface}$ holds

$$\mathbf{n} \times (\mathbf{H}_{\mathcal{A}} - \mathbf{H}_{\mathcal{G}}) = \mathbf{j}_{surface}\,, \quad (3.8)$$

where $\mathbf{H}_{\mathcal{A}}$, $\mathbf{H}_{\mathcal{G}}$ are magnetic fields intensity in appropriate domains. In stationary state,[3] magnetic field is null in the entire model, therefore no surface current density will be observed.

At boundaries Γ_2, Γ_3, Γ_4 we demand current insulation

$$\mathbf{n} \cdot \mathbf{j} = \mathbf{0}\,, \quad (3.9)$$

where $\mathbf{n}$ is a unit normal vector pointing out of the model system.

At boundaries Γ_6, Γ_7 no condition is applicable due to revolution about the axis of symmetry.

Our system has limited size[4] in horizontal plane, that is coincident with the length of the boundary Γ_5. This size compromises two contradictory requirements. If the system radius is too large, then calculation would not be effective. On the other hand, if system radius is too small, simulation would suffer from fringe effect.

Typical geometrical grain parameters together with selected model parameters are listed in table Tab. 2.

[2] In other words, discontinuity of normal component of electric field displacement equals bound surface charge at boundary.

[3] long time after start-up transient effects

[4] Further in the text, this size is denoted as a model radius or model edge.

Table 2: **Model parameters**

System radius	0.6-3.5 μm
Cone apex semi-angle α	20°
Spherical cap sector semi-angle β	50°
Effective contact semi-angle γ	5°
Incubation height $v_{incubation}$	0.2 μm
Cap radius (from top view) r_{cap}	0.255 μm
Cone height v_{cone}	0.7 μm
Radius of the osculating sphere R_{cap}	0.33 μm
Top contact potential V_0	1 V
Bottom contact potential	0 V
Microcrystalline grain conductivity	1×10^{-5} S/cm
Amorphous tissue conductivity	1×10^{-8} S/cm
Permittivity of grain	11.8
Permittivity of amorphous tissue	11.8

3.2 Distribution of electrical potential and intensity for sharp and rounded apex

In Fig. 3.3, there are final distributions of current density, electric field intensity, respectively electromagnetic power dissipation. Electric potential in capped cone is almost constant, as a consequence of high cone's conductivity in comparison to low conductivity of amorphous tissue. Analogue of this situation can be solid metal body immersed into almost non conductive liquid. This holds true, if difference between amorphous and crystalline conductivity is more than 3 or 4 orders of magnitude. Low gradient of electric potential in grain is responsible for low electric intensity in the grain's volume. Therefore, electric intensity is mostly spread in amorphous tissue.

Current density is a product of electric intensity and conductivity. Fig. 3.3 says in fact, that difference in conductivity of grain and tissue is larger, than the difference of electric fields in both domains, therefore current density can prevail in the grain. Thus, vector field of current density and electric intensity complements each other.

Local density of electric resistive loss p in ohmic material (so called Joule heat) is

$$p = \mathbf{j} \cdot \mathbf{E} = \sigma E^2 \tag{3.10}$$

with standard notation. Total volume resistive loss P is an integral of density loss over entire model volume $\Omega = \mathcal{G} \bigcup \mathcal{A}$, or is equaled to the sum of integrals over grain domain $\mathcal{G}$ and tissue domain $\mathcal{A}$.

$$P = \int_\Omega p(\mathbf{r})\,\mathrm{d}^3 r = \int_\mathcal{G} \sigma_\mathcal{G}\, E^2_\mathcal{G}(\mathbf{r})\,\mathrm{d}^3 r + \int_\mathcal{A} \sigma_\mathcal{A}\, E^2_\mathcal{A}(\mathbf{r})\,\mathrm{d}^3 r\,, \tag{3.11}$$

where $\mathbf{r}$ is a position-vector; $\sigma_{\mathcal{G}}$, $\sigma_{\mathcal{A}}$ are conductivities of crystalline grain, resp. amorphous tissue.

It is a known fact that electric surface charge is condensed at spike and electric intensity is theoretically divergent at the tip[5]. Besides this, incubation layer is shortest distance between cone's skirt and bottom electrode. Hence, segment line connecting cone apex with bottom electrode is the most effortless trajectory for electrons to surmount resistive barrier of amorphous tissue.

Electric potential contours in incubation layer are compressed within the apex and bottom electrode. Steep descent of potential leads to high electric field at that place.

Altogether lead us to the idea that major power dissipation should be concentrated bellow cone apex.

This is documented in Fig. 3.3 with wireframe mesh. Value of power dissipation and affected volume, surrounding the apex, are strongly dependent on mesh quality. For instance, if maximum element size is less than $0.001\,\mu m$, then resistive loss at apex is $2 \times 10^{11}\,W/m^3$. Increase of mesh quality at apex (i.e. decrease maximum element size) results dramatically in explosion of dissipation (hyperbolically in log-scale). Besides, power loss is also increased with the height of incubation layer.

In order to ensure convergent power loss at cone apex, the sharp cone's spire was artificially rounded with cubic Bezier curve (see Fig. 3.2). If derivation (slope) of the Bezier curve is zero at apex point[6], afterward electric intensity is convergent, when maximum element size approaches zero. For rounded apex, power loss is typically $2.6 \times 10^8\,W/m^3$. In bulk of grain, it is from 1 to $3 \times 10^5\,W/m^3$. In bulk of amorphous tissue, power loss is from 1 to $2 \times 10^6\,W/m^3$. Total electric resistive losses in the capped cone for bias voltage $1\,V$ is $6.9 \times 10^{-14}\,W$ and for domain of amorphous tissue, it is $2.6 \times 10^{-12}\,W$.

Units of pikowatts are rational values in concordance with macroscopic Joule's law for resistive loss

$$P = IV\,. \tag{3.12}$$

If AFM tip's current I is in orders of pikoamperes under bias voltage $V = 1\,V$, then power dissipation is obtained in order of pikowatts.

These numbers instantly answered the question, whether resistive losses are sufficient heat source to increase temperature in cone apex region by at least about $1\,K$. If yes, then power dissipation must be equalled to output heat flux. Suppose model bias voltage $10\,V$ and model radius $2\,\mu m$. Corresponding power loss is $P = 2.6 \times 10^{-10}\,W$. Assume temperature gradient from boundary Γ_6, Γ_7

[5]Every real spike has finite tip curvature, so it is not physically possible.

[6]Bezier curve intersects the axes of symmetry perpendicularly.

Figure 3.1: *Cross section of the grain with terminology linked to the boundary conditions. Angle α is the apex semi-angle, β is the semi-angle of spherical sector forming the grain's cap, γ is the angle that defines effective electric contact area. Red curves show placement of electrodes.*

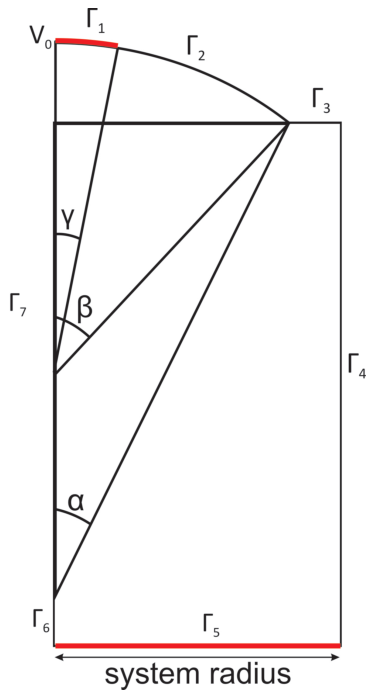

Figure 3.2: *Qualitative solution for simple electric Laplace problem with two electrodes. Cone apex is curved. Color scale corresponds to the electric potential range from 0 to 1 V. Contours correspond to electric equipotential levels. Arrows in the left image display current distribution. Arrows in right image show electric intensity distribution. Arrow's length is in logarithmic scale.*

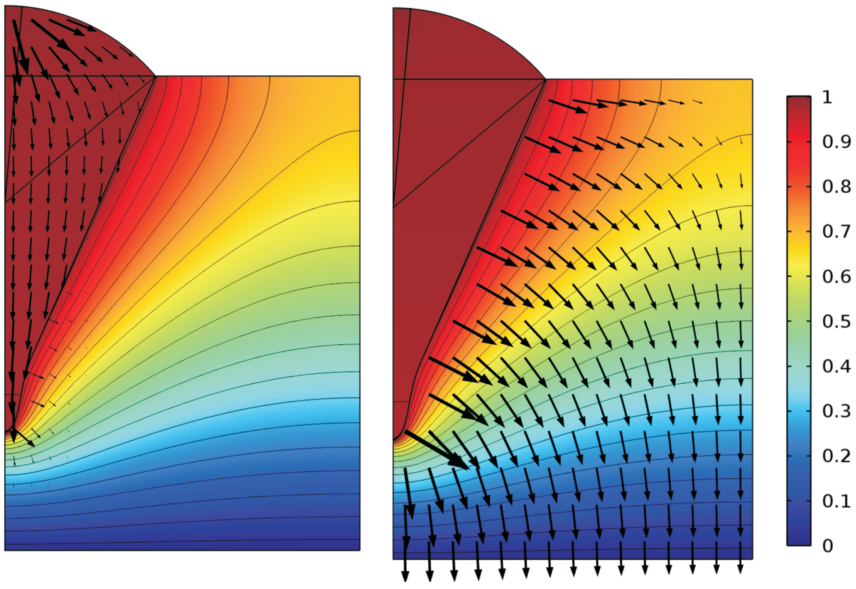

Figure 3.3: *The same task as in the previous figure Fig. 3.2, but the cone apex is a sharp spire for this case. Last image with scale shows power dissipation density, caused by resistive losses in material. Wireframe net reflects model mesh. Cone apex creates a mathematical singularity that results in divergence of electric intensity. Size of the power lossy stain, located bellow the apex, is highly dependent upon mesh quality. Finer mesh causes smaller stain's size and higher values of electric intensity at apex. Cut-out shows power dissipation in vicinity of tip's contact.*

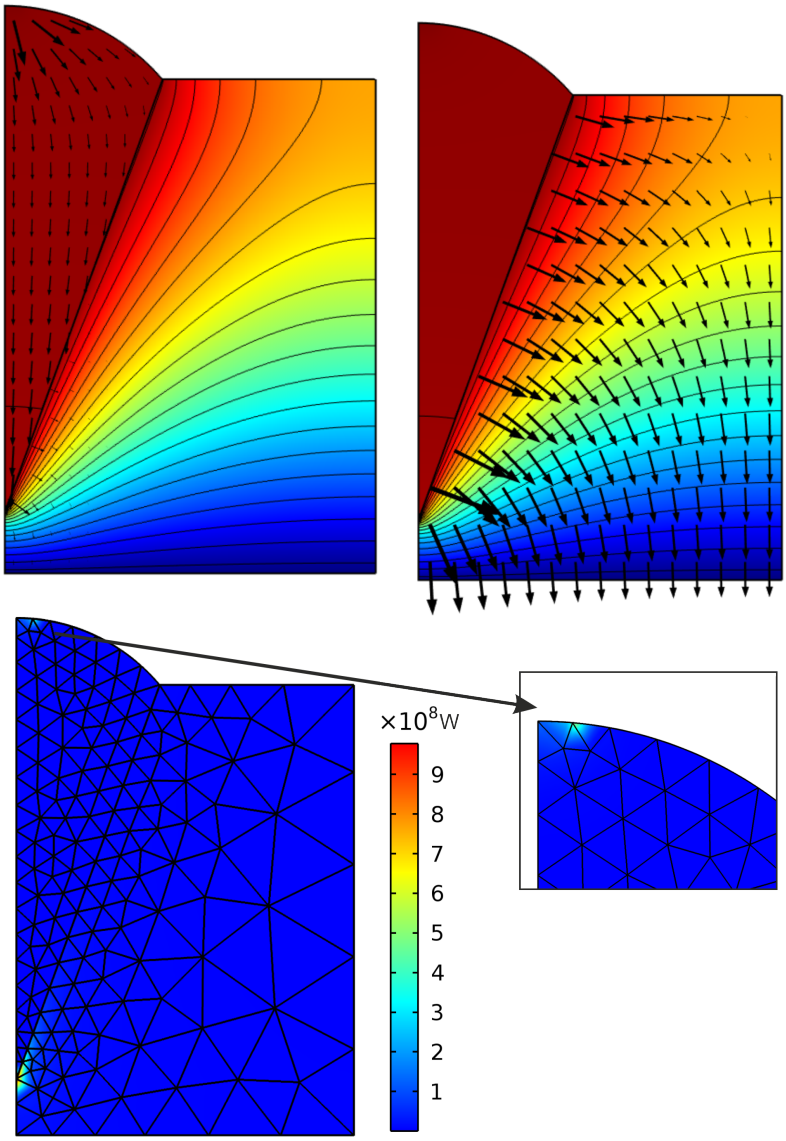

to boundary Γ_4 (Fig. 3.1) equalled to $\Delta T/\Delta R = 1\,K/2\,\mu m$. The whole surface of model covers area around $S = 40\mu m^2$. Thermal conductivity of silicon is $k = 1.3\,W/(K.cm)$. Hence, the output heat flux is $\Phi = k\frac{\Delta T}{\Delta R}S = 2.6 \times 10^{-3}\,W$. We see $P \ll \Phi$. Difference of 7 orders of magnitude speaks for all. We do not have to involve any temperature variation to the model.

Total current, that flows from the top electrode to the bottom electrode, is always equalled to a surface integral of z-component of current density over bottom electrode

$$I = \int_\Sigma \mathbf{j} \cdot \mathrm{d}\mathbf{S} = \int_0^{R_{model}} \int_0^{2\pi} j_z\, R\, \mathrm{d}\varphi\, \mathrm{d}R = 2\pi \int_0^{R_{model}} j_z\, R\, \mathrm{d}R\,. \tag{3.13}$$

Σ denotes surface of the model's bottom basement. Surface element $\mathrm{d}\mathbf{S} = \mathrm{d}S\,\mathbf{n} = R\mathrm{d}\,\varphi\,\mathrm{d}R\mathbf{n}$ has normal vector $\mathbf{n} = \mathbf{e}_z$, φ is an azimuthal angle of cylindrical coordinate system. Z-coordinate of current density is generally function of radius R and angle φ. Thus the penultimate integral holds for general asymmetrical model arrangement, while the last integral is used for the case of axial symmetry.

For bias voltage $1\,V$, total current is $2.64\,pA$, resp $2.49\,pA$ for the case of sharp, resp. rounded apex. Parametric dependence of total current upon voltage[7] is a linear function with zero intercept and slope $k_{sharp} = 2.64\,pA/V$, $k_{rounded} = 2.49\,pA/V$. Simple Ohm's law $I = \frac{U}{R}$ claims that current is a linear function of voltage with slope equalled to reciprocal value of resistance. Total power loss for strictly ohmic conductor suits relation $P = \frac{U^2}{R}$, i.e. power dissipation is a parabola scaled by reciprocal value of resistance.

It is high time to make a remark on electric intensity and potential. Imagine a homogeneous film of thickness $d = 1\,\mu m$ biased to $V = 1\,V$. Internal electric intensity is $E = V/d = 10^4\,V/cm$. Breakdown field of crystalline silicon is approximately $3 \times 10^5\,V/cm = 30\,V/\mu m$.[8] Electric intensity at rounded cone apex under bias voltage $1\,V$ is $11,8\,V/\mu m$ and for $3\,V$ it overruns breakdown limit with value $40\,V/\mu m$. We remind that voltage from 3 to $4\,V$ is critical penetrative voltage from experimentally received IV curves (see section 4.5).

Potential and intensity are function of radius R and height z. Electrical potential as a function of radius for fixed $z-$coordinate is plotted in Fig. 3.4. Bottom electrode was set as null height. Profiles are taken: at amorphous tissue height $0.9\,\mu m$, at twice of incubation height $0.4\,\mu m$, at $0.98\times$cone's apex height $0.2\mu m$ and at $0.1\times$incubation height $0.02\,\mu m$. Interior of grain is at constant potential $\approx 0.95\,V$. Outside of the grain potential hyperbolically decreases with asymptote at zero.

Analogical profiles of electric intensity, taken at the same heights for model

[7] Further in text, we call the dependence on some parameter simply "parametric sweep".
[8] See table Tab. 1.

of rounded apex, are shown in a graph in Fig. 3.5. Intensity has two nonzero coordinates E_z, E_R. Radial coordinate of intensity fast converges to zero for $R \to 0$ and also for $R \to \infty$ Vertical coordinate of intensity increases, as we move from $R = \infty$ to the cone's skirt, where it falls to zero. This is the reason, why profiles do not begin at zero radius.

3D expression of potential is presented in picture Fig. 3.6.

Figure 3.4: *Electric potential as a function of radius R at fixed heights. Grain and cone apex is at constant potential* $0.95\,V$. *Outside the grain, potential hyperbolically decreases to zero.*

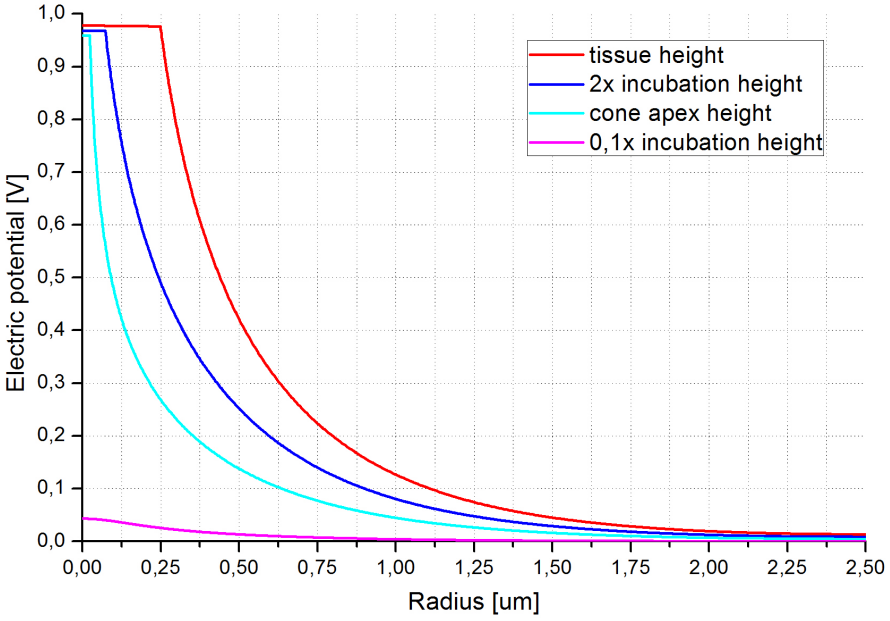

Parametric sweep of total current upon the conductivity of amorphous tissue is depicted in Fig. 3.7. Conductivity runs over 6 orders of magnitude from 10^{-8} to $10^{-2}\,S/m$. Sweep was calculated at bias voltage of $1\,V$

Typical experimental values of dark current are $10\,fA - 10\,pA$ that complies with conductivity range from $5 \times 10^{-11}\,S/cm$ to $5 \times 10^{-8}\,S/cm$. Trend of curve is linear in log-log scaled graph, with end point about $2 \times 10^{-5}\,S/m$. Linear function in log-log graph means that true dependence in Cartesian coordinates is some power of conductivity[9].

3.3 Impact of deposition conditions

In accordance to Fig. 2.7, grain's geometry is fully described with following parameters: α, β, cap radius, incubation height. Cap radius can be also substituted with cone's height or with radius of cap's sphere. Incubation height is interchangeable for height of amorphous tissue. Model radius is not a restrictive

[9] $\log y = k \log x + q \Rightarrow y = Cx^k$.

Figure 3.5: *Radial and vertical component of electric intensity as a function of radius at several fixed heights above bottom electrode.*

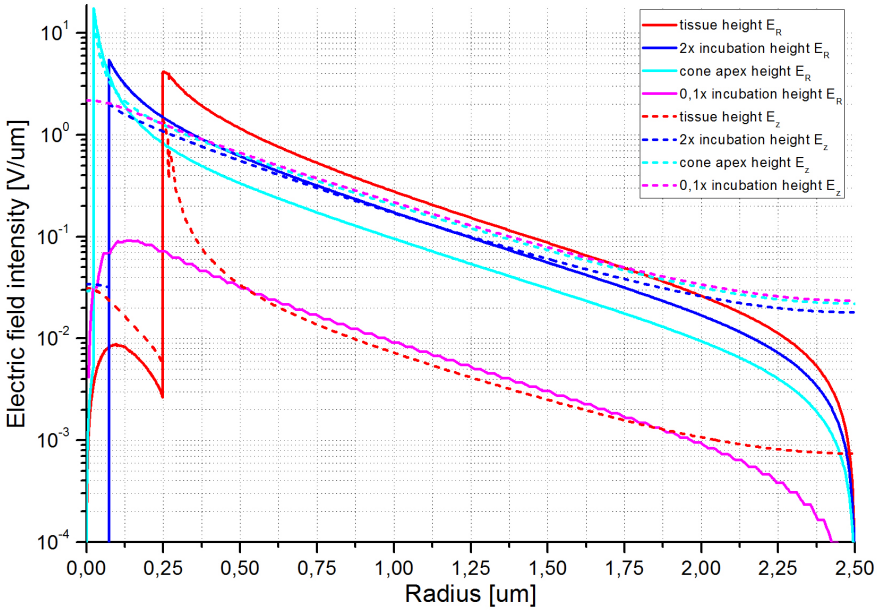

parameter, it is limiting factor ensuring finite volume for computer simulation. Semi-angles α, β decide grain's proportions, whereas cap radius and incubation height scale the grain size. The proportion is an inherent and stable property attained within the deposition of mixed phase layer. Incubation height and cap radius are feasible to vary within film deposition. Bellow, we will try to disclose effects of deposition parameters on AFM probe's current[10].

Resultant dependence of total current flowing through the bottom electrode on cap radius (Fig. 3.8) might be adequately delineated by linear function in range of $50-300\,nm$ with slope $k = (11.9\pm0.5)\,fA/nm$, intercept $q = (-350\pm90)\,fA$ and coefficient of determination $R^2 = 0.985$. Remaining conditions stayed the same as in table Tab. 2. The same qualitative dependence was observed experimentally (Fig. 4.5).

Naturally, it would be beneficial, if experimental data from chapter 4 were fitted with model curve. Comfortable adjusting of a-Si conductivity and amorphous tissue height would probably lead to overlapping of model curve with measured data in graph Fig. 4.5. Nevertheless, this procedure contradicts with scientific virtue due to various arguments. AFM measurements lack sufficient experimental reproducibility under ambient atmosphere conditions, particularly for aged specimens [Vetushka2010], [Vetushka-phd]. Experimental results are greatly dependent on used cantilever and on its abrasion, that master entire tunneling process. Therefore, received experimental data are strongly influenced with momentary specimen's surface quality and with the interface among film and cantilever tip.

[10]Henceforth, we simply say current.

Figure 3.6: *Terrain map of electrical potential above the cross section view.*

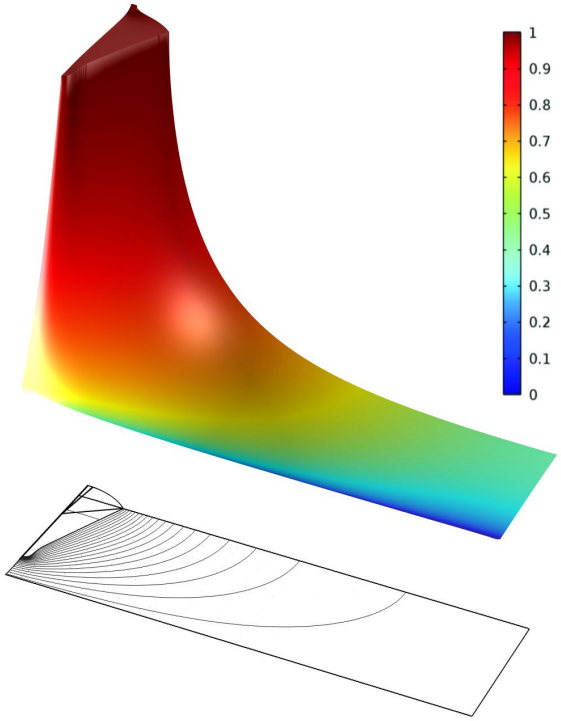

Convenient modification of material constant in order to obtain good agreement with experimental results, and subsequent elimination of negative AFM measurement effects, that numerical model does not involve, do not push our knowledge forward or make any step ahead in comprehension.

Now, we will focus on dependence of current upon incubation height plotted in Fig. 3.9. In this simulation cone's height is fixed at $0.7\,\mu m$ and incubation height is varied, whence amorphous tissue height is also varied, as a sum of incubation height and grain's cone. Sample bias voltage is standardly $1\,V$, model radius was $2\,\mu m$. Grain's cone hits the substrate (resp. electrode) for null incubation layer. When this happens, one might hope that current flew primarily through the only one point that cone apex contacts bottom electrode. But this is an incorrect idea, because through zero dimensional singular object[11] in 3 dimensional physical arrangement flows no current. Therefore, charge transport is realizable only through cone's skirt. Oppositely, if incubation height approaches infinity, electric resistance between both electrodes reaches infinity and current converges asymptotically to zero. For those reasons, it is possible to approximate function with a linear line only in limited interval. Slope of line is $k = (-2.08 \pm 0.09)$, intercept $q = (2.88 \pm 0.03)$ and $R^2 = 0.962$. This case has coherence with preceding example, where amorphous tissue height was constant and the cone's height was changed (through cap radius), but both situations are not mutually substitutable.

Trivial formula (3.12) for power loss in ohmic isotropic homogeneous material

[11] for instance throttled pipe into a single point

Figure 3.7: *Dependence of AFM probe's current on amorphous tissue conductivity.*

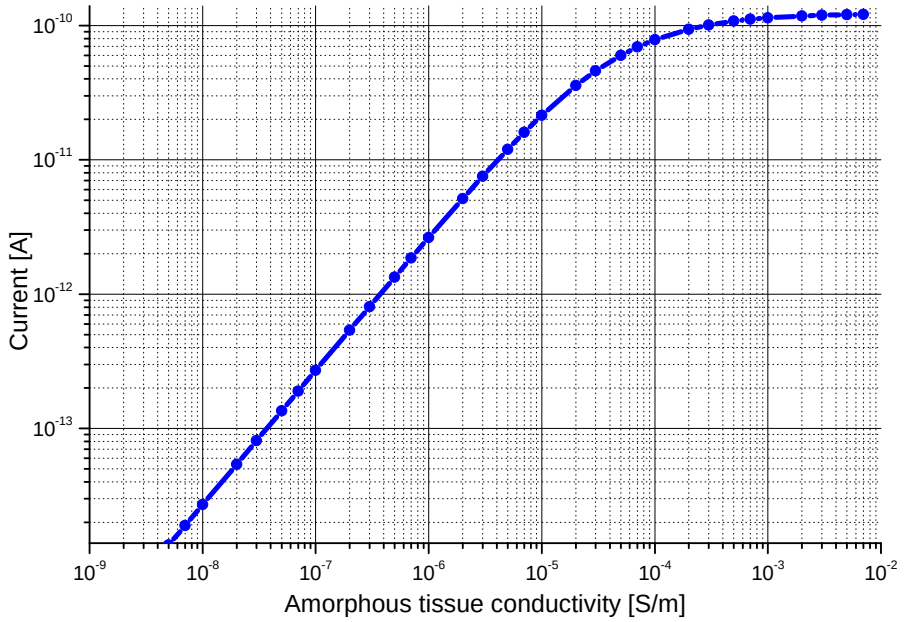

Figure 3.8: *Dependence of AFM probe's current on cap radius (from top view).*

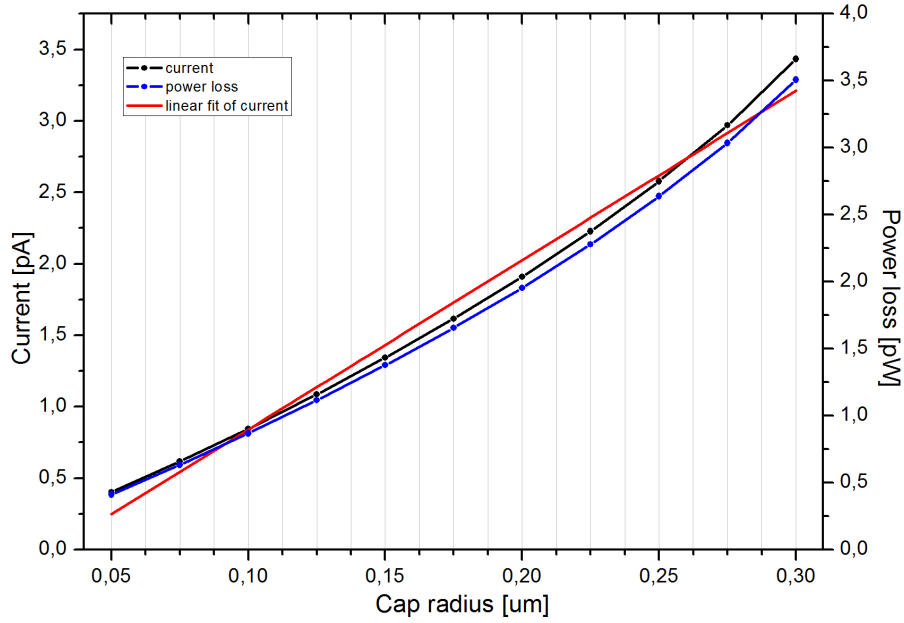

Figure 3.9: *Dependence of AFM probe's current on incubation layer height.*

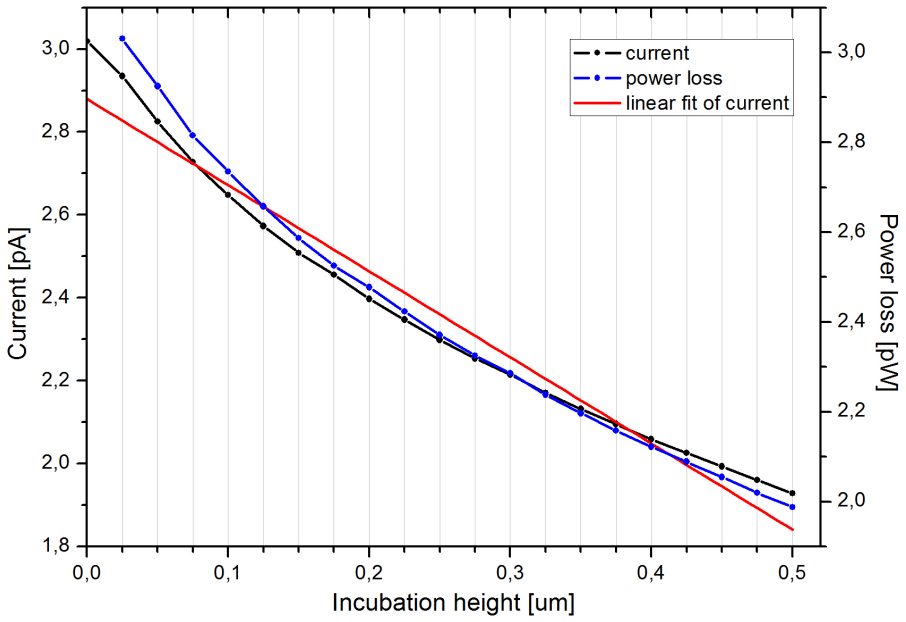

holds exactly for cylindrical conductor contacted at basements to voltage V. For voltage of $1\,V$, numerical value of lossy power is equalled to value of current (units of both quantities are omitted). For the case of grain geometry, this fact is retained valid with accuracy in the same order of magnitude. Discrepancy of dissipation curve and current curve gives us some clue about divergence of the current stream and indicates possible substitution of grain-tissue model for simple cylinder. Then the slope of IV curve and other current-like dependences will be multiplied by constant prefactor reflecting the geometrical conformation of grain-tissue model.

Previously, it was mentioned that the total power loss P is an integral of power loss density $p = \sigma E^2$ over entire model volume $P = \int \sigma E^2 \,\mathrm{d}^3 r$. Voltage is commonly defined as path integral from the first to the second electrode $V = \int \mathbf{E}(\mathbf{r}) \cdot \mathrm{d}\mathbf{r}$. Inward current is defined as an integral of input current density over area of the first electrode $I = \int \mathbf{j} \cdot \mathrm{d}\mathbf{S} = \int \sigma \mathbf{E} \cdot \mathrm{d}\mathbf{S}$. For a layer in the shape of cylinder, contacted at its basements, electric intensity $\mathbf{E}$ is constant. Hence, the power loss integral P is able to separate into the product of current I and voltage V. For nontrivial geometry, factorization is not applicable. Similarity between complex geometry and cylinder geometry decides, whether power loss P converges to product IV or not.

3.4 Effect of tip's deformation on the shape of contact zone

There are two basic qualitative positions of AFM cantilever's tip for electrical measurements:

1. the position where the tip contacts the cap's surface – cap contact
2. the position where tip touches plane surface of amorphous tissue – off-cap contact.

Cantilever's tip has its native spherical curvature at the end, which was created during the process of etching. Young modulus of cantilever's material is comparable to modulus of silicon microcrystalline grain or amorphous tissue. AFM deflection setpoint incites the piezo motor to press the scanning probe towards the surface. Applied force causes material deformation at tip-grain, resp. tip-tissue interface. Basically, it is a deformation of two elastic spheres, resp. a deformation of the elastic sphere with elastic plane (also known as Hertzian contact). Contact zone is a circle [Johnson]. Let us have two spheres of radii R_1, R_2 that are made of materials with Young moduli E_1, E_2 and Poisson ratios ν_1, ν_2. Let F be the interacting force. Denote E^* reduced mutual Young modulus

$$\frac{1}{E^*} = \frac{1-\nu_1^2}{E_1} + \frac{1-\nu_2^2}{E_2} \tag{3.14}$$

and define effective radius R as

$$\frac{1}{R} = \frac{1}{R_1} + \frac{1}{R_2}\,. \tag{3.15}$$

Penetration depth d of sphere with higher hardness into the second softer sphere is

$$d = \sqrt[3]{\left(\frac{3}{4}\right)^2 \frac{F^2}{E^{*2}R}}\,. \tag{3.16}$$

and circular contact zone has radius

$$a = \sqrt{dR} = \sqrt[3]{\frac{3}{4}\frac{FR^2}{E^*}}\,. \tag{3.17}$$

If one of the radii approaches infinity, then interface between sphere and half-space is received.

To obtain numerical evaluations of previous quantities, assume a silicon-silicon contact, tip's radius $R_1 = 30\,nm$, grain cap radius $R_2 = 0.33\,\mu m$, Poisson ratio $\nu = 0.28$, Young modulus $E = 130\,GPa$ (in direction [100]). Typical probe

contact force is about $10\,nN$. This yields effective radius $R = 28\,nm$ for sphere-sphere and $R = 30\,nm$ for sphere-halfspace contact. Further, reduced Young modulus is $E^* = 70.5\ GPa$. Penetration depth is for both cases almost the same $d \approx 0.072 - 0.074\,nm$. This size is far beyond validity of continuum mechanics. But resulting contact zone radius $a \approx 1.5\,nm$ is plausible. In accordance to Fig. 3.1, one acquires effective contact angle $\gamma = 0.3°$.

Trajectory, that AFM tip left after scanning of the μc-Si sample biased to oxidizing voltage $+10\,V$, is well demonstrated in paper [Vetushka2010] in Fig. 2. Tip created trace during scanning motion, due to local anodic oxidation. Width of trace $50\,nm$ is equalled to diameter of tip's contact zone. Tip curvature radius was roughly $10\,nm$. For cap sphere radius $0.33\,\mu m$ we gain experimental value of effective contact angle $\gamma \approx 4.3°$.

This does not truly fit with introduced concept of tip's mechanical deformation. Probably, effective contact area is predominantly determined by spatial dispersion of electron stream due tunneling effect from the probe's tip.

3.5 Dependence of current upon position and size of the cap-contact

Our further exertion will be aimed to investigate dependence of AFM probe's current on the area of contact spot, i.e. on contact zone radius a, resp. on contact angle γ. In addition, we will also focus on the effect of distance between the top of cap and the contact zone.

Firstly, inspect parametric sweep of effective angle γ in Fig. 3.11. For zero angle, when AFM tip contacts at the only one point, current quickly falls to naught. Oppositely, if effective angle tends to cap spherical sector semi-angle β, current is being saturated. Simulation was performed for bias voltage $1\,V$. Power loss curve is still above current curve without any intersects.

Secondly, position of cap contact onto cap spherical sector is represented with deviation angle δ, taken from the axis of symmetry (Fig. 3.10). Parametric sweep of current upon deviation angle δ was made for fixed effective contact angle $\gamma = 5°$. Range of angle deviation was from 0 to 45°. Problem is three-dimensional with mirror plain of symmetry. As documents graph in Fig. 3.12, no significant qualitative change of current was discovered. Electric charge still seeks the easiest path for its transfer, that leads throughout more conductive grain. This fact could not be seriously altered with deviation angle δ. Nevertheless, weak monotonous decreasing trend is appreciable. The angle of deviation reduces resistive distance between the cap contact and the bottom electrode. But the effect of contact asymmetry, that decrease current through the grain, faintly prevails. Deviation

Figure 3.10: *Model geometry explaining the terminology the contact onto the cap and onto the tissue. Angle δ denotes deviation of cap's contact from the axis of symmetry. Angle γ defines an effective contact area for cap contact. Similarly, zone distance determines space between the off-cap contact and axis. Zone radius defines the effective contact area for the off-cap contact.*

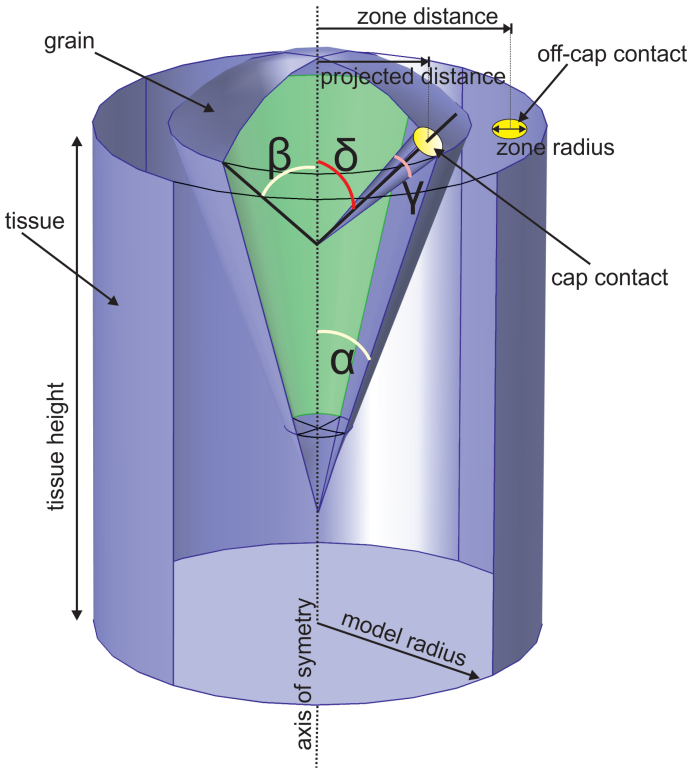

angle influences solution more qualitatively rather quantitatively.

Distribution of electric intensity and current density for asymmetric cap-contact arrangement is in Fig. 3.13.

3.6 Dependence of current upon position and size of the off-cap contact

The second tip's position is the contact onto amorphous tissue. At the beginning, parametric sweep of the effective contact radius would be studied at fixed distance from the central axis of symmetry. The distance was set up to $1.4\times$cap radius $= 0.357\mu m$. Relevant interval of radii that simulates different tip's curvature (sharpness) is from $5\,nm$ to $80\,nm$. Area of the contact zone defines amount of electric charge entering into a-Si:H tissue.

Conceive whole model as a conductive fiber, having two basements with insulating coat. Input basement is represented with effective contact zone and output basement with bottom electrode. What exactly happens with electric charge, as travels from input basement to output basement is unimportant or undetectable, excluding the fact of the input and output charge equality. If input basement has

Figure 3.11: *Dependence of current and total power loss on the effective contact angle γ.*

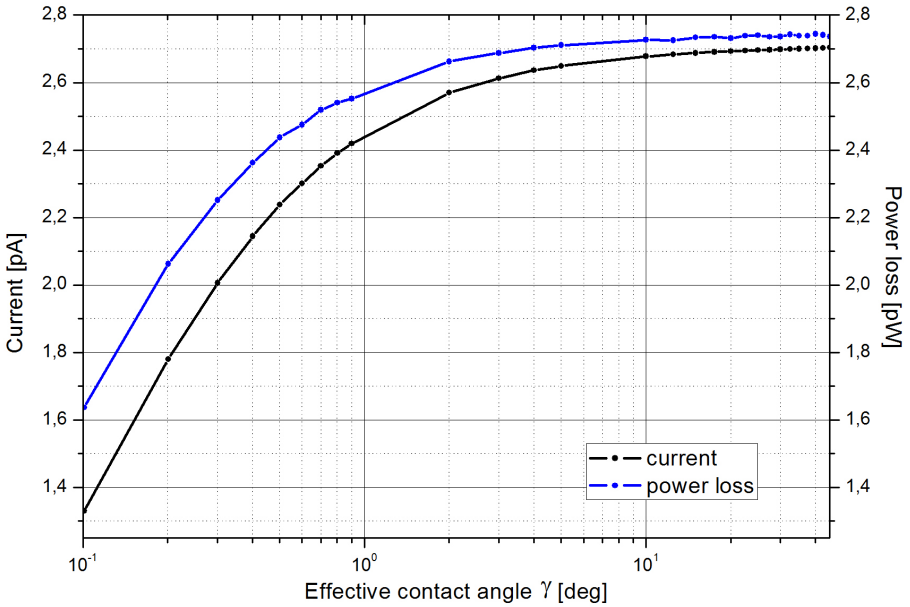

Figure 3.12: *Current and power loss dependence on various deviation angle δ.*

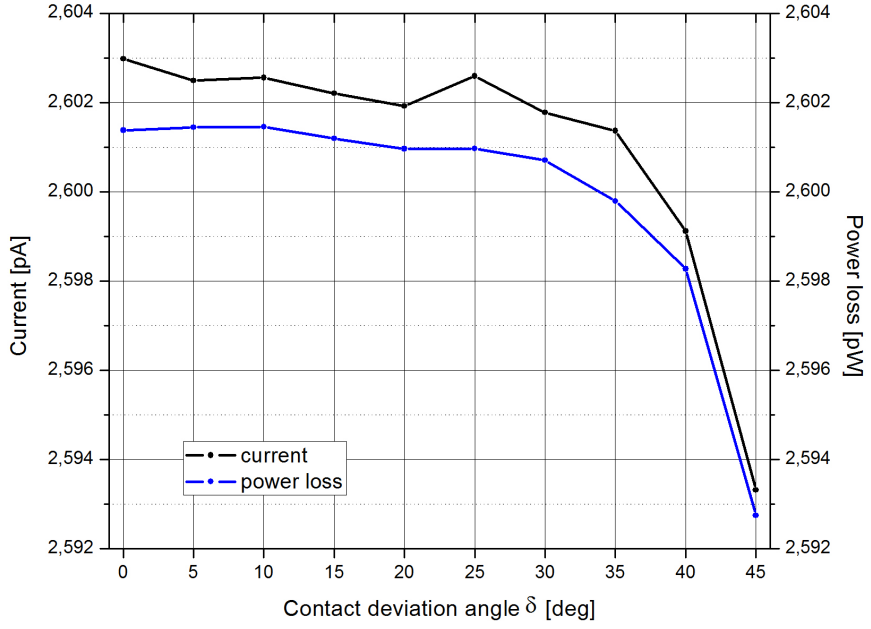

Figure 3.13: *Solution for electric intensity and current density from cross section view, resp. from top view at height of tissue. Arrows are scaled logarithmically. Effective contact angle γ is 5° and deviation angle δ is 45°.*

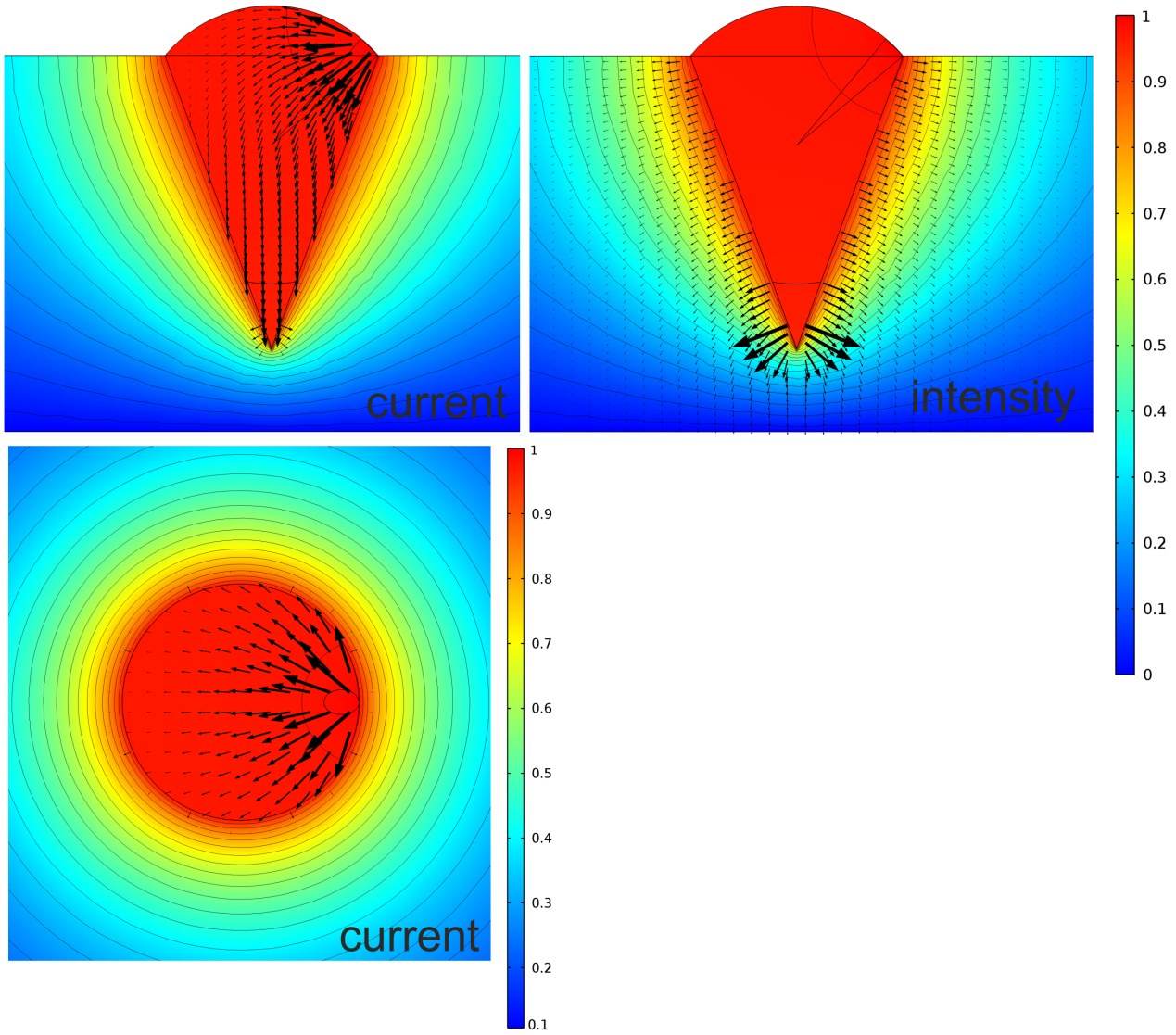

Figure 3.14: *Dependence of current and total power loss on contact zone radius (in tissue-contact geometry) at fixed distance* $1.4\times$*radius of cap from the axis of symmetry.*

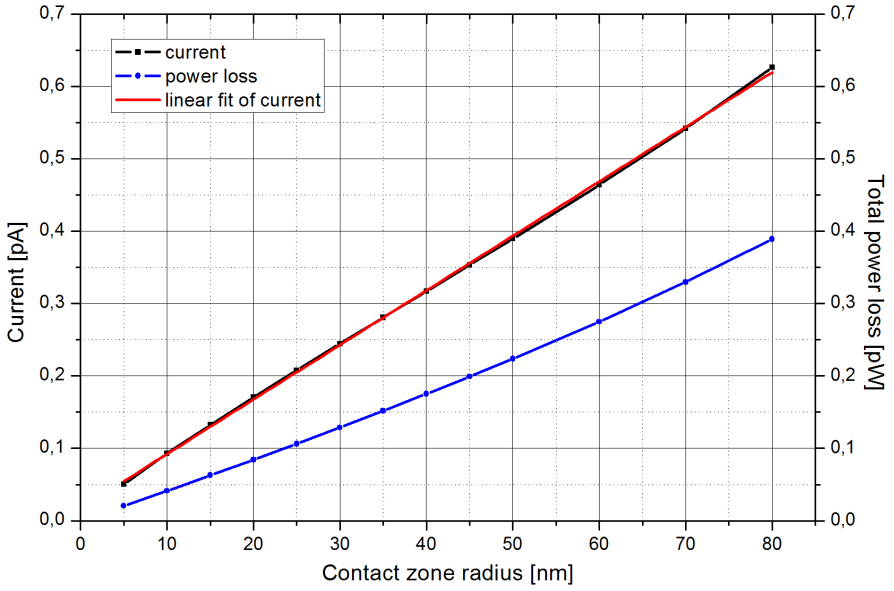

homogeneous inward current density across its entire area and if current density is perpendicular to the basement surface[12], then input and consequently also output current is proportional to the area of the input basement. This simple abstract idea is fairly well fulfilled, as Fig. 3.14 shows. Linear function fitting current curve has slope $k = (7.53 \pm 0.04)\, fA/nm$ and small intercept $q = (17 \pm 2)\, fA$, regression coefficient is $R^2 = 0.9996$. Power dissipation curve lies below current curve. The shift evokes subsequent suspicion. The off-cap contact shifts current curve above power dissipation curve, whereas in the case of cap-contact, current and dissipation curve almost overlays one the other.

In Fig. 3.15, dependence of current upon the contact zone distance from axis of symmetry is plotted. Contact area was fixed within the sweep and set to $29.01\, nm$. This value yields the same area, as we had for cap-contact with effective angle $\gamma = 5°$. As contact zone on tissue drifts apart from axis, the amount of current, that flows through the grain, is diminished. Current converges to value $0.18\, pA$ and lossy power tends to $0.1185\, pW$, as contact zone distance approaches to infinity. Electric potential more and more disregards presence of grain in contact zone's neighbourhood. The whole model situation ends up, as if no grain would ever exist and only if the contact zone and bottom electrode is left.

Plot Fig. 3.16 links up parametric sweep on deviation angle δ with parametric sweep on contact zone's distance on tissue. Position vector pointing from the axis to the contact zone located on cap's surface is projected to radius. Huge step

[12]The same assumption for output basement is not required.

Figure 3.15: *Current and power loss descent limiting to value* $0.18\,pA$, *respectively* $0.1185\,pW$, *as tip's contact zone on tissue moves further from axis of symmetry.*

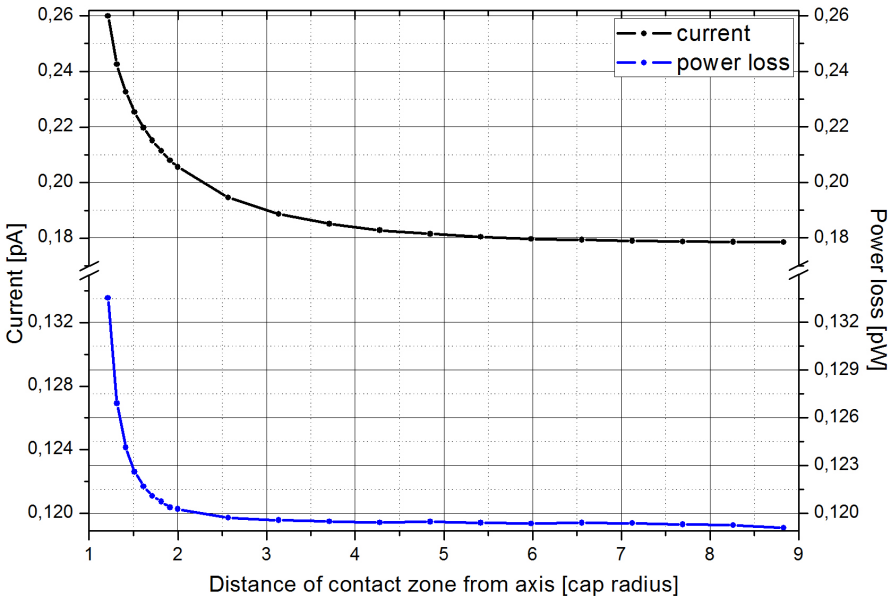

downwards at boundary of the cap strictly dominates final curve, as well as to the experimental curve in Fig. 4.1.

3.7 Agglomerates

Up to now, we have handled with a solitary grain enclosed with amorphous tissue. Forthcoming section will be devoted to the presence of additional secondary grain in our model. In order to understand electric behaviour of complicated grain's formation, a theory of 2 grain system must be developed. Particularly, two fundamental questions related to geometrical configuration should be answered. How separation distance $\mathcal{D}$ between both grains and how secondary grain's size influences charge flow through a primary contacted grain. Appropriate physical arrangement is sketched at picture Fig. 3.18. Axial symmetry is no longer favourable and thereby unemployed, mirror symmetry still holds. Instead of it, a block was adopted as a amorphous silicon tissue. The height of block is standardly $0.9\,\mu m$. Width is a sum of double model edge $1.8\,\mu m$ plus the cone's separation distance. Block's depth is also equalled to model edge, that is regarded as a characteristic model size. Upper electric contact is located at the top of the primary grain's cap and still represents AFM probe's tip. Bottom side of the block has the role of the ground electrode. Bias voltage is foresighted set to $1\,V$.

Figure 3.16: *Summary of graphs from Fig. 3.13, Fig. 3.15. Deviation angle δ was recalculated into the distance projected to radius. Note the discontinuity of current, as the grain boundary is being crossed. Areas of cap-contact and off-cap contact are identical $2\,645\,nm^2$. But cap-contact is a sphere sector, while the off-cap contact is a circle on the tissue. Horizontal axis is in units of cap's radii.*

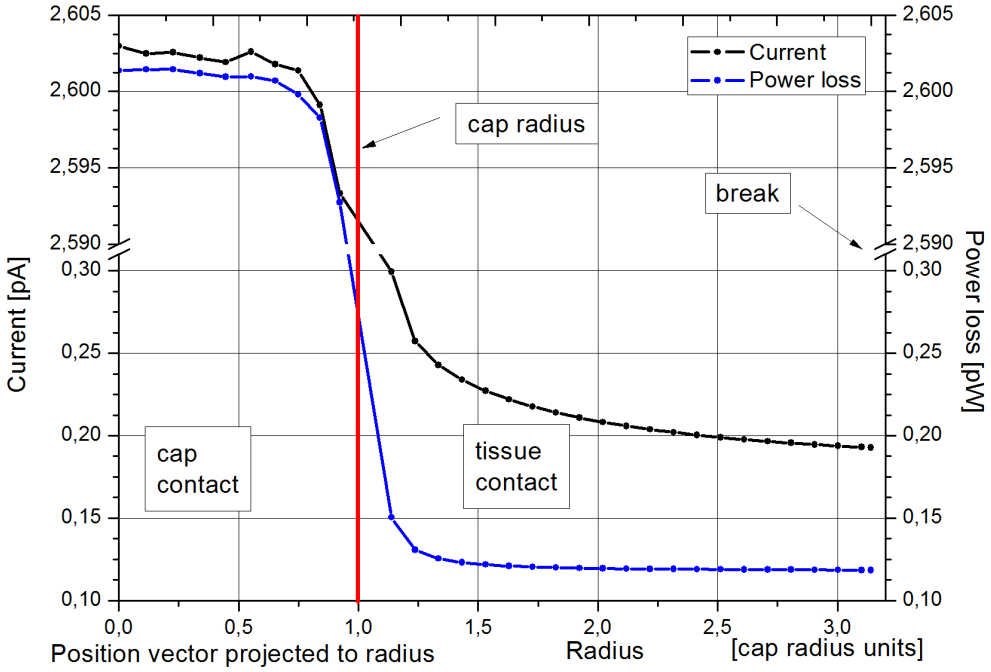

3.7.1 Variation of grain's separation distance

Firstly, effect of cone's separation distance $\mathcal{D}$ will be discussed. Qualitatively, two basic cone's position exists. If the distance between cones are less than the sum of cap's radii of both cones: $\mathcal{D} < r_{cap\,1} + r_{cap\,2}$, then each cone penetrates into the other one and shares common intersection[13] The second basic position describes situation, when separation distance is greater than the sum of cap's radii: $\mathcal{D} > r_{cap\,1} + r_{cap\,2}$, and cones are strictly isolated.

Solutions of both possible ordering are depicted in Fig. 3.19 and Fig. 3.20. Certain part of the total current flows throughout the secondary uncontacted grain and creates a competitive parallel electric channel in contrast to the primary grain. For joined grains, electrical potential is almost constant overall agglomerate's volume. In the case of detached grains, potential isosurfaces, generated by the primary grain, are asymmetrically deformed with an unfamiliar conductive body - secondary grain. Potential drop of the secondary grain is highly dependent upon the separation distance. The main current entrance into the isolated secondary grain is situated closely bellow the top side of the block, where the resistive amorphous filling is the most narrow (see the gray frame in Fig. 3.20).

Generally, surface boundary of a single cone consists of the spherical cap and

[13] $r_{cap\,1}$, $r_{cap\,2}$ denotes cap radius of the primary, resp. secondary cone.

Figure 3.17: *Illustrative distribution of electric intensity and current density from cross section view, resp. from top view at* $0.8\times$*height of tissue. Current density arrows are logarithmically scaled, field intensity arrows are proportional. Tissue is contacted at distance* $1.4\times$*cap radius. Colorful background and contours belongs to electric potential.*

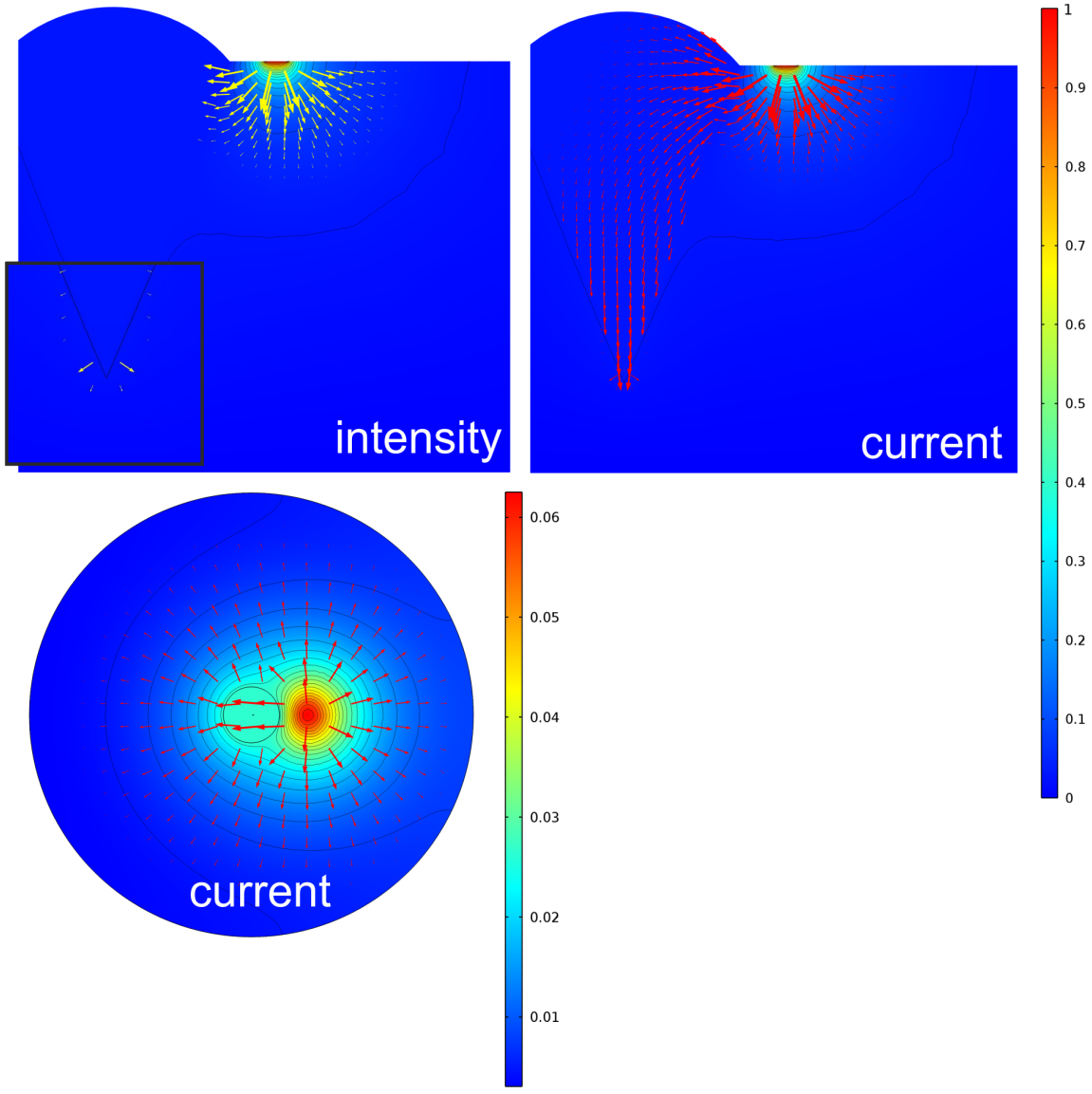

Figure 3.18: *Scheme of two-grain model. The grain with the top-cap contact is hereafter called the primary and the remaining uncontacted grain as the secondary. Conical surface of the cone is called the skirt. For attached grains, skirts are imperfect and damaged from the side of their mutual fusion.*

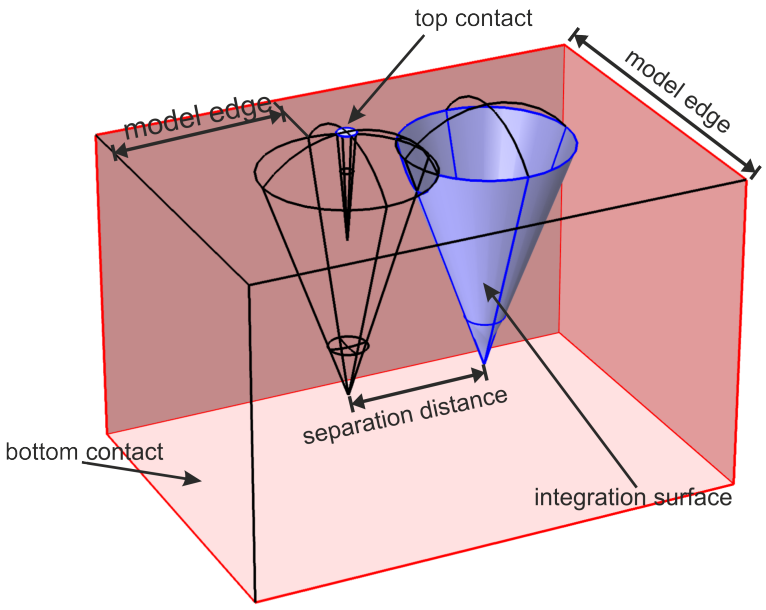

the conical skirt. Surface of the cone's cap is insulated except the upper contact zone of the primary grain. Thus, the only way for charge to transfer to the bottom electrode is via the cone's skirt. To obtain an information about current, that flows through the skirt, one needs to integrate spatial current density over its surface $\int_\Sigma \mathbf{j}\cdot\mathbf{n}\mathrm{d}S$. Normal vector $\mathbf{n}$ perpendicular to the skirt is given by expression (3.6). Theoretically, outward current from contacted cone equals to the total current over the bottom electrode. Also, an integral over the secondary cone's skirt should be identically null because no internal current source is presented. The uncontacted grain behaves as a passive element and continuity equation must be fulfilled. Hence, in the end, its outward current is the same as inward. Suggestively, lateral input into the secondary grain is compensated by output at the cone's apex. Intensity distribution in Fig. 3.20 shows a specific "silent" place, where dominant electric field, broadening from the primary grain, hits the secondary grain's field, that sparkles from the its cone's apex (see the frame).

We can easily recognize outward current as $\mathbf{j}\cdot\mathbf{n} > 0$. The condition allows us to calculate output current.

For linked cones, both skirts are slightly damaged and imperfect (see Fig. 3.18). In such case, integration runs over the damaged skirt and preceding consideration does not hold. Current across the secondary skirt is directly equalled to the decrease that the primary cone lost after fusion. Mutual proportion of contacted and uncontacted cone's current is plotted in Fig. 3.21. Size of the primary and secondary cone is the same. Region 1 is defined as geometrical arrangement when cones are combined. Oppositely, region 2 denotes situation of

isolated cones. In region 1, sum of primary and secondary cone's currents give total current over bottom electrode. In interval 0-1 of detachment distance, primary and secondary current are almost the same, from 1 to 2 currents split off and primary cone profits. As the divide into region 2 is crossed, primary current is identically attached to total current curve. The secondary current falls deeply to zero.

From pictures Fig. 3.19 and Fig. 3.20, one readily see that electric potential of grain does not change dramatically in volume of grains. Therefore, average value of electric potential in the grain is a meaningful quality. Dependence of average potential upon the separation length is in Fig. 3.22. Contrary, average value of potential in amorphous tissue is disputable. For various model edge, one apparently obtains different values of average tissue potential, although potential distribution overall the model system is identical, just because the tissue volume was changed. Generally and informally said, electric potential distribution creates a droplet enclosing the entire grain's cone (Fig. 3.13). In the rest of model bulk, potential is close to the zero. Thus, tissue average potential can be estimated as a weighted mean of primary and secondary droplets with addition of almost null potential bulk. Intersection of tissue potential and secondary grain potential curve might be interpreted as a beginning of far field.

3.7.2 Modification of the secondary grain's size

Now, we will survey the interplay between two grains in dependence upon the secondary grain's size for fixed grain's remoteness. Secondary grain size can be naturally measured in scale factor Θ respecting the size of the primary grain. For instance, the scale factor $\Theta = 3$ means that the secondary grain is three times larger than the primary one. Other geometrical parameters scale proportionally with the factor Θ. In the sequent text, we have equivalently chosen to describe the secondary grain's size by the cap radius parameter, expressed in units of primary grain cap's radius. But the reader can imagine the cap radius without units and obtains scale factor Θ.

If the secondary cone's center of mass is located inside the primary grain, magnification or reduction of secondary grain's size could not lead topologically to the arrangement of two separated cones. On the other hand, when secondary cone's mass center is set externally in relation to the primary cone, whole agglomerate undergoes a fission into two grains at the specific secondary cone's splitting size. Therefore, the choice of constant cone's separation distance is not arbitrary. The preceding consideration forces us to divide the problem in two cases. In our calculations, we have decided to set the secondary cone's center at circumference of the primary cap $\mathcal{D} = r_{cap\,1}$ and also at the distance of two primary cap radii, i.e.

$\mathcal{D} = 2\,r_{cap\,1}$. A common triplet of electric quantities - current, average potential, power loss will be studied. Size of the secondary cone is limited, because the secondary cap must not overlay electric contact of the primary grain. Accordingly, the factor Θ is restricted to interval 0.1-1.05 for $\mathcal{D} = r_{cap\,1}$, respectively 0.1-1.25 for $\mathcal{D} = 2\,r_{cap\,1}$.

Fig. 3.23 demonstrates averages potential of grains and tissue for fixed separation distance $\mathcal{D} = 2\,r_{cap\,1}$. Cone's separation only slightly decreases average potential of the primary grain from $0.98\,V$ to $0.96\,V$. But the mean potential of the secondary grain differs significantly. In region 1, potential saturates at $0.94\,V$. But after cones separation, it drops to value $0.45\,V$. Such value surprisingly corresponds to potential contour of the single grain model positioned at radius $2\,r_{cap\,1}$ and at the height of tissue.

Current is analyzed in Fig. 3.24. Before cone's conjunction, current through the secondary skirt is negligible small in comparison to total current. After link, conductive channel is created thru the second grain. The secondary current outperforms the primary current for size $\Theta = 1.125$. As the second grain is magnified, the participation of the primary cone declines. Total power dissipation of system and power loss of cones are plotted in Fig. 3.25. Resistive losses of the primary cone increase when secondary cone is extended. From the first view, it could be in contradiction with the reduction of the primary current. But in the contacted cone, chief power dissipation takes place in the cap, in neighbourhoods of the contact zone (see frame in Fig. 3.3). Charge flux, through the domain of the contacted cap[14], does not dramatically depends on the mutual interaction of primary and secondary current, but depends upon their sum.

Only a short remark will be devoted to Fig. 3.26. Graph shows comparison of total current across the bottom electrode with currents across primary and secondary damaged cone's skirts. The size sweep was carried out for separation distance $\mathcal{D} = 1 \times R_{cap\,1}$. The sum of cone's current gives the total current. At point $R_{cap\,2} := R_{cap\,1}$, structure of cones is symmetrical, excluding the position of upper electric contact, and both cone's current are the same.

[14] We mean the primary cap, not the primary cone.

Figure 3.19: *Distribution of electric field intensity and spatial current density for the case of linked grains of the same size. Arrows are logarithmically scaled. Last picture is the cross section (top view) at* $0.97\times$*tissue height.*

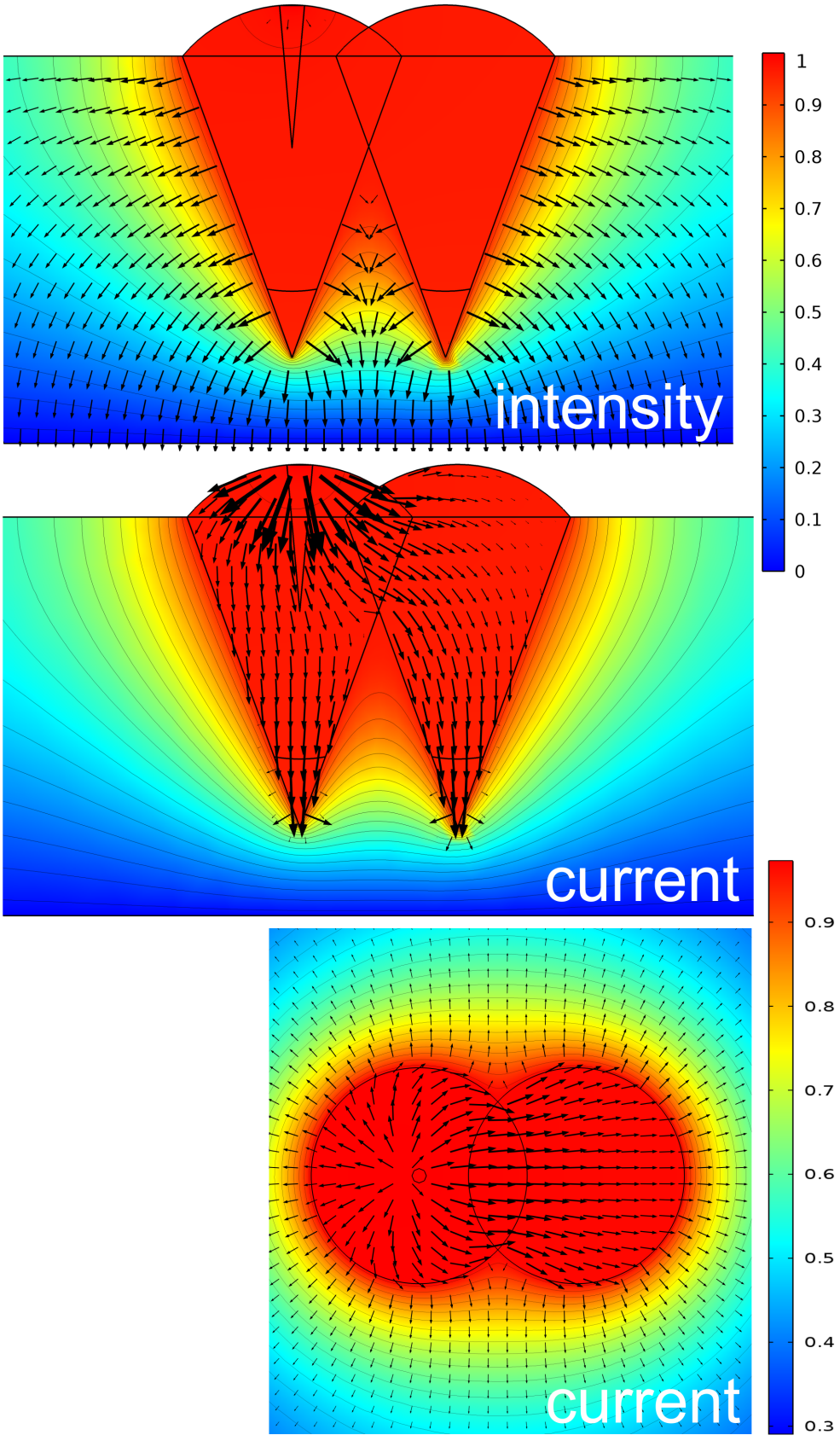

Figure 3.20: *Solution of electric field and current density for separated grain arrangement. Arrows are logarithmically scaled. Last picture is the cross section (top view) at* $0.97\times$*tissue height. The frame in intensity map demonstrates existence of the silent place. The frame in current map presents competitive channel in relation to the main electric current lead throughout the primary grain.*

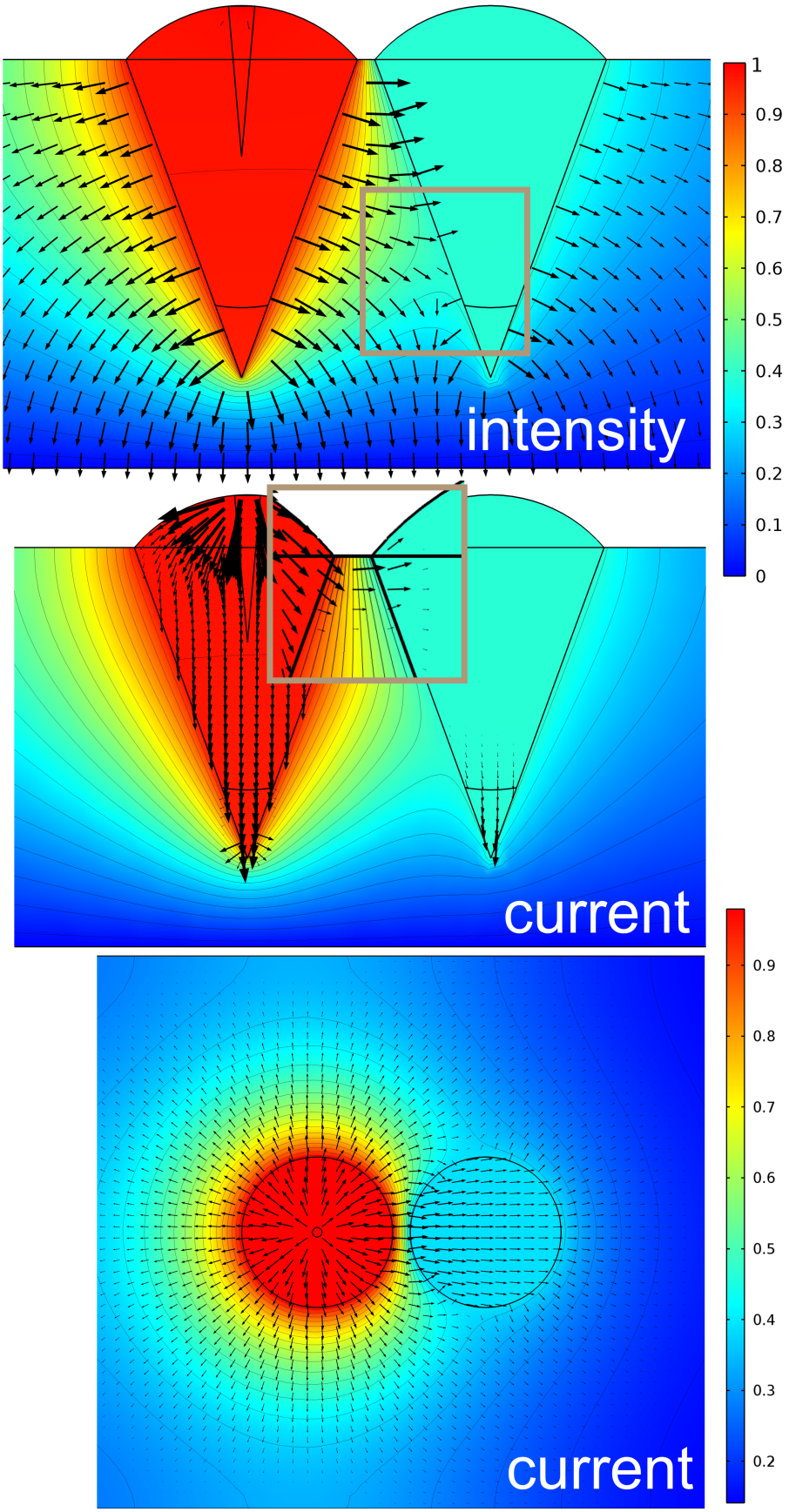

Figure 3.21: *Current as a function of mutual cone's separation distance. Horizontal axis is in units of cap radius* (0.255 μm). *Current axis is logarithmic above the break. Magent vertical line segment identify termination of grain's mutual intersection. Total current means entire charge flow across bottom electrode. Uncontacted cone's current is obtained as an integration across deformed skirt in region 1. In region 2, integration runs over ideal skirt but integrand is only outward (positive) flux. In region 1, contacted cone's current was received in the same manner as uncontacted cone's current. In region 2, contacted cone's current is the difference between total current and uncontacted cone's current.*

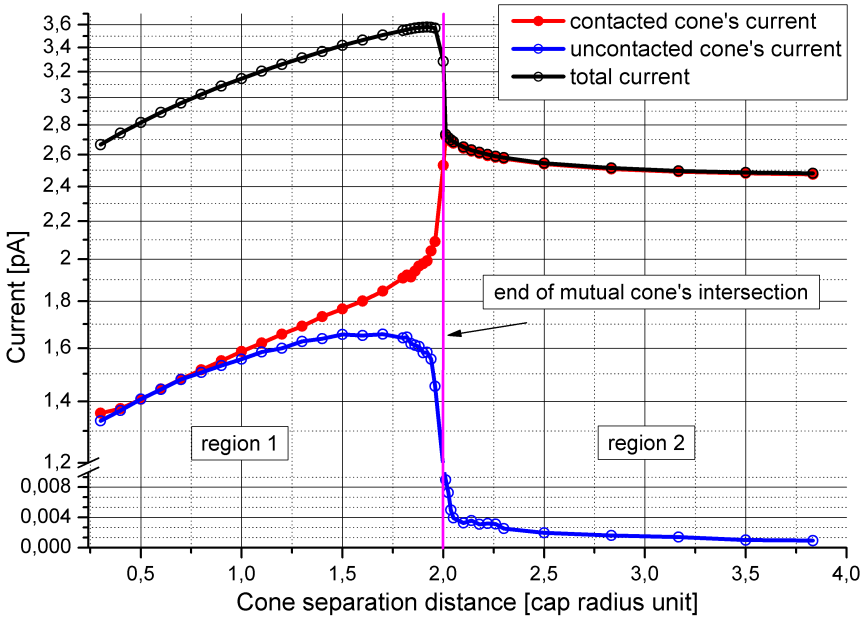

Figure 3.22: *Average electrical potential over primary contacted cone, secondary uncontacted cone and tissue in dependence on cone's separation distance. Distance is in units of cap radius. Radii of primary and secondary cones are equalled therefore the end of mutual cone's intersection is positioned at 2.*

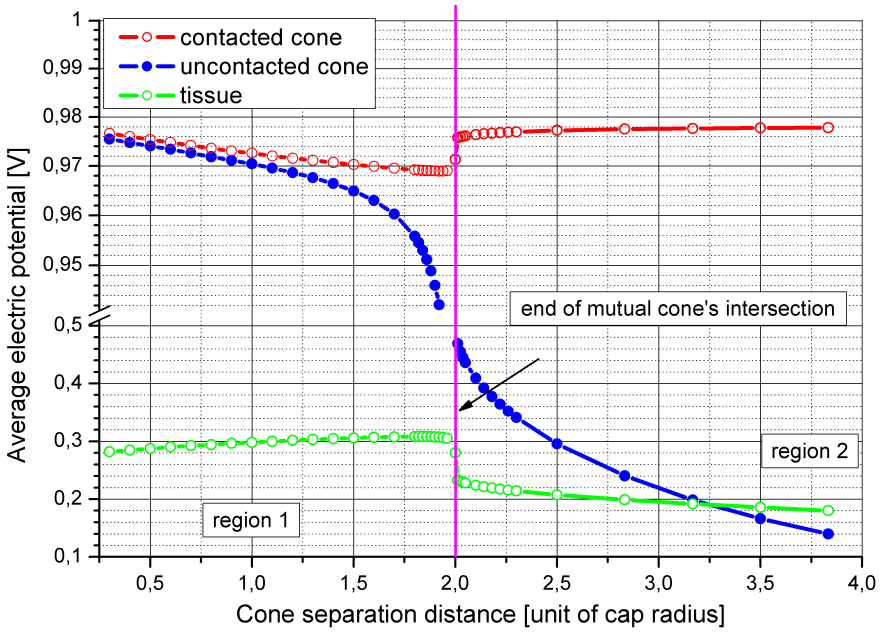

Figure 3.23: *Average electric potential for the sweep of secondary cone's size. Fixed separation distance was set to* $\mathcal{D} = 2 \times r_{cap\,1}$. *Region 1 expresses the fact that cones are fused. Situation, when cones are isolated, defines region 2. Magent line marks the size of the secondary grain, when cone's merger begins. At this point, both cones have the same size.*

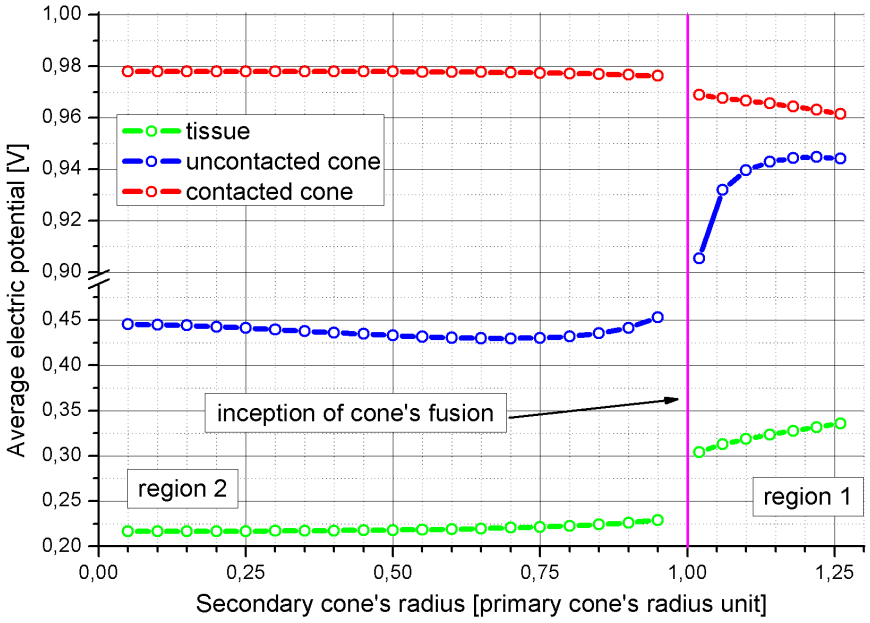

Figure 3.24: *Dependence of current on the size of the secondary cone for fixed separation distance* $\mathcal{D} = 2 \times r_{cap\,1}$. *The meaning of currents is the same as in Fig. 3.21.*

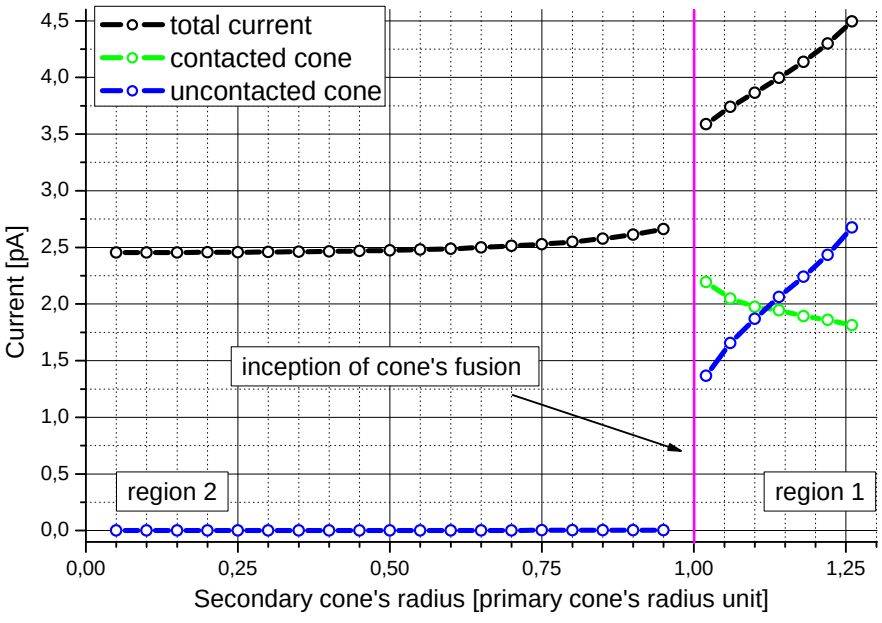

Figure 3.25: *Power resistive loss in cones as a function of secondary grain's size. Fixed separation distance was set to* $\mathcal{D} = 2\times r_{cap\,1}$. *Power loss of the whole system is* 10-50$\times$ *greater than in the primary cone.*

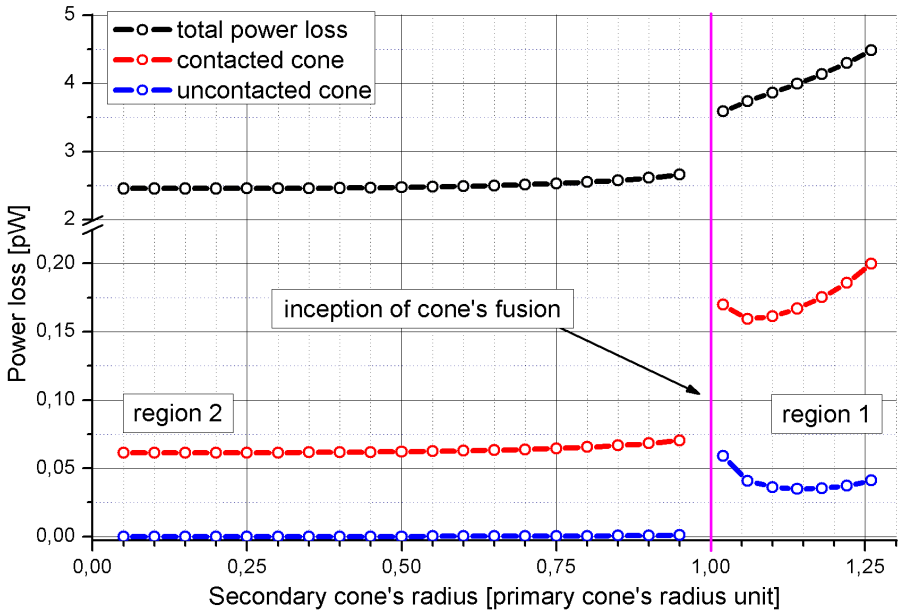

Figure 3.26: *Dependence of current upon size of the secondary cone for fixed separation distance* $\mathcal{D} = r_{cap\,1}$. *Size of the secondary cone, equalled to 1, corresponds to situation, when both cones have the same greatness. In such case, geometrical arrangement is symmetrical and currents are almost identical, although only the primary grain is contacted.*

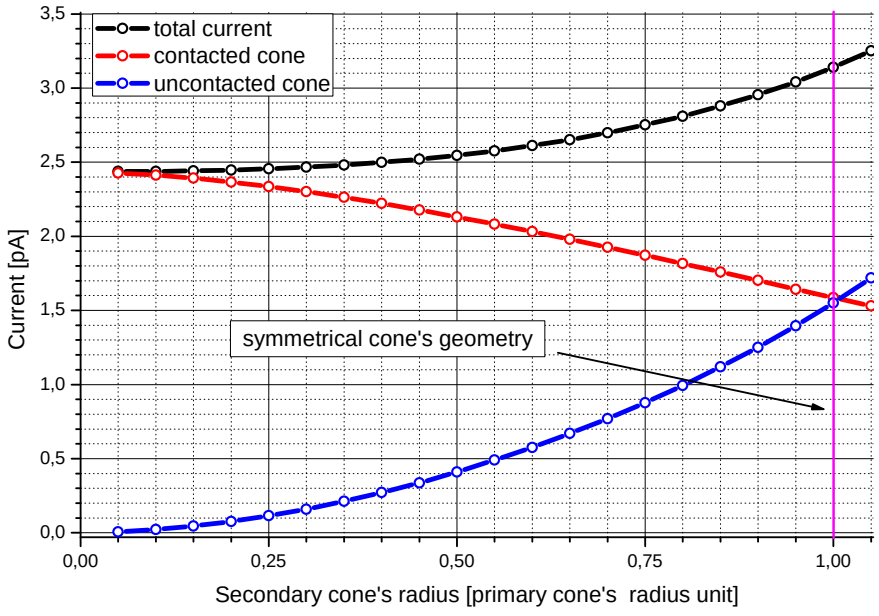

4. Local electrical properties of hydrogenated microcrystalline and amorphous mixed silicon films

As a matter of fact, there is only one broadly used technique to seriously inspect local electrical properties of thin films at micro- and nano-scale. It is the scanning probe microscopy, especially atomic force microscopy. Conductive mode of AFM works similarly as a tiny ampere-meter measuring in scales of fA, pA, nA. Schematic diagram of the AFM in conductive mode is shown in Fig. 2.3. Main advantage of AFM experimental device is ability to point whatever place at the film surface and measure volt-ampere characteristics (IV curve). AFM also allows to obtain topographical and current map of the surface.

Thus, there are two kinds of output from AFM measurement that give us some information about electric properties: IV curve and current map[1]. Let us realize what kind of current (or charge flow) AFM cantilever's tip actually detects. In the case of IV curve, the tip contacts the surface at area approximately from 30 to $220\,nm^2$ according to the tip's curvature radius. Then bias voltage is applied between the specimen's electrode and the tip[2]. AFM current amplifier detects current flowing through a small contact area at specific point with given coordinates. Hence, measurement is very local. Contact tip area is typically negligible in comparison to the area of the cap, therefore the tip contact is well approximated as a point contact. Thus, one might say that AFM current amplifier detects total current flowing through a point contact[3].

Whereas the physical substance of AFM current map can be explained differently. Assume a region of size $10 \times 10\,\mu m^2$. AFM cantilever scans line per line, until the desired number of rows is reached, e.g. 256. Within the scanning of the single row, AFM tip stops at required number of points, e.g. 256. Coordinates of each point are registered and tunneling current is measured at that place. After completion of scanning, a matrix 256×256 is recorded and projected to original region. So, one pixel of map corresponds to area $A = 39 \times 39\,nm^2 \approx 1\,520\,nm^2$.

[1] AFM is usually equipped with other advanced features that enable to measure surface potential, magnetic properties, etc.

[2] Incidentally, suppose following convention for further reading: we say that the sample bias voltage is *positive, forward*; if the AFM probe is at higher electric potential level then specimen's electrode. Electron flows from the sample surface to the cantilever's tip. Conventional current is also positive and flows from the tip to the sample.

[3] In the section 3.4, we got to know that the term "point of contact" is not absolutely accurate expression for the interface between the tip and surface, because contact area still exist as a consequence of finite Young modules, even if it is very small. Nevertheless, suppose for a moment that tip touches the film only through a single point.

One value of current, measured in the center of square A, represents current over the square[4]. Area of square A has actually nothing in common with tip's contact area. From this point of view, measurement must be understand as nonlocal.

However, current map is naturally perceived as a continuous distribution of current density flowing through the layer's surface. One should be aware to avoid confusion with the situation, when the film is continuously covered with the plane contact biased to constant voltage.

Pixel of the current map is interchangeable with a point of IV curve, only if the area of the square A is the same as the tip's contact area.

Disadvantage of the AFM scanning technique is difficulty with interpretation of obtained data. Data are often affected with artefacts of the tip or with transient effects of thin insulating Si oxide layer.

A substitute circuit diagram for C-AFM probe operating in ambient can be described by six serial connected resistors: resistance of cantilever and tip R_{tip}, resistance of contact $R_{contact}$, resistance of interface between oxide layer and tip $R_{interface}$, resistance of a thin oxide layer R_{oxide}, resistance of the film mass R_{film} and resistance of electrode $R_{electrode}$.

Then total resistance is

$$R_{tot} = R_{tip} + R_{contact} + R_{interface} + R_{oxide} + R_{film} + R_{electrode}\,. \qquad (4.1)$$

$R_{contact}$ expresses geometrical conformation, i.e. how tip touches upper objects on the film's surface. For instance, if the tip is blunted or if the metal coating is worn, then the contact resistor is large. Oppositely, if tip touches the grain laterally, the contact area is greater and $R_{contact}$ is smaller. $R_{interface}$ stands for the set of things such as moisture, water meniscus enclosing the tip, dirt, tunneling effects, surface oxidation and other hardly identifiable and variable effects. R_{tip} and $R_{electrode}$ are usually in comparison to the rest of resistors negligible small.

4.1 Current profiles of grain

Firstly, we will study morphological effects of the grain's shape on the local behaviour of the electric current.

Initial step for such task is to investigate current change over the spherical cap. Because of axial symmetry of the cap, it is sufficient to describe dependence of current on radius[5]. In Fig. 4.1, several semi-profiles are plotted. Profiles were extracted from current map of the grain. Offsets of profiles were adjusted,

[4]Even if, this is not an average value, rather arbitrary, but taken at specific point.

[5]lateral distance taken from the interception of the axes of symmetry with surface plane of the film.

Figure 4.1: *Several current profiles (cross sections in current map) along the cap. The main trend is step function with skip at the boundary. Amorphous tissue is low conductive in contrast to μc-Si grain. Measurement carried out by Bruker Dimension Icon AFM.*

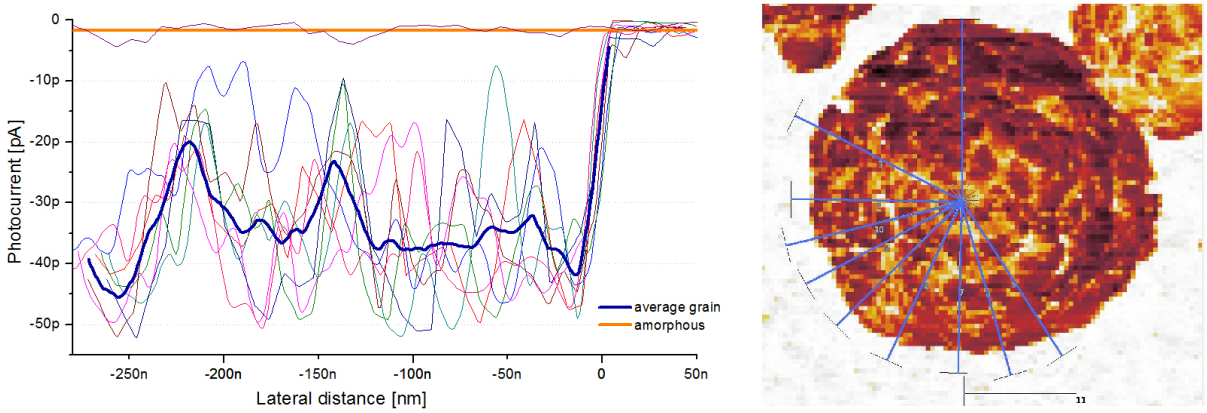

therefore boundaries of all profiles have the same lateral distance equalled to zero and lie at the same point. The reason of such act is that current profile is strongly contingent on the boundary divide more than on the axial asymmetry of the grain. The AFM image was scanned with diamond cantilever under illumination of AFM detection laser diode and under bias voltage of $-3V$ and vertical deflection setpoint[6] $0.3\,V$. Main trend of profiles is the step function with a skip at the boundary divide. Fluctuations of current on grain's surface, resp. roughness in current map, is caused by grain's inhomogeneities. Interior of the grain reminds fractal cauliflower structure. But the mean current profile is constant function on that cap. Seldom, there might be tendency to decrease absolute value of current, as tip approaches to the top of the cap. Because tip simply touches the surface at larger contact area at grain boundaries. At the top of the cap, tip contact is relatively modest, particularly when the tip's conductive coating is worn. Hence, if the tip arrives to the cap or when the tip leaves the cap, higher current should flow. For comparison, low steady conductivity of amorphous tissue is also demonstrated.

Graph in Fig. 4.3 displays current distribution over cap's profile. The length of the line-segment is $500\,nm$. One half of profile is onto the cap and the second one is onto the amorphous tissue. Gaussian peak nearby zero corresponds to nonconductive amorphous phase, whereas more or less uniformly distributed band from 20 to $70\,pA$ belongs to μc-Si grain.

Typical values of AFM tunneling current of $1\,\mu m$ thin silicon layer are $100-500\,pA$ for illuminated μc-Si:H, $1-10\,pA$ for illuminated a-Si:H under biased voltage $-2\,V$ (in dependence upon cantilever's type, thickness of oxide layer,

[6]Further in text only setpoint, in units of AFM quadrant photodector.

Figure 4.2: *Terrain of film surface. Colorful layout represents current distribution. Notice that agglomerates are more conductive than smaller isolated grains. Current inhomogeneities on cap surface are apparent. Scales are in pA.*

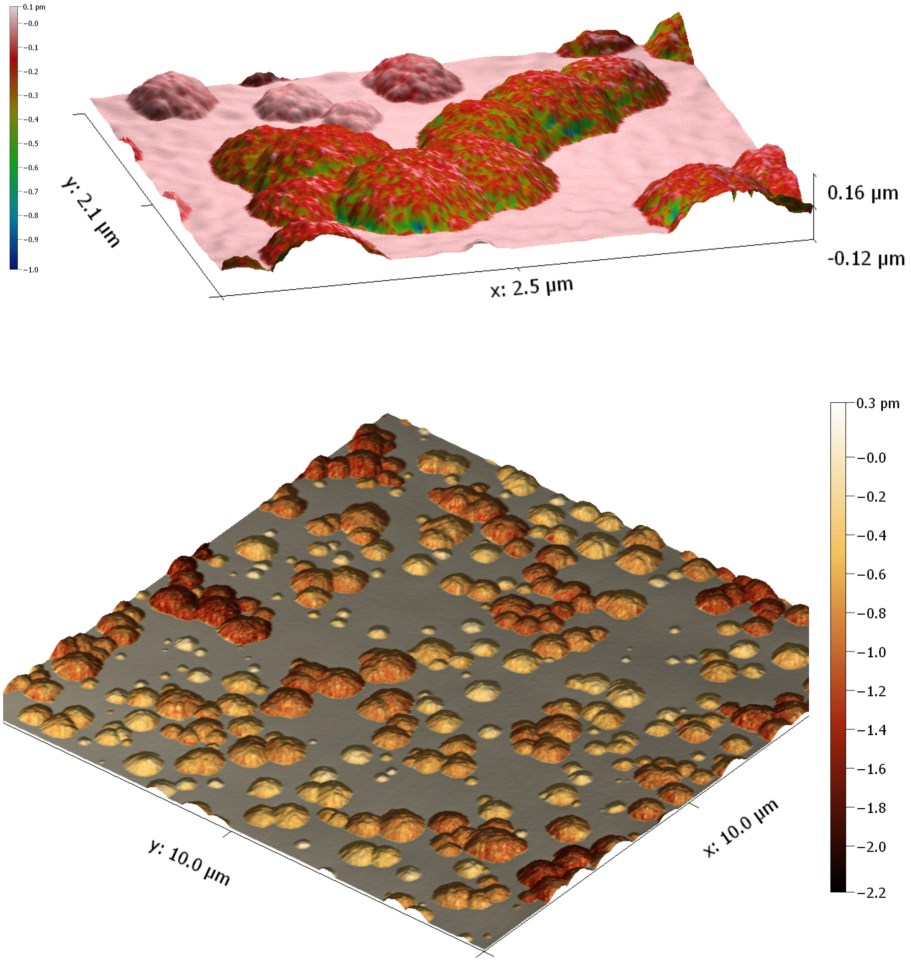

Figure 4.3: *Histogram of the current profile. Bin size* $0.8\,pA$*, total number of values 1000. Sharp peak shows minimal current in amorphous tissue, spread band belongs to fluctuations on grain's cap. Inset presents current as a function of distance in direction from the the center of the cap.*

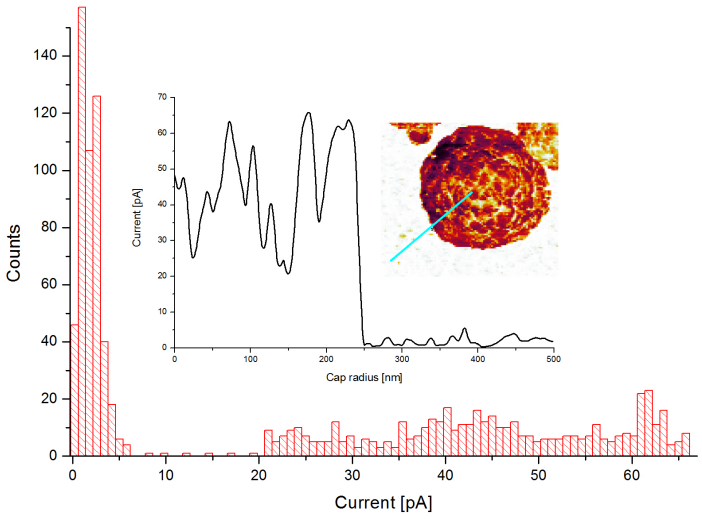

etc.). Without any illumination, it is usually 100 times less, so in orders of fA [7].

4.2 Dependence of current on cap radius

Now, we know that in the first approximation cap's surface has homogeneous and isotropic current density distribution (or equivalently constant conductivity). With image processing software, one can find rough average value across the surface of the cap balancing local inhomogeneities. Consequently, the following question is plausible: Is average current on grain dependent upon radius of the grain's cap?

In Fig. 4.4, we see the result $5 \times 5\,\mu m$ image taken by NT-MDT AFM under bias voltage $-2\,V$ and setpoint $1\,V$ and with standard silicon metal coated cantilever. We have measured average current over selected grains in inset of Fig. 4.4. These values are display in the chart and fitted with a linear function. Slope of the line is $k_1 = (0.03 \pm 0.08)\,fA/nm$ and intercept $q_1 = (320 \pm 20)\,fA$, coefficient of determination $R^2 = 0.013$. Average current on amorphous tissue is $(130 \pm 10)\,pA$.

The same thing was carried out for $5 \times 5\,\mu m$ image taken by Bruker Dimension Icon AFM under bias voltage $-1\,V$ and setpoint $0.3\,V$ with diamond cantilever (see Fig. 4.5). On current map, it is possible to see less conductive smaller grains. This observation proves linear fit with the slope $k_2 = (0.61 \pm 0.08)\,fA/nm$ and intercept $q_2 = (-11 \pm 7)\,fA$, coefficient of determination is $R^2 = 0.76$. The fact, that smaller grains are less conductive than larger, is also well demonstrated in Fig. 4.2. Compactness of agglomerates rapidly enlarges conductivity. Average amorphous current is $(1.8 \pm 1.3)\,pA$.

It it effortless to basically estimate value of current in a-Si:H tissue biased to units of volts. Conductivity of a-Si:H is approximately $\sigma_{photo} = 10^{-6}$-$10^{-5}\,S/cm$, thickness of the film is about $d = 2\,\mu m$ and effective contact area for tip with curvature radius $30-40\,nm$ is around $S = 2000\,nm^2$ [Vetushka2010]. Then Ohm's law gives resistance of film $R = 10^{12}$ - $10^{13}\,\Omega$. For sample bias voltage $1\,V$, one acquires current 100-1000 fA, which is in accordance with our observations.

Immediately, subsequent consideration is suggested. Photoconductivity of μc-Si is about two orders of magnitude greater than a-Si photoconductivity [Ledinsky2011], [Ledinsky2012]. The grain takes from 1 to 2 thirds of the film thickness. Therefore, microcrystalline portion on overall resistance can be omitted in comparison to the resistance of amorphous portion. Thus, remaining amorphous part produces one-third of resistance of the pure tissue. So, we anticipate from 1.5 to 3 times larger current on the grain than in amorphous environment.

[7] $1fA$ current is a stream of 3000 electrons/s.

Figure 4.4: *Dependence of average cap current on cap radius. NT-MDT AFM image.*

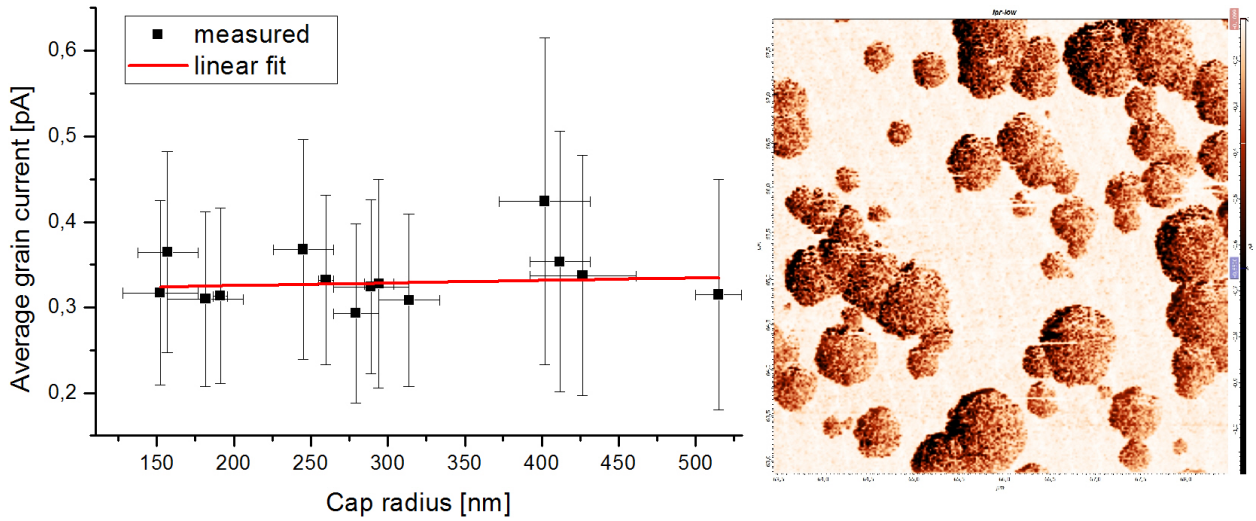

Figure 4.5: *Dependence of average cap current on cap radius. Bruker Dimension Icon AFM image. Identification number of sample: KSTM9.*

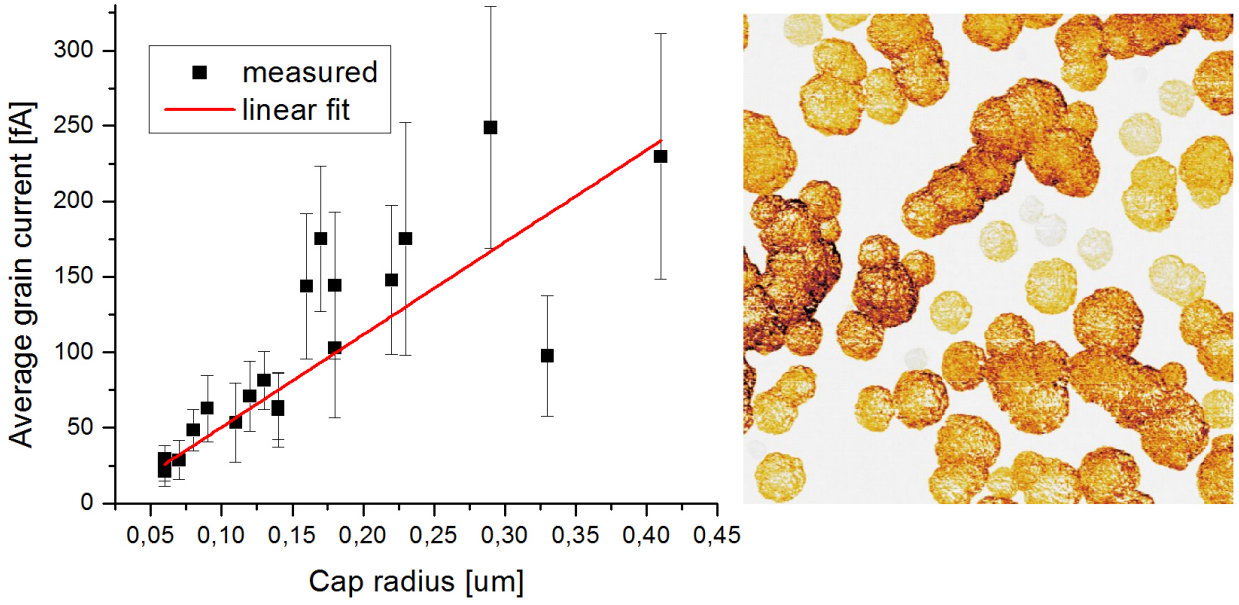

Further discussion modifying simple Ohm's law can be developed. Suppose that the electric resistance at the grain's site is directly proportional to the incubation layer v_i and indirectly to amorphous conductivity σ_a :

$$R \approx \widetilde{C}\frac{v_i}{\sigma_a}\,, \tag{4.2}$$

where $\widetilde{C}$ is a specific constant. Now, we will recall back simplified model of grain from Fig. 2.16. If we accept the terminology, where d denotes film thickness, r_{cap} is the cap radius, α is the apex angle, then the incubation height can be written as $v_i = d - r_{cap}/\tan\alpha$. Replacing v_i in (4.2) leads to formula

$$R = \frac{\widetilde{C}}{\sigma_a}(d - \frac{r_{cap}}{\tan\alpha}) = C_1 + C_2 r_{cap}\,, \tag{4.3}$$

where new constants C_1, C_2 were established. When r_{cap} approaches to the zero, resistance is reduced to $R = C_1$. Similarly, if grain reaches its maximum possible cap radius $r_{max} = d\tan\alpha$, i.e. if there is no incubation layer left, then $R = 0$. Of course that the grain's resistance does not equals zero, but in contrast to the resistance of amorphous portion, it actually does. These conditions give relation between constants: $dC_2\tan\alpha = C_1$. Under bias voltage V, one easily finds

$$I(r_{cap}) = \frac{V}{C_1(1 - \frac{r_{cap}}{r_{max}})}\,. \tag{4.4}$$

4.3 Coincidence of dark and photo current

Silicon is greatly sensitive to visible light due to band gap $1.1\,eV$ for crystalline phase and $1.7\,eV$ for amorphous phase. Under illumination, concentration of charge carriers is rapidly influenced by generation term on right hand side of equation (1.30). The specific form of generation term depends on layer's geometry. In the case of flat film without any interference reflections, generation term is expressed by (1.22), as was derived in chapter 1. For more complicated film's structure, distribution of light absorption can not be described with Beer-Lambert law, because it does not respect geometrical proportions of structure. Light power dissipation must be calculated via electro-magnetic energy density

$$w = \frac{1}{2}\varepsilon E^2 + \frac{1}{2}\frac{B^2}{\mu}\,. \tag{4.5}$$

where E, B are norms of electric, resp. magnetic field of incident EM wave in layer's volume, ε is permitivity and μ is permeability of environment.

Experimental contribution of light generation term to total conductivity of Si is significant and even prevailing. Light illumination increase electric conductivity

about 2 orders of magnitude in dependence on light intensity [Ledinsky2011], [Ledinsky2012].

Effect of light induced conductivity alternation is detectable by tunneling current amplifier of Bruker Icon dimension AFM. AFM uses red light laser diode for cantilever positioning within scanning maneuvers. Red light beam incidents on cantilever's coating and reflects to quadrant photodetector (Fig. 2.3). Cantilever is variously vertically and torsionally deflected, as it moves across the layer's terrain. Cantilever's inclination changes reflective angle of incident light beam. Different position of light spot on photodetector is subsequently processed and evaluated. Feedback loop maintains constant force that probe acts on sample's surface. Proportional and integral feedback gain parameters control error between measured value of deflection and desired deflection setpoint.

Furthermore, AFM scanning head is equipped with optical microscope. Microscope serves for sample focusing and for orientation on sample's surface. Auxiliary lamp is attached to microscope's objective. Lamp shines with white light at sample's surface.

Light intensity of microscope lamp is adjustable in range from 1 to 100% of its maximum value. Maximum lamp intensity is much more lower than constant light intensity of the laser diode [Ledinsky2011], [Ledinsky2012].

AFM operation software permits double pass scan consisting of main and interleave scan stage. Firstly, topography is detected within the main stage and the line profile is memorized. During the second interleave stage, feedback controls constant contact height and laser diode could be switched off, thus the only microscope lamp illuminates the film's surface. Tunneling current can be measured within both of stages. After the interleave stage, AFM halts until laser diode stabilizes its light power (delay 100 - 300 ms), then probe repeats main scan stage. This procedure is periodically iterated until required number of scanned rows is obtained (typically 256, 512). It must be emphasize, that interleave trajectory does not match precisely with the trajectory, taken in main stage. Inspite of that, interleave scanning stage stays convenient method for measurement of Si film's photoresponse.

Cantilever hinders light propagation bellow its body and scatters incident light rays. Nevertheless, cantilever's width $\approx 30-40\,\mu m$ and thickness $1-5\,\mu m$ are so far from the wavelength. That is why, the light can relatively easily get beyond the geometrical shadow of cantilever. However, it is doubtful and arguable to believe that illumination at cantilever's contact zone is homogeneous and well defined.

Initially, we find it beneficial to investigate local coincidence of dark and photo conductivity. Such information could be extracted from height, deflection error,

Figure 4.6: *Dark and photo current profile's coincidence with structural formation of crystalline grain and amorphous surroundings. Vertical delimiters restrict grain's interior. Height, deflection error, dark and photo current are normalized to interval from 0 to 1. Each group of paired functions is shifted in y-axis about 1 upward. Bias sample voltage was* $-3\,V$.

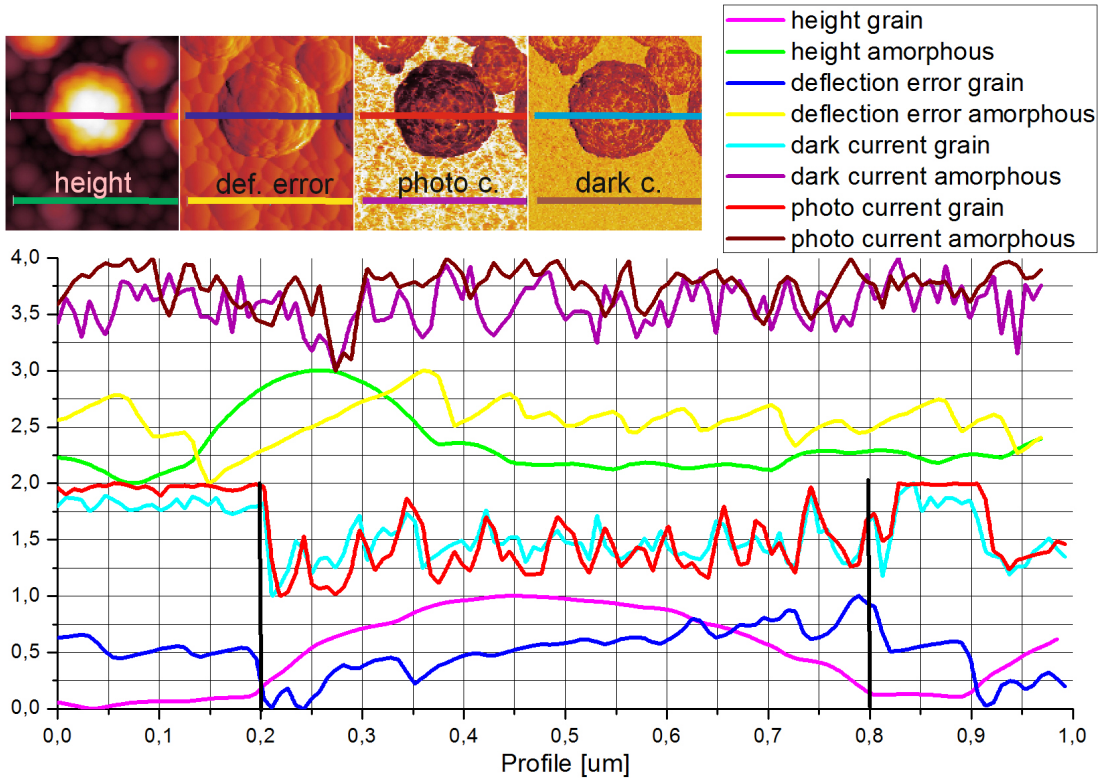

photocurrent and darkcurrent scans. Photocurrent map is received within first main scan stage. In this stage, the illumination is given by laser diode light. Microscope lamp is permanently turned off. Darkcurrent map is acquired within the interleave scan stage. Figure 4.6 shows current profiles along line crossing the grain and tissue. Besides absolute height, vertical deflection error profile is also plotted. Vertical deflection error can be compared to the derivative of height in direction of scan. Scan angle was set perpendicularly to cantilever's axis of symmetry (from left to the right side in inset of Fig. 4.6). All quantities in the graph: height, deflection error, dark and photo current are normalized to interval from 0 to 1. Each group of plotted curves is shifted in y-axis about 1 upward. Sample was biased to $-3\,V$, with deflection setpoint $0.3\,V$, integral gain 2.0 and proportional gain 5.0 .

On cap's surface, dark- and photocurrent curves overlap and roughly correspond to peaks of deflection-error curve. Small fluctuations of deflection curve are caused by submicron granular structure of grain. Leading trend of deflection-error curve is an outline of the cap's arc. Two vertical line segments restrict grain boundary. Current profiles onto amorphous surface remind "stock exchange charts" with only mild correlation between photo and dark conductivity.

4.4 Photoresponse in dependence on the grain's size

Now, we will briefly mention about dependence of photo current on light intensity for various grain size (see Fig. 4.7). An experiment outputting such result can be carried out in the following way. AFM probe scans repeatedly the same area (e.g. $2 \times 2\,\mu m^2$) with occurrence of several grains (e.g. 3-8). AFM operates at double pass scan mode. Before every scan, microscope lamp intensity is changed about 10% of its possible extent. Within interleave scan stage, laser position diode is turned off and only microscope light illuminates the area. Afterwards, photocurrent over each grain's cap is averaged and cap's diameter is measured in image processing software. Absolute value of microscope lamp intensity is not specified in instruction guide and thereby uncalibrated. We guess that lamp intensity is the most likely in orders of milliwatts. Illuminated area is a circle with diameter about $0.5\,cm$. Thus, all optical measurement are merely relative without a reference scale. If position laser diode and microscope lamp is turned off, microscope camera does not detect any picture. From this point of view, we might say that the specimen is totally in darkness.

Regrettably, result in Fig. 4.7 does not give us satisfying and fruitful information and must be interpreted carefully and flexibly. The only faithful deduction is that current is strictly monotonously increasing function of the light intensity. However, this trivial discovery was already and surely known. We can not say, whether larger grains are more photosensitive or not. For fixed light intensity, average grain current should raise as grain diameter is being increased (recall Icon AFM result in Fig. 4.5), but it is not observed. Therefore, current curves lie in a bundle with width from 2.5 to $7.5\,pA$. Approximative current for 50% of light intensity is about $10\,pA$ and for 100 % it is roughly $17\,pA$. Grain's photo current is multiplied 1.7× when light intensity is increased twice. Tissue's photo current is increased 1.1 times. Y-errorbars (root mean square) signifies high grain's cap microgranulity (see the grain with diameter $831\,nm$ in inset). Effect of current dependence upon the grain size is overridden. Bias voltage was set to $-2\,V$ within the main and the interleave stage. Tip velocity was $1.6\mu m/s$. In order to prevent tip's contact zone reduction due to abrasion of tip's conductive coating, full metallic cantilever was employed (Fig. 2.12). Cantilever consisted of an etched platinum wire slightly bent at the end. Anyway, tip blunt still exists and inevitable influences radius of the contact zone (illustratively in Fig. 2.11).

Figure 4.7: *Dependence of negative photocurrent on light intensity for various grain diameters.*

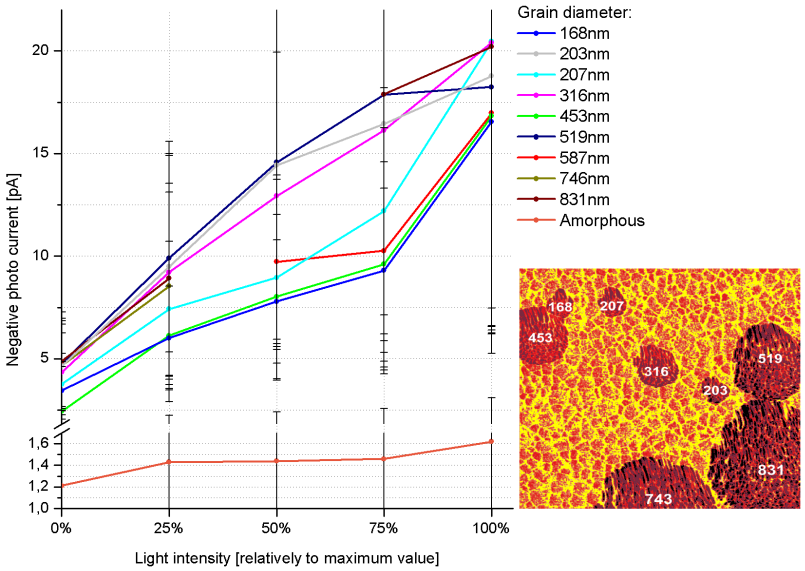

4.5 Effect of illumination of IV curve

Icon AFM allows to measure an IV curve in voltage interval from -10 to $+10\,V$, anywhere the cantilever's tip is pointed to. Cantilever's position is steady during the act of measurement. So, the position laser diode can be turned off and illumination is given only by microscope lamp. Volt-ampere characteristics of amorphous tissue in dependence upon light intensity is shown in Fig. 4.8, respectively in Fig. 4.9 for microcrystalline grain. Curve comprises of 3 parts: low voltage segment where IV curve behaves constant with null value, breakdown at bending and rapid exponential rise. Breakdown comes at $1.5\,V$ for amorphous phase and in 0.5-0.7 V for grain. IV curves, belonging to different light intensities, are split off beyond the breakdown point. Current is 2-3× increased between voltage $-2\,V$ and $-3\,V$. Null current, at zero voltage for 100% light intensity, supports the fact, that film has no dopants, as was told in section regarding the sample preparation. Repeated runs of IV curves under the same conditions do not lead to overlapping with the first one[8]. Significant current oscillations (curve fluctuation) attest instability of characteristic. Unsteady curve is probably caused by variability of interface contact between the tip and silicon-oxide thin layer. Repeated IV curves differ from the first one about 10-30% and hence creates relatively wide band[9]. This causes that two IV-curve bands, that corresponds to light intensity for instance 40 and 50%, can intersect (Fig. 4.9). Thus, IV curve measured under lower illumination can lie above IV curve measured under higher illumination. These situations was filtered out and inconvenient IV curves were

[8] In contrast to result in Figure 3 in [Ledinsky2011], where repeated IV curves are stable.
[9] As documents for example Figure 6.11 in [Vetushka-phd].

erased (Fig. 4.8), therefore graph does not includes curves for all light intensities. Accurate reproducibility of IV curves is complicated and almost impossible under standard atmospheric conditions, especially if the specimen is aged more than few hours after preparation. Voltage interval from 0 to $-3\,V$ was chosen to evade local anodic oxidation and local sample degradation (memory effect).

Figure 4.8: *IV curves of amorphous phase for voltage in interval from* 0 *to* $-3V$ *measured by Bruker Dimension Icon AFM under various microscope lamp illumination.* 100% *means maximum light intensity of microscope's lamp. Breakdown voltage is about* $1.5\,V$.

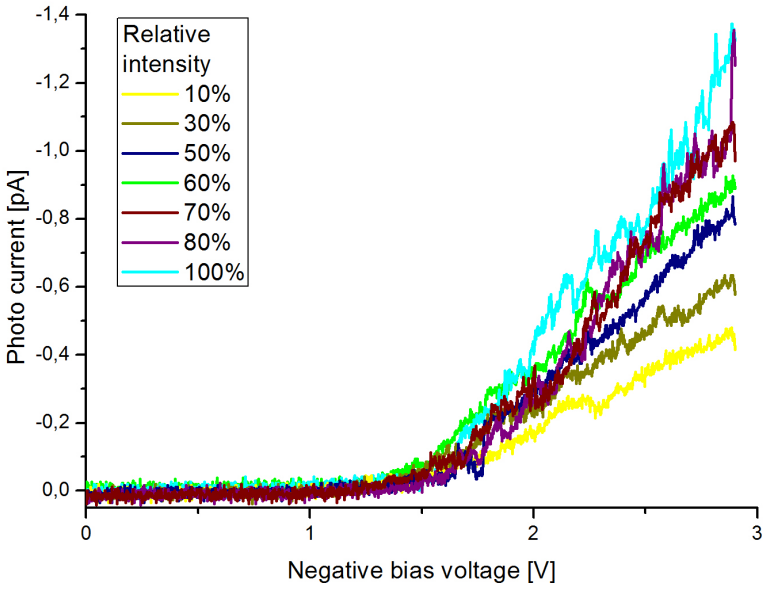

Figure 4.9: *IV curves on* μc*-Si grain for voltage in interval from* 0 *to* $-3V$ *measured by Bruker Dimension Icon AFM under various microscope lamp illumination. Breakdown voltage is approximately from 0.5 up to* $0.7\,V$.

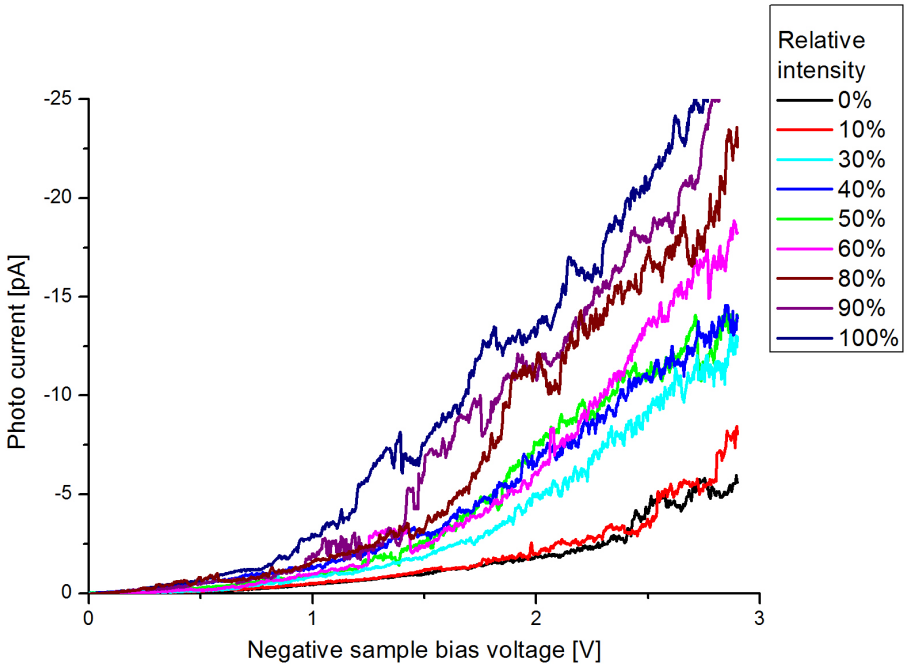

5. Discussion

The subsequent very short chapter is devoted to the confrontation of the experimental results with the finite element analysis of the grain model.

5.1 Schottky versus ohmic contact

First of all, we will take a look at the AFM tip and we will one more time reconsider, what kind of contact it actually provides. Because this is the key feature, explaining discrepancies between numerical calculations and experiment. As a matter of fact, intrinsic silicon can be regarded rather as an insulator[1] than a conductor due to conductivity around 10^{-5}-$10^{-10}\,S/cm$. Consequently, AFM current is tunneling, very diminutive and in orders of nA, pA and fA. It leads us to the thought that the contact among the tip and film suits better restrictions of the Schottky barrier contact than ohmic contact, Because the metal tip touches the semiconductive film very locally and in microscopic scale. Characteristic of Schottky contact evinces exponential current growth as applied voltage increases. Bottom electrode of specimen could be classified as an ohmic contact because of its macroscopic size. Thus, the shape of experimentally obtained IV curves (Fig. 4.8, Fig. 4.9) beyond the breakdown voltage could be interpreted as an effect of contact's nonlinear behaviour. As another proof of the hypothesis may serve the Rezek's work [Rezek2002], where he studied IV curves by AFM in ultra high vacuum and he came to the similar conclusion.

Now, we would like to paraphrase the result[2] published in [Vetushka-phd], where the author endeavoured to measure conductivity of μc-Si:H film in coplanar geometry. For such purpose, several golden $1\,mm$-thick stripes were placed equidistantly onto a glass substrate. Then, the microcrystalline thin film was deposited above. The main target was to test, whether the resistance of the film, that is enclosed by two adjacent golden electrodes, is a constant function of voltage or not. An experiment satisfactorily confirmed the assumption. Hence, both golden electrodes represent macroscopic ohmic contacts and enclosed intrinsic silicon layer is a linear material. It was discovered that coplanar conductivity is $\sigma_D = 8 \times 10^{-8}\,S/cm$ for μc-Si:H film with crystallinity around 50%.

In contrast to previous situations, cap-contact of the grain is 100% ohmic contact in our finite element model[3]. Thus, all acquired IV curves were strictly linear.

[1] Typical metal conductivity is around $10^4 - 10^5\,S/cm$, whereas conductivity of glass is $10^{-13} - 10^{-17}\,S/cm$.

[2] Fig. 6.1 and Fig. 6.2 at pages 57-58.

[3] Apparently, bottom electrode also creates ohmic contact in the FEM model.

5.2 Influence of silicon oxide layer

Next few paragraphs are addressed to the influence of thin silicon-oxide layer on experimental results. It is known fact, that whenever pure silicon is exposed to air, a very thin layer of silicon dioxide with a thickness of approximately $1\,nm$ is formed onto the surface. SiO_2 is a native oxide of silicon. The average length of Si-O bond is $0.162\,nm$ and distance between oxygen ions is $0.227\,nm$ [SiO2bond]. Thence, we are allowed to suppose that about 5 molecules of SiO_2 could be arranged in the line to fill the space $1\,nm$ thick.

In the following example, we will manifest the fact that Ohm's law[4] can not be used for physical estimation in scale of nanometers. Resistivity of silicon dioxide is about $\sigma = 10^{-14}$ – $10^{-16}\,S/cm$ at $25°C$. Suppose tip's contact area about $S = \pi\,(25\,nm)^2 \approx 2000\,nm^2$ and upper thin silicon oxide layer of thickness around $d =$ 1-2 nm. Then, in accordance to formula $R = d/(S\sigma)$, additive resistance R of the oxide must be typically 10^{18} – $10^{20}\,\Omega$. Such values are highly exaggerated and senseless. Because, hypothetically in that case, current would be dominantly determined by the oxide layer, no matter if the grain or tissue is presented. Current would have values in orders of 10^{-18} - $10^{-20}\,A$ for bias voltage $1\,V$.

This is why, electric current need to be considered as a quantum tunneling effect. For this purpose, Fowler–Nordheim formula describing tunneling current I was derived [Teichert] (p. 698), [Gehring], [Zeghbroeck]

$$I = A_{eff}\frac{e^3}{16\pi^2\hbar}\left(\frac{m_0}{m_{eff}}\right)\left(\frac{\beta}{t(E)}\right)^2\left(\frac{V}{d_{ox}}\right)^2\frac{1}{\phi}\exp\left(-\frac{4\sqrt{2m_{eff}e\phi^3}}{3\hbar}\frac{\nu(E)}{\beta}\frac{d_{ox}}{V}\right). \tag{5.1}$$

A_{eff} is an effective tunneling area (say $20 \times 20\,nm^2$), e is the elementary charge, m_0 is the free electron mass, m_{eff} is the effective mass of the electron in the oxide ($m_{eff}/m_0 = 0.4 - 0.5$), $\hbar$ is the reduced Planck constant, d_{ox} is the oxide layer thickness, V is the applied sample bias voltage, ϕ is work function of emitter ($3.25\,eV$ for Si oxide on silicon), $t(E)$ and $\nu(E)$ are tabularized functions that account for the image charge lowering[5]. These functions are able to set as constants $t(E) = 1.011 - 1.013$, $\nu(E) = 0.925 - 0.937$ for electric field in range from 10 to $25\,MV/\mu m$. β is the field enhancement factor from the nonplanar geometry of the tip (for negative bias voltage can be assumed as 1).

Relation (5.1) can be also interpreted as a product

$$I = evSN\Theta\,, \tag{5.2}$$

[4] Up to now, Ohm's law was very useful and strong tool for basic physical estimation due to its simplicity, flexibility and universality. But the limit of its validity was exceeded. For further calculations, effects of quantum mechanics must be taken into account.

[5] Image charge lowering is a decrease of induced charge on electrode.

where Θ represents probability of electron tunneling from metal through the oxide layer, v is average velocity with which electrons approach the Schottky barrier, N is density of available electrons in metal electrode, S is effective tunneling area. Probability Θ is matched with exponential function in (5.1), while product $evSN$ is assigned to the remaining prefactor in (5.1).

After numerical evaluation, we obtain

$$I = 4.63 \times 10^{-22} \left(\frac{V}{d_{ox}}\right) \exp\left(-2.53 \times 10^{10} \cdot \frac{d_{ox}}{V}\right), \tag{5.3}$$

For oxide layer thickness $d_{ox} = 0.5; 1; 1.5\,nm$ and voltage $V = 1\,V$, we acquire currents $6\,nA$; $4.8fA, 7 \times 10^{-21}\,A$.

Oxidation reaction $Si(\mathrm{s}) + O_2 \longrightarrow SiO_2$ proceeds until pure silicon is entirely covered by the insulating oxide layer[6]. Reaction rate is dependent on pressure and temperature. Dissociation energy of $Si - O$ bond is $4.68\,eV$ [SiOdisoc] and activation energy of the oxidation is roughly 1-2 eV [SiO2activ]. If AFM tip repels or attracts electrons with acceleration voltage 1-2V, electrons gain sufficient energy to initiate the oxidation reaction.

Generally, forming mechanism of the silicon dioxide growth is a complex process above the frame of the text. For more details, we refer the reader to book [Lehmann]. But it is to be noted that AFM electric measurement is time dependent as the upper surface degrades due to the oxidation. IV characteristics can not be reproduced repeatedly. Current as a function of time slowly decreases and stabilizes at various values distinct from initial one.

If AFM measurements should be avoid the effect the film's degradation, they must be carried out under UHV conditions not in ambient atmosphere. Otherwise, experimental results are heavily affected by noise and desired information is often hidden with disturbing elements and artefacts (Fig. 4.7).

5.3 Notable successes of FEM analysis

The most important achievement of FEM model is indisputably spatial distribution of electrical potential, intensity, current density and resistive losses depicted in Fig. 3.3, resp. in Fig. 3.2, because such quantities are not directly measurable via any available experimental technique.

Dependence of current on cap radius (Fig. 3.8) was confirmed experimentally (Fig. 4.5). Another verification can be found in the paper [Fejfar2010] in Figure 6, where the computed curve almost exactly coincided with the measured values

[6]Process of oxidation takes usually several hours, thereafter specimen becomes aged. To refresh film's surface quality, oxide layer must be etched off by HF acid.

by AFM.

Parametric sweep of current upon the distance of contact zone (Fig. 3.16) demonstrates another qualitative agreement with our experimental result (Fig. 4.1) or with the works [Fejfar2010], [Rezek1999], where current is a step function of radius.

Last remark to this topic is devoted to agglomerates. Figure 3.21 predicts large drop of current, when grains become separated. Analogically, figure 3.24 reveals current decrease, if size of the secondary cone is reduced bellow the critical rate. This prognosis is in concordance with the current map in the inset of Fig. 4.5.

6. Conclusion

In this study, we have attempted to get deeper insight into the issue of heterostructured thin silicon films. Thin-film photovoltaic technology leads to significant reduction of material and energy costs. Our objective was to find out and discover basic morphological and electrical properties of microcrystalline grains embedded in amorphous phase. We have also introduced to elementary measurement techniques of conductive atomic force microscopy.

In chapter 1, we tried to collect, classify and summarize some essential facts about amorphous and microcrystalline hydrogenated silicon and its preparation. After that, we focused on derivation of basic formulae of semiconductor physics. Simple electric carrier transport theory of intrinsic silicon was developed.

The process of plasma enhanced chemical vapour film deposition and specimen preparation was briefly described in chapters 1 and 2.

Qualitative structural analysis of specimen KSTM21 was carried out by scanning electron microscope. Then the topography of film's surface was inspected by AFM. Characteristic shape of microcrystalline grains – capped cone was observed.

Proportions of capped cone can be determined by two constant parameters: cone's apex semi-angle and semi-angle of spherical sector approximating the cap. Their typical values are 20°, respectively 60-90°. Typical cap radius is about 0.15 - 0.35 μm. Higher crystallinity rate causes formation of agglomerates.

In chapter 4, local electric properties of film were surveyed by Bruker Dimension Icon AFM. Dependence of current upon radial distance was discussed (Fig. 4.1) and can be delineated as a step function. The same result was obtained with finite element method (Fig. 3.16).

Further, dependence of current on cap radius was studied. Different results for NT-MDT and Dimension Icon were found out.

The last part of experimental section was aimed to film's photoresponse and comparison of dark and photo conductance.

In ambient atmosphere, reproducibility of IV curves is complicated due to surface degradation.

Chapter 3 concerns simple grain model created in Comsol Multiphysics simulation software. Comsol uses finite element analysis for its calculations. Grain model was employed for various physical arrangements.

For instance, dependence of current upon cap radius (Fig. 3.8) was figured out with the same qualitative result as the experiment showed (Fig. 4.5).

Parametric sweeps of current in dependence on incubation layer height, amorphous tissue conductivity, effective contact angle, deviation angle, contact zone distance and on contact zone radius were performed.

Section 3.7 is dedicated to agglomerates comprised of two grains. Only the one of the grains is contacted on the cap. Initially, grain's separation distance is varied as the secondary grain is moved apart from the vicinity of the primary grain (Fig. 3.21). Then, the size of the secondary grain was altered at fixed distance (Fig. 3.24), in order to clarify mutual interplay of cones.

List of abrreviations and selected symbols

symbols	
a	contact zone radius onto amorphous tissue
m^*	effective mass
N	spatial density of free carriers
T	temperature
$\mathcal{E}$	carrier's energy
$\mathcal{D}$	separation distance of cones
$\mathbf{E}$	electric field intensity
$\mathbf{D}$	electric field displacement
$\mathbf{H}$	magnetic field intensity
$\mathbf{j}$	spatial current density
$\mathbf{n}$	normal vector
w	density of electromagnetic energy
p	density of resistive power loss
P	total resistive power loss
I	current
V	electic potential
α	cone's apex semi-angle
β	semi-angle of osculating spherical sector
γ	effective contact semi-angle
δ	angular deviation of contact zone on cap
ϕ	work function
ε	permitivitty
ε_r	relative permitivitty
σ	conductivity
σ_{dark}	dark conductivity
σ_{photo}	photo conductivity
τ	mean carrier life-time
Θ	scale factor of the secondary grain
r_{cap}	cap's radius
R_{cap}	radius of spherical sector
R_{cone}	edge of cone
v_{cap}	cap's height
v_{cone}	cone's height
$v_{incubation}$	height of incubation layer
abrreviations	
AFM	Atomic Force Microscope
C-AFM	Conductive Atomic Force Microscope
EM	Electro-Magnetic
FEM	Finite Element Method
MS	Metal-Semiconductor
PV	Photo-Voltaic
PECVD	Plasma Enhanced Chemical Vapour Deposition
SEM	Scanning Electron Microscope
UHV	Ultra High Vacuum
XTEM	Cross-Sectional Transmission Electron Microscope
μc-Si:H	hydrogenated microcrystalline silicon
a-Si:H	hydrogenated amorphous silicon
p-Si	polycrystalline silicon

Table 1: **Properties of silicon** at $T = 300\,K$ [ioffeSi], [propertSi]

Proton number	14
Atomic weight	28.086
Atom density	$5 \times 10^{22}\,cm^{-3}$
Electron configuration	[Ne] $3s^2 3p^2$
Main chemical valence	4
Melting point	$1414\,°C$
Electronegativity(Pauli)	1.9
1st ionization energy	$8.15\,eV$
Electron affinity	$4.05\,eV$
Atomic radius	1.11 Å
Crystal structure	diamond
Lattice constant	5.431 Å
Main isotopic distribution	^{28}Si(92.2%), ^{29}Si(4.7%), ^{30}Si(3.1%)
Linear thermal expansion coefficient	$2.6 \times 10^{-6}\,K^{-1}$
Heat capacity c_p (at $300\,K$)	$0.7\,J/(g.K)$
Thermal conductivity	$1.3\,W/(cm.K)$
Relative magnetic permeability	1
Dielectric constant	$11.7 - 11.9$
Refractive index	3.4
Effective density of states (conduction band)	$2.8 \times 10^{19}\,cm^{-3}$
Effective density of states (valence band)	$1.8 \times 10^{19}\,cm^{-3}$
Effective electron mass	$1.08\,m_0$
Effective hole mass	$0.81\,m_0$
Mobility of electrons	$1000 - 1400\,cm^2/(V.s)$.
Mobility of holes	$200 - 450\,cm^2/(V.s)$
Diffusion coefficient of electrons	$25 - 35\,cm^2/s$
Diffusion coefficient of holes	$5 - 11\,cm^2/s$
Electron thermal velocity	$2.3 \times 10^5\,m/s$
Hole thermal velocity	$1.65 \times 10^5\,m/s$
Ionization energy for shallow donors in Si	$13.8\,meV$
Ionization energy for shallow acceptors in Si	$20.5\,meV$
Electric breakdown field	$3 \times 10^5\,V/cm$

Selected properties of a-Si and c-Si

	c-Si	a-Si
Mass density ϱ (at $300\,K$)	$2.33\,g/cm^3$	$\approx 2.25\,g/cm^3$
Young modulus	$130[100], 185[111]\,GPa$	$80 \pm 20\,GPa$
Poisson ratio	0.28[100]	0.22
Intrinsic conductivity(at $300\,K$)	$\approx 10^{-5}\,S/cm$	$\approx 10^{-8}\,S/cm$
Energy gap	$1.12\,eV$ ($300\,K$), $1.17\,eV$ ($0\,K$)	$1.7\,eV$

Bibliography

[Alsema] Alsema E. A., de Wild-Scholten M. J., Fthenakis V. M.: *Enviromental Impacts of PV electricity generation - a critical comparison of energy supply options.* 21st European Photovoltaic Solar Energy Conference, Dresden, Germany, September (2006)

[Azulay2010] Azulay D., Balberg I., Chu V., et al.: *Reply to "Comment on 'Current routes in hydrogenated microcrystalline silicon' "* . Physical Review B 81 (2010), 237302

[Bronsveld] Mates T., Bronsveld P.C.P., et al.: *Detailed structural study of low temperature mixed-phase Si films by X-TEM and ambient conductive AFM.* Journal of Non-Crystalline Solids, 352 (2006), 1011-1015.

[csgsolar] Keevers A., Young T., Schubert U., et al.: *10 % efficient CGS minimodules.*

[Fejfar2004] Fejfar A., et al.: *Model of electronic transport in microcrystalline silicon and its use for prediction of device performance.* Journal of Non-Crystalline Solids, 338-340 (2004), p. 303-309

[Fejfar2010] Fejfar A., Vetushka A., Kalusová V., et al.: *Relation of nanoscale and macroscopic properties of mixed-phase silicon thin films.* Physica Status Solidi,A 207 (2010), p. 582-586

[Fuhs] Fuhs W.: *Charge Transport in Disordered Solids with Applications in Electronics.* chapter 3: Hydrogenated Amorphous Silicon—Material Properties and Device Applications, Wiley, (2006), ISBN: 9780470095041.

[Jianming] Jianming Jin: *Introduction to the finite element method of electromagnetics.* John Willey & Sons, Inc. publisher, (2002), ISBN: 0-471-43818-9.

[Johnson] Johnson K. L.: *Contact mechanics.* Cambridge University Press, (1987), ISBN: 9780521347969.

[Kalusova] Kalusová V., *Modelování vnitřních polí v nanostrukturních křemíkových vrstvách metodou konečných prvků.* Bachelor thesis, (2010), University of West Bohemia, Faculty of Applied Science, Supervisor: Fejfar A.

[Ledinsky2011] Ledinský M., et al.: *Local photoconductivity of microcrystalline silicon thin films measured by conductive atomic force microscopy.* Physica Status Solidi RRL 5, No. 10-11 (2011), p. 373-375

[Ledinsky2012] Ledinský M., et al.: *Local photoconductivity of microcrystalline silicon thin films excited by 442 nm HeCd laser measured by conductive atomic force microscopy.* Journal of Non-Crystalline Solids, preprint (2012)

[Lehmann] Lehmann Volker: *Electrochemistry of Silicon: Instrumentation, Science, Materials and Applications.* Wiley-VCH Press, (2002), ISBN: 3-527-29321-3.

[Polycarpou] Polycarpou Anastasis C.: *Introduction to the finite element method of electromagnetics.* Morgan & Claypool, (2006), ISBN: 1598290460.

[Rezek1999] Rezek B., et al.: *Local characterization of electronic transport in microcrystalline silicon films with submicron resolution.* Applied Physical Letters, Vol.74 No. 10 (1999), p. 1475-1477

[Rezek2002] Rezek B., et al.: *Microcrystalline silicon thin films studied by atomic force microscopy with electrical current detection.* Journal of Applied Physics, Vol.92 No. 1 (2002), p. 587-593

[Shah] Shah Arwind, et al.: *Thin film silicon solar cells* . 1st edition . EPFL Press, (2010), ISBN: 978-2-940222-36-0.

[Sproul] Sproul A. B.,Green M. A.: *Improved value for the silicon intrinsic carrier concentration from 275 to 375 K.* Journal of Applied Physics, vol. 70, issue 2, pp. 846, (1991).

[Teichert] Teichert C., Beinik I.: *Conductive Atomic-Force Microscopy Investigation of Nanostructures in Microelectronics.* chapter 23 (Scanning Probe Microscopy in nanoscience and Technology 2), Springer (2011).

[Vetushka-phd] Vetushka A.: *Mechanical and Electrical Properties of μc-Si:H Thin Films Studied by Raman microspectroscopy and combined AFM.* Doctoral thesis, (2010), Charles University MFF, Supervisor: Fejfar A.

[Vetushka2010] Vetushka A., et al.: *Comment on "Current routes in hydrogenated microcrystalline silicon".* Physical Review, B 81 (2010), 237301.

[ioffeSi] Properties of c-Si: `http://www.ioffe.ru/SVA/NSM/Semicond/Si/index.html`

[propertSi] Properties of c-Si: `http://www.phy.duke.edu/~hx3/physics/silicon/silicon.htm#4`

[AbsorptionSi] Green M.A., Keevers M.: *Optical properties of intrinsic silicon at 300 K.* Progress in Photovoltaics, p.189-92, vol.3, no.3, (1995).

[conSi] Intrinsic concentration of c-Si: `http://www.pveducation.org/pvcdrom/pn-junction/intrinsic-carrier-concentration`

[EnGap] Thermal correction of energy gap: `http://ecee.colorado.edu/~bart/book/book/chapter2/ch2_3.htm` equation (2.3.5)

[AbsorpSi] Optical absorption of c-Si: `http://www.pveducation.org/pvcdrom/appendicies/optical-properties-of-silicon`

[ncSi] Refractive index c-Si: `http://www.filmetrics.com/refractive-index-database/Si/Silicon`

[naSi] Refractive index a-Si: `http://refractiveindex.info/?group=CRYSTALS&material=a-Si`

[npSi] Refractive index poly-Si: `http://refractiveindex.info/?group=CRYSTALS&material=poly-Si`

[SiO2bond] Length of SiO_2 bond: `http://www.iue.tuwien.ac.at/phd/hoessinger/node28.html`

[SiOdisoc] Dissociation energy of $Si-O$ bound: http://www.sartep.com/chem/chartsandtools/bondenergy.cfm

[SiO2activ] Activation energy of SiO_2: http://www.iue.tuwien.ac.at/phd/hollauer/node16.html

[Gehring] GEHRING Andreas: *Simulation of Tunneling in Semiconductor Devices.* Doctoral thesis, (2003), Technical University of Wien, http://www.iue.tuwien.ac.at/phd/gehring/diss.html

[Zeghbroeck] VAN ZEGHBROECK Bart: *Principles of Semiconductor Devices.* chapter: Field emission - Fowler-Nordheim tunneling, (1997), http://ecee.colorado.edu/~bart/book/home.htm

[Comsol] ComsolMultiphysics: http://www.humusoft.cz/produkty/comsol/

[Gwyd] Gwyddion software: http://www.gwyddion.net/

[WSxM] WSxM software: http://www.nanotec.es/products/wsxm/index.php

[Icon] Bruker Dimension Icon AFM: http://www.bruker-axs.com/dimension_icon_atomic_force_microscope.html

[Ntegra] NT-MDT NTegra AFM: http://www.ntmdt.com/platform/ntegra